A&A 594, A1 (2016)
DOI: 10.1051/0004-6361/201527101

Astronomy & Astrophysics
Special feature

Planck 2015 results

I. Overview of products and scientific results

Planck Collaboration: R. Adam[105], P. A. R. Ade[126], N. Aghanim[84], Y. Akrami[89,148], M. I. R. Alves[143,14,84], F. Argüeso[28], M. Arnaud[103], F. Arroja[94,109], M. Ashdown[98,9], J. Aumont[84], C. Baccigalupi[123], M. Ballardini[46,70,72], A. J. Banday[143,14], R. B. Barreiro[92], J. G. Bartlett[1,95], N. Bartolo[45,94], S. Basak[123], P. Battaglia[48,50], E. Battaner[146,147], R. Battye[96], K. Benabed[85,140], A. Benoît[82], A. Benoit-Lévy[35,85,140], J.-P. Bernard[143,14], M. Bersanelli[49,71], B. Bertincourt[84], P. Bielewicz[116,14,123], I. Bikmaev[30,4], J. J. Bock[95,16], H. Böhringer[111], A. Bonaldi[96], L. Bonavera[26], J. R. Bond[13], J. Borrill[19,131], F. R. Bouchet[85,129], F. Boulanger[84], M. Bucher[1], R. Burenin[130,113], C. Burigana[70,47,72], R. C. Butler[70], E. Calabrese[135], J.-F. Cardoso[104,1,85], P. Carvalho[88,98], B. Casaponsa[92], G. Castex[1], A. Catalano[105,101], A. Challinor[88,98,17], A. Chamballu[103,21,84], R.-R. Chary[81], H. C. Chiang[39,10], J. Chluba[34,98], G. Chon[111], P. R. Christensen[117,53], S. Church[133], M. Clemens[67], D. L. Clements[80], S. Colombi[85,140], L. P. L. Colombo[33,95], C. Combet[105], B. Comis[105], D. Contreras[32], F. Couchot[100], A. Coulais[101], B. P. Crill[95,16], M. Cruz[27], A. Curto[92,9,98], F. Cuttaia[70], L. Danese[123], R. D. Davies[96], R. J. Davis[96], P. de Bernardis[48], A. de Rosa[70], G. de Zotti[67,123], J. Delabrouille[1], J.-M. Delouis[85,140], F.-X. Désert[77], E. Di Valentino[85,129], C. Dickinson[96], J. M. Diego[92], K. Dolag[145,110], H. Dole[84,83], S. Donzelli[71], O. Doré[95,16], M. Douspis[84], A. Ducout[85,80], J. Dunkley[135], X. Dupac[57], G. Efstathiou[98,88], P. R. M. Eisenhardt[95], F. Elsner[35,85,140], T. A. Enßlin[110], H. K. Eriksen[89], E. Falgarone[101], Y. Fantaye[52,5], M. Farhang[13,122], S. Feeney[80], J. Fergusson[17], R. Fernandez-Cobos[92], F. Feroz[9], F. Finelli[70,72], E. Florido[146], O. Forni[143,14], M. Frailis[69], A. A. Fraisse[39], C. Franceschet[49], E. Franceschi[70], A. Frejsel[117], A. Frolov[128], S. Galeotta[69], S. Galli[97], K. Ganga[1], C. Gauthier[1,109], R. T. Génova-Santos[91,25], M. Gerbino[138,119,48], T. Ghosh[84], M. Giard[143,14], Y. Giraud-Héraud[1], E. Giusarma[48], E. Gjerløw[89], J. González-Nuevo[26,92], K. M. Górski[95,150], K. J. B. Grainge[9,98], S. Gratton[98,88], A. Gregorio[50,69,76], A. Gruppuso[70,72], J. E. Gudmundsson[138,119,39], J. Hamann[139,136], W. Handley[98,9], F. K. Hansen[89], D. Hanson[112,95,13], D. L. Harrison[88,98], A. Heavens[80], G. Helou[16], S. Henrot-Versillé[100], C. Hernández-Monteagudo[18,110], D. Herranz[92], S. R. Hildebrandt[95,16], E. Hivon[85,140], M. Hobson[9], W. A. Holmes[95], A. Hornstrup[22], W. Hovest[110], Z. Huang[13], K. M. Huffenberger[37], G. Hurier[84], S. Ilić[143,14,8], A. H. Jaffe[80], T. R. Jaffe[143,14], T. Jin[9], W. C. Jones[39], M. Juvela[38], A. Karakci[1], E. Keihänen[38], R. Keskitalo[19], I. Khamitov[137,30], K. Kiiveri[38,64], J. Kim[110], T. S. Kisner[107], R. Kneissl[55,11], J. Knoche[110], L. Knox[42], N. Krachmalnicoff[49], M. Kunz[23,84,5], H. Kurki-Suonio[38,64], F. Lacasa[84,65], G. Lagache[7,84], A. Lähteenmäki[2,64], J.-M. Lamarre[101], M. Langer[84], A. Lasenby[9,98], M. Lattanzi[47,73], C. R. Lawrence[95,⋆], M. Le Jeune[1], J. P. Leahy[96], E. Lellouch[102], R. Leonardi[12], J. León-Tavares[90,59,3], J. Lesgourgues[86,139], F. Levrier[101], A. Lewis[36], M. Liguori[45,94], P. B. Lilje[89], M. Lilley[85,129], M. Linden-Vørnle[22], V. Lindholm[38,64], H. Liu[117,53], M. López-Caniego[57], P. M. Lubin[43], Y.-Z. Ma[96,125], J. F. Macías-Pérez[105], G. Maggio[69], D. Maino[49,71], D. S. Y. Mak[88,98], N. Mandolesi[70,47], A. Mangilli[84,100], A. Marchini[74], A. Marcos-Caballero[92], D. Marinucci[52], M. Maris[69], D. J. Marshall[103], P. G. Martin[13], M. Martinelli[148], E. Martínez-González[92], S. Masi[48], S. Matarrese[45,94,61], P. Mazzotta[51], J. D. McEwen[114], P. McGehee[81], S. Mei[60,142,16], P. R. Meinhold[43], A. Melchiorri[48,74], J.-B. Melin[21], L. Mendes[57], A. Mennella[49,71], M. Migliaccio[88,98], K. Mikkelsen[89], M. Millea[42], S. Mitra[79,95], M.-A. Miville-Deschênes[84,13], D. Molinari[47,70,73], A. Moneti[85], L. Montier[143,14], R. Moreno[102], G. Morgante[70], D. Mortlock[80], A. Moss[127], S. Mottet[85,129], M. Münchmeyer[85], D. Munshi[126], J. A. Murphy[115], A. Narimani[32], P. Naselsky[118,54], A. Nastasi[84], F. Nati[39], P. Natoli[47,6,73], M. Negrello[67], C. B. Netterfield[29], H. U. Nørgaard-Nielsen[22], F. Noviello[96], D. Novikov[108], I. Novikov[117,108], M. Olamaie[9], N. Oppermann[13], E. Orlando[149], C. A. Oxborrow[22], F. Paci[123], L. Pagano[48,74], F. Pajot[84], R. Paladini[81], S. Pandolfi[24], D. Paoletti[70,72], B. Partridge[63], F. Pasian[69], G. Patanchon[1], T. J. Pearson[16,81], M. Peel[96], H. V. Peiris[35], V.-M. Pelkonen[81], O. Perdereau[100], L. Perotto[105], Y. C. Perrott[9], F. Perrotta[123], V. Pettorino[62], F. Piacentini[48], M. Piat[1], E. Pierpaoli[33], D. Pietrobon[95], S. Plaszczynski[100], D. Pogosyan[40], E. Pointecouteau[143,14], G. Polenta[6,68], L. Popa[87], G. W. Pratt[103], G. Prézeau[16,95], S. Prunet[85,140], J.-L. Puget[84], J. P. Rachen[31,110], B. Racine[89], W. T. Reach[144], R. Rebolo[91,20,25], M. Reinecke[110], M. Remazeilles[96,84,1], C. Renault[105], A. Renzi[52,75], I. Ristorcelli[143,14], G. Rocha[95,16], M. Roman[1], E. Romelli[50,69], C. Rosset[1], M. Rossetti[49,71], A. Rotti[79], G. Roudier[1,101,95], B. Rouillé d'Orfeuil[100], M. Rowan-Robinson[80], J. A. Rubiño-Martín[91,25], B. Ruiz-Granados[146], C. Rumsey[9], B. Rusholme[81], N. Said[48], V. Salvatelli[48,8], L. Salvati[48], M. Sandri[70], H. S. Sanghera[88,98], D. Santos[105], R. D. E. Saunders[9], A. Sauvé[143,14], M. Savelainen[38,64], G. Savini[120], B. M. Schaefer[141], M. P. Schammel[9,93], D. Scott[32], M. D. Seiffert[95,16], P. Serra[84], E. P. S. Shellard[17], T. W. Shimwell[9,134], M. Shiraishi[45,94], K. Smith[121], T. Souradeep[79], L. D. Spencer[126], M. Spinelli[100], S. A. Stanford[42], D. Stern[95], V. Stolyarov[9,132,99], R. Stompor[1], A. W. Strong[111], R. Sudiwala[126], R. Sunyaev[110,130], P. Sutter[85], D. Sutton[88,98], A.-S. Suur-Uski[38,64], J.-F. Sygnet[85], J. A. Tauber[58], D. Tavagnacco[69,50], L. Terenzi[124,70], D. Texier[56], L. Toffolatti[26,92,70], M. Tomasi[49,71], M. Tornikoski[3], D. Tramonte[91,25], M. Tristram[100], A. Troja[49], T. Trombetti[70,47], M. Tucci[23], J. Tuovinen[15], M. Türler[78], G. Umana[66], L. Valenziano[70], J. Valiviita[38,64], F. Van Tent[106], T. Vassallo[69], L. Vibert[84], M. Vidal[96], M. Viel[69,76], P. Vielva[92], F. Villa[70], L. A. Wade[95], B. Walter[63], B. D. Wandelt[85,140,44], R. Watson[96], I. K. Wehus[95,89], N. Welikala[135], J. Weller[145], M. White[41], S. D. M. White[110], A. Wilkinson[96], D. Yvon[21], A. Zacchei[69], J. P. Zibin[32], and A. Zonca[43]

(Affiliations can be found after the references)

Received 1 August 2015 / Accepted 18 January 2016

ABSTRACT

The European Space Agency's *Planck* satellite, which is dedicated to studying the early Universe and its subsequent evolution, was launched on 14 May 2009. It scanned the microwave and submillimetre sky continuously between 12 August 2009 and 23 October 2013. In February 2015, ESA and the Planck Collaboration released the second set of cosmology products based on data from the entire *Planck* mission, including both temperature and polarization, along with a set of scientific and technical papers and a web-based explanatory supplement. This paper gives an overview of the main characteristics of the data and the data products in the release, as well as the associated cosmological and astrophysical science results and papers. The data products include maps of the cosmic microwave background (CMB), the thermal Sunyaev-Zeldovich effect, diffuse foregrounds in temperature and polarization, catalogues of compact Galactic and extragalactic sources (including separate catalogues of

⋆ Corresponding author: C. R. Lawrence, e-mail: charles.lawrence@jpl.nasa.gov

Sunyaev-Zeldovich clusters and Galactic cold clumps), and extensive simulations of signals and noise used in assessing uncertainties and the performance of the analysis methods. The likelihood code used to assess cosmological models against the *Planck* data is described, along with a CMB lensing likelihood. Scientific results include cosmological parameters derived from CMB power spectra, gravitational lensing, and cluster counts, as well as constraints on inflation, non-Gaussianity, primordial magnetic fields, dark energy, and modified gravity, and new results on low-frequency Galactic foregrounds.

Key words cosmology: observations – cosmic background radiation – surveys – space vehicles: instruments – instrumentation: detectors

1. Introduction

The *Planck* satellite[1] (Tauber et al. 2010; Planck Collaboration I 2011), launched on 14 May 2009, observed the sky continuously from 12 August 2009 to 23 October 2013. *Planck*'s scientific payload contained an array of 74 detectors in nine bands covering frequencies between 25 and 1000 GHz, which scanned the sky with angular resolution between 33′ and 5′. The detectors of the Low Frequency Instrument (LFI; Bersanelli et al. 2010; Mennella et al. 2011) were pseudo-correlation radiometers, covering bands centred at 30, 44, and 70 GHz. The detectors of the High Frequency Instrument (HFI; Lamarre et al. 2010; Planck HFI Core Team 2011) were bolometers, covering bands centred at 100, 143, 217, 353, 545, and 857 GHz. *Planck* imaged the whole sky twice in one year, with a combination of sensitivity, angular resolution, and frequency coverage never before achieved. *Planck*, its payload, and its performance as predicted at the time of launch are described in 13 papers included in a special issue of Astronomy & Astrophysics (Volume 520).

The main objective of *Planck*, defined in 1995, was to measure the spatial anisotropies in the temperature of the cosmic microwave background (CMB), with an accuracy set by fundamental astrophysical limits, thereby extracting essentially all the cosmological information embedded in the temperature anisotropies of the CMB. *Planck* was not initially designed to measure to high accuracy the CMB polarization anisotropies, which encode not only a wealth of cosmological information, but also provide a unique probe of the history of the Universe during the time when the first stars and galaxies formed. However, during *Planck*'s development it was significantly enhanced in this respect, and its polarization measurement capabilities have exceeded all original expectations. *Planck* was also designed to produce a wealth of information on the properties of extragalactic sources, including clusters of galaxies via the Sunyaev-Zeldovich (SZ) effect, and the dust and gas in the Milky Way. The scientific objectives of *Planck* were described in detail in Planck Collaboration (2005). With the results presented here and in a series of accompanying papers, *Planck* has already achieved all of its planned science goals.

An overview of the scientific operations of the *Planck* mission was given in Planck Collaboration I (2014). Further operational details extending to the end of the mission are presented in the 2015 Explanatory Supplement (Planck Collaboration 2015). The first set of scientific data, the Early Release Compact Source Catalogue (ERCSC; Planck Collaboration VII 2011), was released in January 2011. At the same time, a set of 26 papers related to astrophysical foregrounds were published in a special issue of Astronomy and Astrophysics (Vol. 536, 2011). Since then, 40 "Intermediate" (i.e., between the major data releases) papers have been submitted to A&A containing further astrophysical investigations by the Collaboration. The second set of scientific data (sometimes referred to as Planck Release 1 or "PR1", because it was the first release of cosmologically useful data) consisting mainly of temperature maps of the whole sky, was released in March of 2013. These data and associated scientific results are described in a set of 32 papers in another special issue of A&A (Vol. 571, 2014). This paper presents an overview of the third set of scientific data (and second set of cosmological data, hence "PR2") and scientific results to be released by *Planck*, based on the data acquired during the complete *Planck* mission from 12 August 2009 to 23 October 2013, and hereafter referred to as the "2015 products".

2. Data products in the 2015 release

The 2015 distribution of released products, freely accessible via the *Planck* Legacy Archive interface (PLA)[2], is based on all the data acquired by *Planck* during routine operations, starting on 12 August 2009 and ending on 23 October 2014. The distribution contains the following items.

- Cleaned and calibrated data timelines for each detector.
- Maps of the sky at nine frequencies (Sect. 7) in temperature, and at seven frequencies (30–353 GHz) in polarization. Additional products serve to quantify the characteristics of the maps to a level adequate for the science results being presented, such as noise maps, masks, and instrument characteristics.
- High-resolution maps of the CMB sky in temperature from four different component-separation approaches, and accompanying characterization products (Sect. 8.1).
- High-pass-filtered maps of the CMB sky in polarization from four different component-separation approaches, and accompanying characterization products (Sect. 8.1). The rationale for providing these maps is explained in Sect. 2.2.
- A low-resolution CMB temperature map (Sect. 8.1) used in the low-ℓ likelihood code, with an associated set of foreground temperature maps produced as part of the process of separating the low-resolution CMB from foregrounds, with accompanying characterization products.
- Maps of thermal dust and residual cosmic infrared background (CIB) fluctuations, as well as carbon monoxide (CO), synchrotron, free-free, and spinning dust temperature emission, plus maps of dust temperature and opacity (Sect. 9).
- Maps of synchrotron and dust polarized emission.
- A map of the estimated CMB lensing potential over 70% of the sky.
- A map of the SZ effect Compton parameter.
- Monte Carlo chains used in determining cosmological parameters from the *Planck* data.
- The Second Planck Catalogue of Compact Sources (PCCS2; Sect. 9.1), comprising lists of compact sources over the entire sky at the nine *Planck* frequencies. The PCCS2 includes polarization information, and supersedes the previous Early Release Compact Source Catalogue (Planck Collaboration XIV 2011) and the PCCS1 (Planck Collaboration XXVIII 2014).

[1] *Planck* (http://www.esa.int/Planck) is a project of the European Space Agency (ESA) with instruments provided by two scientific consortia funded by ESA member states and led by Principal Investigators from France and Italy, telescope reflectors provided through a collaboration between ESA and a scientific consortium led and funded by Denmark, and additional contributions from NASA (USA).

[2] http://pla.esac.esa.int

- The Second Planck Catalogue of Sunyaev-Zeldovich Sources (PSZ2; Sect. 9.2), comprising a list of sources detected by their SZ distortion of the CMB spectrum. The PSZ2 supersedes the previous Early Sunyaev-Zeldovich Catalogue (Planck Collaboration XXIX 2014) and the PSZ1 (Planck Collaboration XXIX 2014).
- The Planck Catalogue of Galactic Cold Clumps (PGCC; Planck Collaboration XXVIII 2016), providing a list of Galactic cold sources over the whole sky (see Sect. 9.3). The PGCC supersedes the previous Early Cold Core Catalogue (ECC), part of the Early Release Compact Source Catalogue (ERCSC; Planck Collaboration VII 2011).
- A full set of simulations, including Monte Carlo realizations.
- A likelihood code and data package used for testing cosmological models against the *Planck* data, including both the CMB (Sect. 8.4.1) and CMB lensing (Sect. 8.4.2).

The first 2015 products were released in February 2015, polarized maps and time-ordered data were released in July 2015, and simulations were released in September 2015 (see Sect. 4). In parallel, the Planck Collaboration is developing the next generation of data products, which will be delivered in 2016.

2.1. Polarization convention

The *Planck* Stokes parameter maps and data follow the "COSMO" [3] convention for polarization angles, rather than the "IAU" (Heeschen & Howard 1974; Hamaker & Bregman 1996) convention. The net effect of using the COSMO convention is a sign inversion on Stokes U with respect to the IAU convention (position angle increases clockwise in the IAU convention, anticlockwise in the IAU convention). On the other hand, when polarization angles are discussed in Planck Collaboration papers, they are given in the IAU convention (e.g., in the Planck Catalogue of Compact Sources, Planck Collaboration XXVIII 2014; the Second Planck Catalogue of Compact Sources, Planck Collaboration XXVI 2016; and papers on foregrounds), with position angle zero being the direction of the north Galactic pole. All *Planck* FITS files containing polarization data include a keyword (POLCCONV) that specifies the convention used, and the text and figures of papers also specify the convention. Users should be aware, however, of this potential source of confusion.

2.2. The state of polarization in the Planck 2015 data

LFI – The 2015 *Planck* release includes polarization data at 30, 44, and 70 GHz. The 70 GHz polarization data are used for the 2015 *Planck* likelihood at $\ell < 30$. The 70 GHz map is cleaned with the 30 and 353 GHz channels for synchrotron and dust emission, respectively (Planck Collaboration XIII 2016).

Control of systematic effects in polarization is a challenging task, especially at large angular scales. We analyse systematic effects in the 2015 LFI polarization data (Planck Collaboration III 2016) following two complementary paths. First, we use the redundancy in the *Planck* scanning strategy to produce difference maps that, in principle, contain the same sky signal ("null tests"). Any residuals in these maps blindly probe all non-common-mode systematics present in the data. Second, we use our knowledge of the instrument to build physical models of all relevant systematic effects. We then simulate timelines and project them into sky maps following the LFI map-making process. We quantify the results in terms of power spectra, and compare them to the FFP8 LFI noise model.

[3] See http://healpix.sourceforge.net/html/intronode6.htm.

Our analysis shows no evidence of systematic errors significantly affecting the 2015 LFI polarization results. On the other hand, our model indicates that at low multipoles the dominant LFI systematics (gain errors and ADC nonlinearity) are only marginally dominated by noise and the expected signal. Therefore, further independent tests are being carried out and will be discussed in a forthcoming paper, as well as in the final 2016 *Planck* release. These include polarization cross-spectra between the LFI 70 GHz and the HFI 100 and 143 GHz maps (that are not part of this 2015 release; see below). Because systematic effects between the two *Planck* instruments are expected to be largely uncorrelated, such a cross-instrument approach may prove particularly effective.

HFI – The February 2015 data release included polarization data at 30, 44, 70, and 353 GHz. The release of the remaining three polarized HFI channels – 100, 143, and 217 GHz – was delayed because of residual systematic errors in the polarization data, particularly but not exclusively at $\ell < 10$. The sources of these systematic errors were identified, but insufficiently characterized to support reliable scientific analyses of, for example, the optical depth to ionization τ and the isotropy and statistics of the polarization fluctuations. Due to an internal mixup, however, the unfiltered polarized sky maps ended up in the PLA instead of the high-pass-filtered ones. This was discovered in July 2015, and the high-pass-filtered maps at 100, 143, and 217 GHz were added to the PLA. The unfiltered maps have been left in place to avoid confusion, but warnings about their unsuitability for science have been added. Since February our knowledge of the causes of residual systematic errors and our characterization of the polarization maps have improved. Problems that users might encounter in the released 100–353 GHz maps include the following:

- Null tests on data splits indicate inconsistency of polarization measurements on large angular scales at a level much larger than our instrument noise model (see Fig. 10 of Planck Collaboration VIII 2016). The reasons for this are numerous and will be described in detail in a future paper.
- While analogue-to-digital converter (ADC) nonlinearity is corrected much better than in previous releases, some residual effects remain, particularly in the distortion of the dipole that leaks dipole power to higher spatial frequencies.
- Mismatches in bandpasses result in leakage of dust temperature to polarization, particularly on large angular scales.
- While the measured beam models are improved, main beam mismatches cause temperature-to-polarization leakage in the maps (see Fig. 17 of Planck Collaboration VII 2016). In producing the results given in the *Planck* 2015 release, we correct for this at the spectrum level (Planck Collaboration XI 2016), but the maps themselves contain this effect.

The component-separation work described in Sect. 9, Planck Collaboration IX (2016), and Planck Collaboration X (2016) was performed on all available data, and produced unprecedented full-sky polarization maps of foreground emission (Figs. 22 and 24), as well as maps of polarized CMB emission. The polarized CMB maps, derived using four independent component-separation methods, were the basis for quantitative statements about the level of residual polarization systematics and the conclusion that reliable science results could not be obtained from them on the largest angular scales.

Recent improvements in mapmaking methodology that reduce the level of residual systematic errors in the maps, especially at low multipoles, will be described in a future paper. A

more fundamental ongoing effort aimed at correcting systematic polarization effects in the time-ordered data will produce the final legacy *Planck* data, to be released in 2016.

3. Papers accompanying the 2015 release

The characteristics, processing, and analysis of the *Planck* data, as well as a number of scientific results, are described in a series of papers released with the data. The titles of the papers begin with "*Planck* 2015 results", followed by the specific titles below.

I. Overview of products and scientific results (*this paper*)

II. Low Frequency Instrument data processing

III. LFI systematic uncertainties

IV. LFI beams and window functions

V. LFI calibration

VI. LFI mapmaking

VII. High Frequency Instrument data processing: Time-ordered information and beam processing

VIII. High Frequency Instrument data processing: Calibration and maps

IX. Diffuse component separation: CMB maps

X. Diffuse component separation: Foreground maps

XI. CMB power spectra, likelihoods, and robustness of parameters

XII. Simulations

XIII. Cosmological parameters

XIV. Dark energy and modified gravity

XV. Gravitational lensing

XVI. Isotropy and statistics of the CMB

XVII. Constraints on primordial non-Gaussianity

XVIII. Background geometry and topology of the Universe

XIX. Constraints on primordial magnetic fields

XX. Constraints on inflation

XXI. The integrated Sachs-Wolfe effect

XXII. A map of the thermal Sunyaev-Zeldovich effect

XXIII. The thermal Sunyaev-Zeldovich effect–cosmic infrared background correlation

XXIV. Cosmology from Sunyaev-Zeldovich cluster counts

XXV. Diffuse low-frequency Galactic foregrounds

XXVI. The Second Planck Catalogue of Compact Sources

XXVII. The Second Planck Catalogue of Sunyaev-Zeldovich Sources

XXVIII. The Planck Catalogue of Galactic Cold Clumps

This paper contains an overview of the main aspects of the *Planck* project that have contributed to the 2015 release, and points to the papers that contain full descriptions. It proceeds as follows. Section 4 describes the simulations that have been generated to support the analysis of *Planck* data. Section 5 describes the basic processing steps leading to the generation of the *Planck* timelines. Section 6 describes the timelines themselves. Section 7 describes the generation of the nine *Planck* frequency maps and their characteristics. Section 8 describes the *Planck* 2015 products related to the cosmic microwave background, namely the CMB maps, the lensing products, and the likelihood code. Section 9 describes the *Planck* 2015 astrophysical products, including catalogues of compact sources and maps of diffuse foreground emission. Section 10 describes the main cosmological science results based on the 2015 CMB products. Section 11 describes some of the astrophysical results based on the 2015 data. Section 12 concludes with a summary and a look towards future *Planck* products.

4. Simulations

We simulated time-ordered information (TOI) for the full focal plane (FFP) for the nominal mission. The first five FFP realizations were less comprehensive and were primarily used for validation and verification of the *Planck* analysis codes and for cross-validation of the data processing centre (DPC) and FFP simulation pipelines. The first *Planck* cosmology results (Planck Collaboration I 2014) were supported primarily by the sixth FFP simulation set, FFP6. The current results were supported by the eighth FFP simulation set, FFP8, which is described in detail in Planck Collaboration XII (2016).

Each FFP simulation comprises a single "fiducial" realization (CMB, astrophysical foregrounds, and noise), together with separate Monte Carlo (MC) realizations of the CMB and noise. The CMB component contains the effect of our motion with respect to the CMB rest frame. This induces an additive dipolar aberration, a frequency-dependent dipole modulation, and a frequency-dependent quadrupole in the CMB data. Of these effects, the additive dipole and frequency-independent component of the quadrupole are removed (see Planck Collaboration XII 2016 for details), while the residual quadrupole and modulation effects are left in the simulations and are also left in the LFI and HFI data. The residual aberration contribution to the Doppler boosting was planned to be left in the simulations; however, due to a bug in the code generating the CMB realizations, it was inadvertently omitted. New, corrected, realizations are being generated, and will be added to the public data release when they become available. This effect remains in the LFI and HFI data.

To mimic the *Planck* data as closely as possible, the simulations use the actual pointing, data flags, detector bandpasses, beams, and noise properties of the nominal mission. For the fiducial realization, maps were made of the total observation (CMB, foregrounds, and noise) at each frequency for the nominal mission period, using the *Planck* Sky Model (Delabrouille et al. 2013). In addition, maps were made of each component separately, of subsets of detectors at each frequency, and of half-ring and single Survey subsets of the data. The noise and CMB Monte Carlo realization-sets also included both all and subsets of detectors (so-called "DetSets") at each frequency, and full and half-ring data sets for each detector combination.

To check that the 2015 results are not sensitive to the exact cosmological parameters used in FFP8, we subsequently generated FFP8.1, exactly matching the PR2 (2015) cosmology.

All of the FFP8 and FFP8.1 simulations are available to be used at NERSC[4]; in addition, a limited subset of the simulations is available for download from the PLA.

5. Data processing

5.1. Timeline processing

5.1.1. LFI

The main changes in LFI data processing compared to the earlier release (Planck Collaboration II 2014) are in how we account for beam information in the pipeline, and in calibration. Processing starts at Level 1, which retrieves necessary information from data packets and auxiliary data received from the Mission Operation

[4] http://crd.lbl.gov/cmb-data

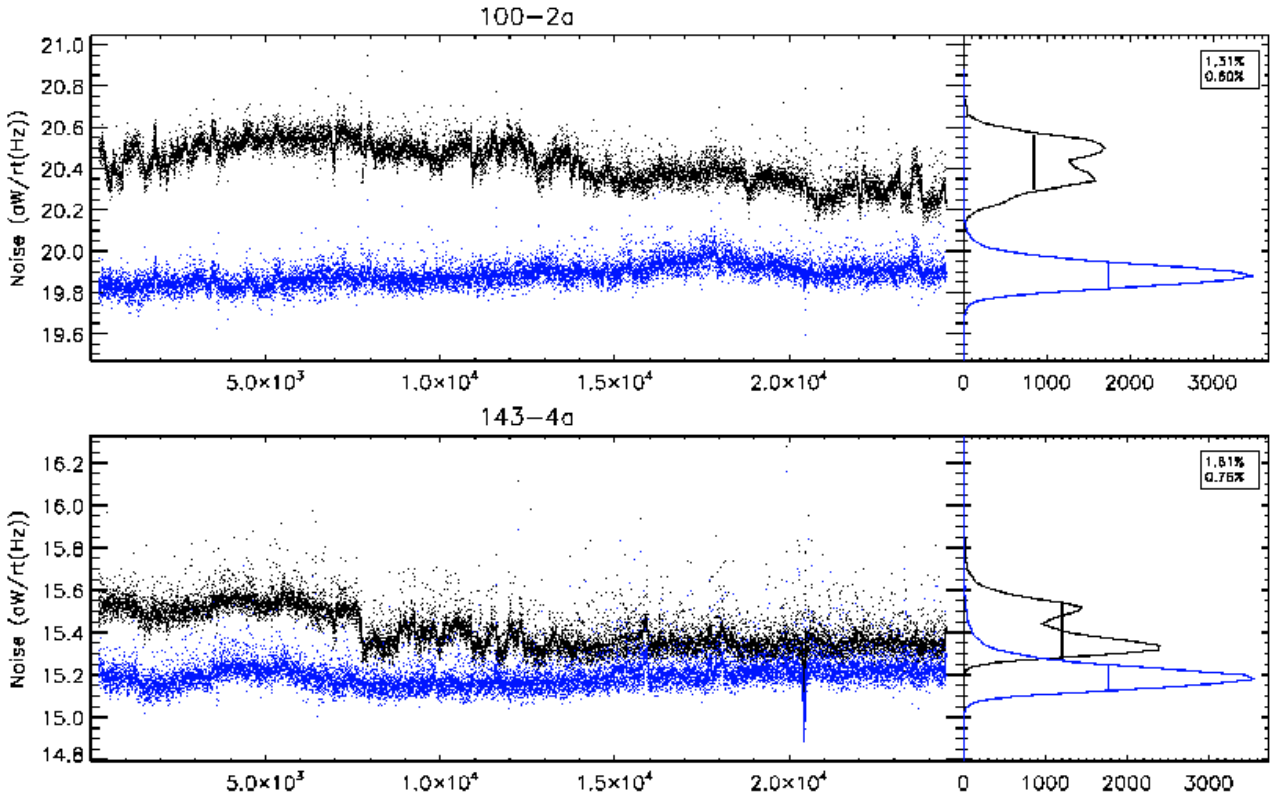

Fig. 1. *Left panels*: noise for two bolometers as a function of ring number. Black dots are from the 2013 data release; blue dots are from the 2015 release. The change in the absolute noise level is due to a change in the time-response deconvolution between the two data releases. *Right panels*: histograms of the noise. The numbers in the boxes give the width of the histogram at half maximum as a percentage of the mean noise level. For most bolometers, the FWHM in the 2015 release is less than 1% (Planck Collaboration VIII 2016).

Centre, and transforms the scientific packets and housekeeping data into a form manageable by Level 2. Level 2 uses scientific and housekeeping information to:

- build the LFI reduced instrument model (RIMO), which contains the main characteristics of the instrument;
- remove ADC nonlinearities and 1 Hz spikes diode by diode;
- compute and apply the gain modulation factor to minimize $1/f$ noise;
- combine signals from the diodes with associated weights;
- compute the appropriate detector pointing for each sample, based on auxiliary data and beam information, corrected by a model (PTCOR) built using Solar distance and radiometer electronics box assembly (REBA) temperature information;
- calibrate the scientific timelines in physical units (K_{CMB}), fitting the total CMB dipole convolved with the 4π beam representation, without taking into account the signature due to Galactic stray light;
- remove the Solar and orbital dipoles (convolved with the 4π beam) and the Galactic emission (convolved with the beam sidelobes) from the scientific calibrated timeline; and
- combine the calibrated time-ordered information (TOI) into aggregate products, such as maps at each frequency.

Level 3 collects Level 2 outputs from both LFI and HFI (Planck Collaboration VI 2016; Planck Collaboration VIII 2016) and derives various products, such as component-separated maps of astrophysical foregrounds, catalogues of different classes of source, and the likelihood of cosmological and astrophysical models given in the maps.

5.1.2. HFI

The most important change in HFI data processing compared to the 2013 release (Planck Collaboration VI 2014) is in the very first step of the pipeline, namely correction of nonlinearity in the 16-bit analogue-to-digital converters (ADCs) that are the last component in the bolometer readout electronics (Planck Collaboration 2015). The subtle effects of the ADC nonlinearities that mimic gain variations were neither detected in ground tests nor anticipated before flight, but proved to be the source of the most difficult systematic errors to deal with in the flight data. A method that reduces the effects of ADC nonlinearity by more than an order of magnitude for most channels has been implemented. Improvements can be assessed by comparing the noise stationarity in the 2013 and the 2015 data (Fig. 1). There is a significant decrease in the width of the noise distributions when the ADC correction is included.

Several other changes were also made in processing for the 2015 release. For strong signals, the threshold for cosmic ray removal ("deglitching") is auto-adjusted to cope with signal variations near bright sources caused by small pointing drifts during a ring. Thus, more glitches are left in the data in the vicinity of bright sources such as the Galactic centre than are left elsewhere. To mitigate this effect, the TOI at the planet locations are flagged and interpolated prior to further processing. For the 2015 release, this is done for Jupiter at all HFI frequency bands, for Saturn at $\nu \geq 217$ GHz, and for Mars at $\nu \geq 353$ GHz. For beam determination and calibration (see Sect. 5.2.2 of Planck Collaboration VII 2016 and Planck Collaboration VIII 2016), however, the full TOI at all planet crossings are needed at all frequencies. To recover these

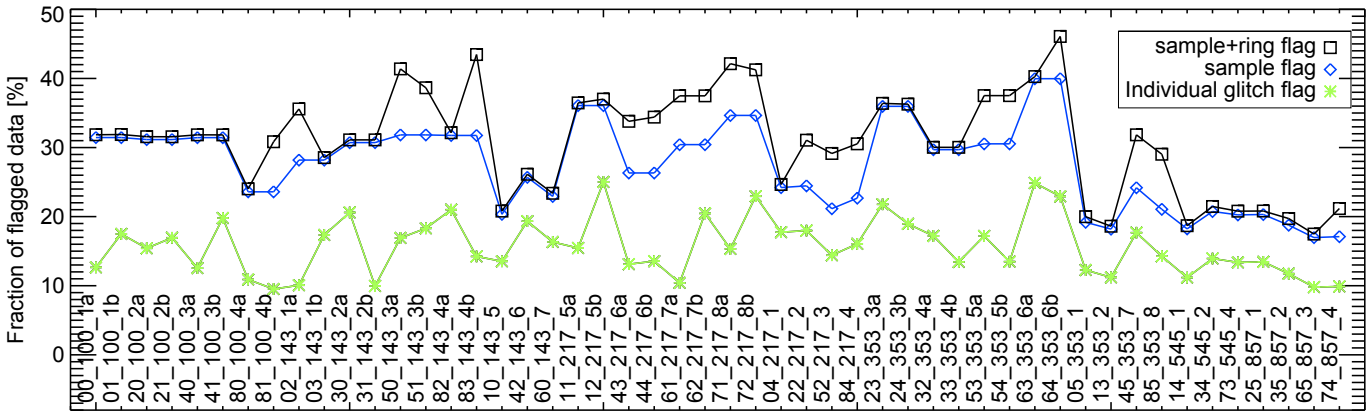

Fig. 2. Fraction of discarded data per bolometer due to all causes (black squares), sample flagging alone (blue diamonds) and glitches alone (green diamonds). Bolometers (143_8 and 545_3) are not shown, since they are not used in the data processing (see Planck Collaboration VI 2014).

data in 2015, a specialized, iterative, 3-level deglitcher is run in parallel on TOI in the vicinity of strong sources.

As noted in Planck Collaboration I (2014), *Planck* scans a given ring on the sky for between 39 and 65 min before moving on to the next ring. The data between these rings, taken while the spacecraft spin-axis is moving, are discarded as "unstable". The data taken during the intervening "stable" periods are subjected to a number of statistical tests to decide whether they should be flagged as usable or not (Planck Collaboration VI 2014). This procedure continues to be used for the present data release. An additional selection process has been introduced to mitigate the effect of interference from the 4-K cooler electronics on the data, especially the 30-Hz line signal that is correlated across bolometers. The 4-K line-removal procedure leaves correlated residuals in the 30-Hz line. The consequence of these correlations is that the angular cross-power spectra between different detectors can show excess power at multipoles around $\ell \approx 1800$ (see Sect. 10.1). To mitigate this effect, we discard all 30-Hz resonant rings for the 16 bolometers between 100 and 353 GHz for which the median average of the 30-Hz line amplitude is above 10 aW. As a result, the $\ell \approx 1800$ feature is greatly suppressed.

No other changes were made in the TOI processing software, apart from fine-tuning of several input parameters for better control of residual systematic errors noticed in the 2013 data.

Figure 2 shows the fraction of data discarded per bolometer over the full mission. Black squares show the fraction discarded due to all causes, including glitches, spin-axis repointings (8%), station-keeping manoeuvres, 4-K cooler lines, Solar flares, and end-of-life calibration sequences. Green stars show the fraction discarded due to glitches alone. Blue diamonds show the fraction discarded in rings that have some valid data, i.e., rings not flagged as entirely bad with the "ring flag". (Note that spin-axis repointing and station-keeping manoeuvres are not part of rings, and therefore never flagged as rings.) Green stars show the fraction discarded due to glitches alone. Compared to flagging in the nominal mission, presented in the 2013 papers, the main differences appear in Survey 5, which is affected by Solar flares arising from increased Solar activity, and to special calibration sequences. The full cold *Planck* HFI mission lasted 885 days, excluding the calibration and performance verification (CPV) period of 1.5 months. Globally, for this duration, the total amount of HFI data discarded amounted to 31%, about half of which came from glitch flagging.

5.2. Beams

5.2.1. LFI beams

As described in Planck Collaboration IV (2016), the in-flight assessment of the LFI main beams relied on measurements of seven Jupiter crossings: the first four occurred in nominal scan mode (spin shift 2′, 1° day^{-1}); and the last three scans in "deep" mode (spin shift 0.′5, 15′ day^{-1}). By stacking data from the seven scans, the main beam profiles are measured down to −25 dB at 30 and 44 GHz, and down to −30 dB at 70 GHz. Fitting the main beam shapes with an elliptical Gaussian profile, we have expressed the uncertainties of the measured scanning beams in terms of statistical errors for the Gaussian parameters: ellipticity; orientation; and FWHM. In this release, the error on the reconstructed beam parameters is lower than that in the 2013 release. Consequently, the error envelope on the window functions is lower as well. For example, the beam FWHM is determined with a typical uncertainty of 0.2% at 30 and 44 GHz, and 0.1% at 70 GHz, i.e., a factor of two better than the value achieved in 2013.

The scanning beams[5] used in the LFI pipeline (affecting calibration, effective beams, and beam window functions) are based on GRASP simulations, properly smeared to take into account the satellite motion, and are similar to those presented in Planck Collaboration IV (2014). They come from a tuned optical model, and represent a realistic fit to the available measurements of the LFI main beams. In Planck Collaboration IV (2014), calibration was performed assuming a pencil beam, the main beams were full-power main beams, and the resulting beam window functions were normalized to unity. For the 2015 release, a different beam normalization has been used to properly take into account the fact that not all power enters through the main beam (typically about 99% of the total power is in the main beam). As described in Planck Collaboration V (2016), the current LFI calibration takes into account the full 4π beam (i.e., the main beam, as well as near and far sidelobes). Consequently, in the

[5] The term "scanning beam" refers to the angular response of a single detector to a compact source, including the optical beam, the smearing effect of scanning plus sampling, and (for HFI) residuals of the complicated time response of the detectors and electronics. In the case of HFI, a Fourier filter deconvolves the bolometer/electronics time response and lowpass-filters the data. The term "effective beam" refers to a beam defined in the map domain, obtained by averaging the scanning beams pointing at a given pixel of the sky map, taking into account the scanning strategy and the orientation of the beams themselves when they point along the direction to that pixel (Planck Collaboration IV 2014).

calculation of the window function, the beams are not normalized to unity; instead, their normalization uses the value of the efficiency calculated taking into account the variation across the band of the optical response (coupling between feedhorn pattern and telescope) and the radiometric response (band shape).

Although the GRASP beams are computed as the far-field angular transmission function of a linearly polarized radiating element in the focal plane, the far-field pattern is in general not perfectly linearly polarized, because there is a spurious component induced by the optical system, called "beam cross-polarization". The Jupiter scans allowed us to measure only the total field, that is, the co- and cross-polar components combined in quadrature. The adopted beam model has the added value of defining the co- and cross-polar pattern separately, and it permits us to properly consider the beam cross-polarization in every step of the LFI pipeline. The GRASP model, together with the pointing information derived from the reconstruction of the focal plane geometry, gives the most advanced and precise noise-free representation of the LFI beams.

The polarized main beam models were used to calculate the effective beams, which take into account the specific scanning strategy and include any smearing and orientation effects on the beams themselves. Moreover, the sidelobes were used in the calibration pipeline to correctly evaluate the gains and to subtract Galactic stray light from the calibrated timelines (Planck Collaboration II 2016).

To evaluate the beam window functions, we adopted two independent approaches, both based on Monte Carlo simulations. In one case, we convolved a fiducial CMB signal with realistic scanning beams in harmonic space to generate the corresponding timelines and maps. In the other case, we convolved the fiducial CMB map with effective beams in pixel space using the FEBeCoP (Mitra et al. 2011) method. Using the first approach, we have also evaluated the contribution of the near and far sidelobes on the window functions. The impact of sidelobes on low multipoles is about 0.1% (for details see Planck Collaboration IV 2016).

The error budget was evaluated as in the 2013 release, and comes from two contributions: the propagation of the main beam uncertainties throughout the analysis; and the contribution of near and far sidelobes in the Monte Carlo simulation chain. Which of the two sources of error dominates depends on the angular scale. Ignoring the near and far sidelobes is the dominant error at low multipoles, while the main beam uncertainties dominate the total error budget at $\ell \geq 600$. The total uncertainties in the effective beam window functions are 0.4% at 30 GHz, 1% at 44 GHz (both at $\ell \approx 600$), and 0.3% at 70 GHz (at $\ell \approx 1000$).

5.2.2. HFI beams

Measurement of the HFI main beams is described in detail in Planck Collaboration VII (2016), and is similar to that of Planck Collaboration VII (2014) but with several important changes. The HFI scanning beam model is a "Bspline" decomposition of the time-ordered data from planetary observations. The domain of reconstruction of the main beam in 2015 is enlarged from a 40′ square to a 100′ square, and is no longer apodized, in order to preserve near sidelobe structure Planck Collaboration XXXI (2014) and to incorporate residual time-response effects into the beam model. A combination of Saturn and Jupiter data is used instead of Mars data for improved signal-to-noise ratio, and a simple model of diffraction consistent with physical optics predictions is used to extend the beam model below the noise floor of the planetary data. Additionally, a second stage of cosmic ray glitch removal is added to reduce bias from unflagged cosmic ray hits.

The effective beams and effective beam window functions are computed using the FEBeCoP and Quickbeam codes, as in Planck Collaboration VII (2014). While the scanning beam measurement produces a total intensity map only, effective beam window functions appropriate for both temperature and polarized angular power spectra are produced by averaging the individual detector window functions, weighted by temperature and polarization sensitivity. Temperature-to-polarization leakage due to main beam mismatch is subdominant to noise in the polarization measurement, and is corrected as an additional nuisance parameter in the likelihood.

Uncertainties in the beam measurements are derived from an ensemble of 100 Monte Carlo simulations of planet observations, which include random realizations of detector noise, cosmic ray hits, and pointing uncertainties propagated through the same pipeline as the data. The errors are expressed in multipole space as a set of error eigenmodes, which capture the correlation structure of the errors. Additional checks are performed to validate the error model, such as splitting up the planet data to construct Year 1 and Year 2 beams and comparison with Mars-based beams. With improved control of systematics and higher signal-to-noise ratio, the uncertainties in the HFI beam window functions have decreased by more than a factor of 10 relative to the 2013 release.

Several differences between the beams in 2013 and 2015 may be highlighted.

- *Finer polar grid.* Instead of the Cartesian grid 40′ on each side used previously, the beam maps were produced on both a Cartesian grid of 200′ on each side and 2″ resolution, and a polar grid with a radius of 100′ and a resolution of 2″ in radius and 30′ in azimuth. The latter grid has the advantage of not requiring any extra interpolation to compute the beam spherical harmonic coefficients $b_{\ell m}$ required by quickbeam, and therefore improves the accuracy of the resulting $B(\ell)$.
- *Scanning beam elongation.* To account for the elongation of the scanning beam induced by the residuals of the time-response deconvolution, quickbeam uses the $b_{\ell m}$ over the range $-6 \leq m \leq 6$. We checked that the missing terms account for less than 10^{-4} of the effective $B^2(\ell)$ at $\ell = 2000$. Moreover, comparisons with the effective $B(\ell)$ obtained by FEBeCoP show very good agreement.
- *Finite size of Saturn.* Even though its rings seem invisible at *Planck* frequencies, Saturn has an angular size that must be accounted for in the beam window function. The planet was assumed to be a top-hat disc of radius 9.″5 at all HFI frequencies, whose window function is well approximated by that of a 2D Gaussian profile of FWHM 11.″185. The effective $B(\ell)$s were therefore divided by that window function.
- *Cut sky and pixel shape variability.* The effective beam window functions do not include the (nominal) pixel window function, which must be accounted for separately in the analysis of *Planck* maps. However, the shapes and individual window functions of the HEALPix (Górski et al. 2005) pixels have large-scale variations around their nominal values across the sky. These variations affect the effective beam window functions applicable to *Planck* maps, in which the Galactic plane has been masked more or less conservatively, and are included in the effective $B(\ell)$s that are provided.
- *Polarization and detector weights.* Each 143, 217, and 353 GHz frequency map is a combination of measurements

by polarization-sensitive and polarization-insensitive detectors, each having a different optical response. As a consequence, at each of these frequencies, the Q and U maps will have a different beam window function than the I map. When cross-correlating the 143 and 217 GHz maps, for example, the TT, EE, TE, and ET spectra will each have a different beam window function.

- *Polarization and beam mismatch.* Since polarization measurements are differential by nature, any mismatch in the effective beams of the detectors involved will couple with temperature anisotropies to create spurious polarization signals (e.g., Hu et al. 2003; Leahy et al. 2010). In the likelihood pipeline (Planck Collaboration XI 2016), this additive leakage is modelled as a polynomial whose parameters are fitted to the power spectra.
- *Beam error model.* The improved S/N compared to 2013 leads to smaller uncertainties. At $\ell = 1000$ the uncertainties on B_ℓ^2 are 2.2×10^{-4}, 0.84×10^{-4}, and 0.81×10^{-4} for 100, 143, and 217 GHz, respectively. At $\ell = 2000$, they are 11×10^{-4}, 1.9×10^{-4}, and 1.3×10^{-4}.

A reduced instrument model (RIMO) containing the effective $B(\ell)$ for temperature and polarization detector assemblies is provided in the PLA for both auto- and cross-spectra. The RIMO also contains the beam error eigenmodes and their covariance matrices.

5.3. Focal plane geometry and pointing

The focal plane geometry of LFI was determined independently for each Jupiter crossing (Planck Collaboration IV 2016), using the same procedure adopted in the 2013 release. The solutions for the seven crossings agree within 4′ at 70 GHz (and 7′ at 30 and 44 GHz). The uncertainty in the determination of the main beam pointing directions evaluated from the single scans is about 4′ for the nominal scans, and 2.′5 for the deep scans at 70 GHz (27′ for the nominal scan and 19′ for the deep scan, at 30 and 44 GHz). Stacking the seven Jupiter transits, the uncertainty in the reconstructed main beam pointing directions becomes 0.′6 at 70 GHz, and 2′ at 30 and 44 GHz. With respect to the 2013 release, we have found a difference in the main beam pointing directions of about 5′ in the cross-scan direction and 0.′6 in the in-scan direction.

Throughout the extended mission, *Planck* continued to operate star camera STR1, with the redundant unit, STR2, used only briefly for testing. No changes were made to the basic attitude reconstruction. We explored the possibility of updating the satellite dynamical model and using the fibre-optic gyro for additional high frequency attitude information. Neither provided significant improvements to the pointing and were actually detrimental to overall pointing performance; however, they may become useful in future attempts to recover accurate pointing during the "unstable" periods.

Attitude reconstruction delivers two quantities, the satellite body reference system attitude, and the angles between it and the principal axis reference system (so-called "tilt" or "wobble" angles). The tilt angles are needed to reconstruct the focal plane line-of-sight from the raw body reference frame attitude. At the start of the LFI-only extension about 1000 days after launch, for unknown reasons the reconstructed tilt angles (cf. Fig. 3) began a drift that covered 1.′5 over about a month of operations. The drift was not seen in observed planet positions, and we were therefore forced to abandon the reconstructed tilt angles and include the tilt correction into our ad hoc pointing correction, PTCOR.

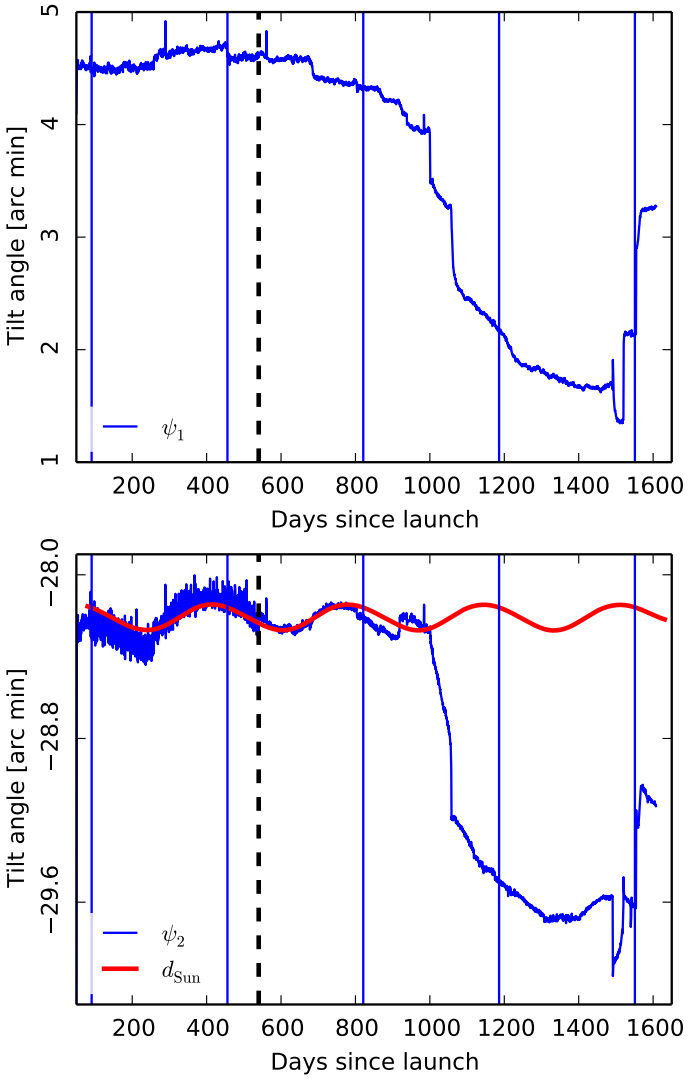

Fig. 3. Reconstructed tilt (wobble) angles between the satellite body frame and the principal axis frame. Vertical blue lines mark the boundaries of operational years, and the dashed black line indicates day 540 after launch, when the thermal control on the LFI radiometer electronics box assembly (REBA) was adjusted. *Top*: first tilt angle, ψ_1, which corresponds to a rotation about the satellite axis just 5° off the focal plane centre. Observed changes in ψ_1 have only a small effect on the focal plane line-of-sight. *Bottom*: second tilt angle, ψ_2, which is perpendicular to a plane defined by the nominal spin axis and the telescope line of sight. Rotation in ψ_2 immediately impacts the opening angle and thus the cross-scan position of the focal plane. We also plot a scaled and translated version of the Solar distance that correlates well with ψ_2 until the reconstructed angles became compromised about 1000 days after launch.

We noticed that the most significant tilt angle corrections prior to the LFI extension tracked well the distance $d_{\rm Sun}$ between the Sun and *Planck* (see Fig. 3, bottom panel), so we decided to replace the spline fitting from 2013 with the use of the Solar distance as a fitting template. The fit was improved by adding a linear drift component and inserting breaks at events known to disturb the spacecraft thermal environment. In Fig. 4 we show the co- and cross-scan pointing corrections, and a selection of planet position offsets after the correction was applied. The template-based pointing correction differs only marginally from the 2013 PTCOR, but an update was certainly necessary to provide consistent, high-fidelity pointing for the entire *Planck* mission.

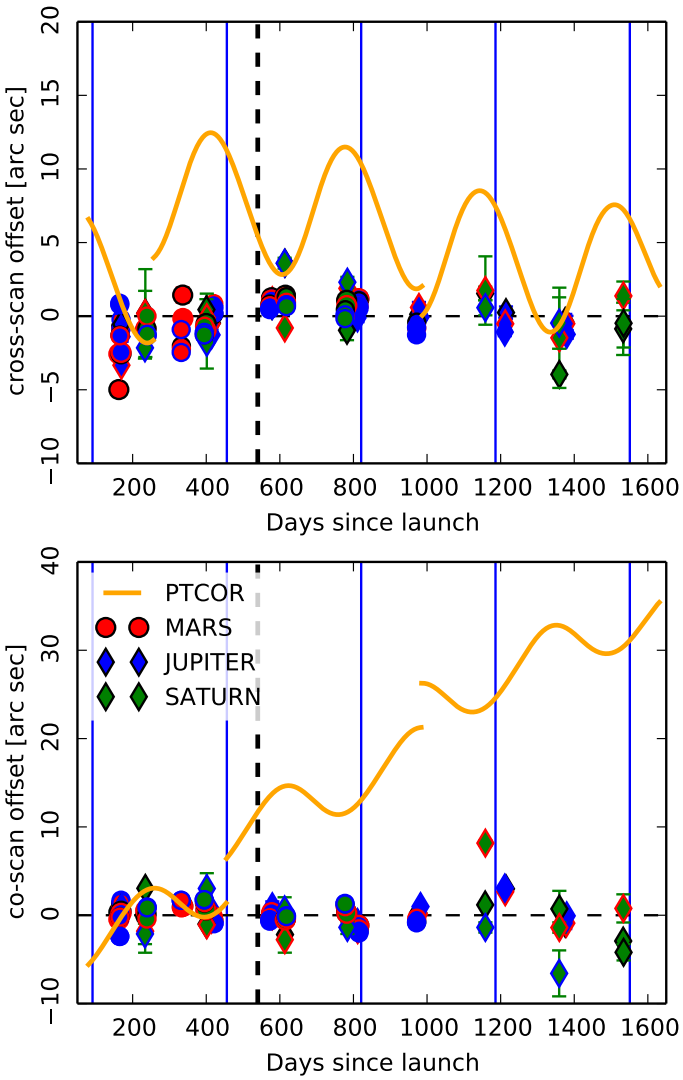

Fig. 4. PTCOR pointing correction, and a selection of observed planet position offsets after applying the correction. *Top*: cross-scan pointing offset. This angle is directly affected by the second tilt angle, ψ_2, discussed in Fig. 3. *Bottom*: in-scan pointing offset. This angle corresponds to the spin phase and matches the third satellite tilt angle, ψ_3. Since ψ_3 is poorly resolved by standard attitude reconstruction, the in-scan pointing was already driven by PTCOR in the 2013 release.

Finally, we addressed the LFI radiometer electronics box assembly (REBA) interference that was observed in the 2013 release, by constructing, fitting, and subtracting another template based on the REBA thermometry. This greatly reduced short-timescale pointing errors encountered prior to REBA thermal tuning on day 540. The REBA template-removal procedure reduced the pointing period timescale errors from 2.″7 to 0.″8 (in-scan) and 1.″9 (cross-scan).

5.4. Calibration

In this section we compare the relative photometric calibration of the all-sky CMB maps between LFI and HFI, as well as between *Planck* and WMAP. The two *Planck* instruments use different technologies and are subject to different foregrounds and systematic effects. The *Planck* and WMAP measurements overlap in frequency range, but have independent spacecraft, telescopes, and scanning strategies. Consistency tests between these three data sets are very demanding tests of the control of calibration, transfer functions, systematic effects, and foreground contamination.

5.4.1. The orbital dipole

In the 2013 data release, photometric calibration from 30 to 353 GHz was based on the "Solar dipole", that is, the dipole induced in the CMB by the motion of the Solar System barycentre with respect to the CMB. We used the value of the dipole measured by WMAP5 (Hinshaw et al. 2009; Jarosik et al. 2011).

In the 2015 data release, photometric calibration of both LFI and HFI is based on the "orbital dipole", i.e., the modulation of the Solar dipole induced by the orbital motion of the satellite around the Solar System barycentre. By using this primary calibrator, we can derive for each *Planck* detector (or combination of detectors) an independent measurement of the Solar dipole, which is then used in the *Planck* calibration pipeline. The orbital motion is known with exquisite accuracy, making the orbital dipole potentially the most accurate absolute calibration source in all of astrophysics, limited ultimately by the accuracy of the temperature of the CMB. The amplitude of this modulation, however, is only about 250 μK (varying with the details of the satellite motion), an order of magnitude smaller than the Solar dipole. Realizing its advantages as a fundamental calibration source requires low noise and good control of foregrounds, sidelobes, and large-angular-scale systematics. For the 2015 release, improvements in the control of systematic effects and foregrounds for both LFI and HFI, including the availability of 2.5 and 4 orbital cycles for HFI and LFI, respectively (compared to 1.25 cycles in the 2013 release), have allowed accurate calibration of both instruments on the orbital dipole, summarized in the following subsections and described in detail in Planck Collaboration II (2016) and Planck Collaboration VIII (2016). The dipole component of the CMB and the frequency-independent part of the quadrupole (induced by the Solar dipole) are removed from both the LFI and HFI data; however, higher-order effects of the Solar dipole (see Planck Collaboration XXVII 2014) are left in the data, as is also the case for the simulations described in Planck Collaboration XII (2016).

With the 2015 data calibrated on the orbital dipole, *Planck* has made independent measurements of the Solar dipole (Table 1), which can be compared to the WMAP5 measurement (Hinshaw et al. 2009). Amplitudes agree within 0.28%; directions agree to better than 2′. Although the difference in amplitude between the *Planck* and the WMAP5 measurements of the Solar dipole is small and within uncertainties, it had non-negligible consequences in 2013. WMAP was calibrated on the orbital dipole, so errors in its Solar dipole measurement did not contribute to its overall calibration errors. *Planck* in 2013, however, was calibrated on the WMAP5 Solar dipole, which is 0.28% lower than the orbital-dipole-calibrated 2015 *Planck* measurement. Calibrating LFI and HFI against WMAP5 in the 2013 results, therefore, resulted in 2013 gains that were 0.28% *too low* for both LFI and HFI. This factor is included in Tables 2 and 3.

5.4.2. Instrument level calibration

LFI – There were four significant changes related to LFI calibration between the 2013 and the 2015 results. First (as anticipated in the 2013 LFI calibration paper, Planck Collaboration V 2014), the convolution of the beam with the overall dipole (Solar

Table 1. LFI, HFI, and WMAP measurements of the Solar dipole.

Experiment	Amplitude [μK_{CMB}]	Galactic coordinates l [deg]	Galactic coordinates b [deg]
LFI[a]	3365.5 ± 3.0	264.01 ± 0.05	48.26 ± 0.02
HFI[a]	3364.29 ± 1.1	263.914 ± 0.013	48.265 ± 0.002
Planck 2015 nominal[a]	**3364.5 ± 2.0[b]**	**264.00 ± 0.03**	**48.24 ± 0.02**
WMAP[c]	3355[d] ± 8	263.99 ± 0.14	48.26 ± 0.03

Notes. [(a)] The "nominal" *Planck* dipole was chosen as a plausible combination of the LFI and HFI measurements early in the analysis, to carry out subtraction of the dipole from the frequency maps (see Sect. 5.4.3). The current best determination of the dipole comes from an average of 100 and 143 GHz results (Planck Collaboration VIII 2016). [(b)] Uncertainties include an estimate of systematic errors. [(c)] Hinshaw et al. (2009). [(d)] See Sect. 5.4.1 for the effect of this amplitude on *Planck* calibration in 2013.

Table 2. LFI calibration changes at map level, 2013 → 2015.

Frequency [GHz]	Beam solid angle [%]	Pipeline improvements[a] [%]	Orbital dipole[b] [%]	Total [%]
30	+0.32	−0.15	+0.28	+0.45
44	+0.03	+0.33	+0.28	+0.64
70	+0.30	+0.24	+0.28	+0.82

Notes. [(a)] This term includes the combined effect of the new destriping code, subtraction of Galactic contamination from timelines, and a new gain smoothing algorithm. It has been calculated under the simplifying assumption that it is fully independent of the beam convolution. [(b)] Change from not being dependent on the amplitude error of the WMAP9 Solar dipole (Sect. 5.4.1).

and orbital dipoles, including their induced frequency independent quadrupoles) is performed with the full 4π beam rather than a pencil beam. This dipole model is used to extract the gain calibration parameter. Because the details of the beam pattern are unique for each detector even within the same frequency channel, the reference signal used for the calibration is different for each of the 22 LFI radiometers. This change improves the results of null tests and the quality of the polarization maps. When taking into account the proper window functions (Planck Collaboration IV 2016), the new convolution scheme leads to shifts of +0.32, +0.03, and +0.30% in gain calibration at 30, 44, and 70 GHz, respectively (see Table 2). Second, a new destriping code, `Da Capo` (Planck Collaboration V 2016), is used; this supersedes the combination of a dipole-fitting routine and the `Mademoiselle` code used in the 2013 data release and offers improved handing of $1/f$ noise and residual Galactic signals. Third, Galactic contamination entering via sidelobes is subtracted from the timelines after calibration. Finally, a new smoothing algorithm is applied to the calibration parameters. It adapts the length of the smoothing window depending on a number of parameters, including the peak-to-peak amplitude of the dipole seen within each ring and sudden temperature changes in the instrument. These changes improve the results of null tests, and also lead to overall shifts in gain calibration a few tenths of a percent, depending on frequency channel. The values reported in the third column of Table 2 are approximate estimates from the combination of improved destriping, Galactic contamination removal, and smoothing. They are calculated under the simplifying assumption that these effects are completely independent of the beam convolution and can therefore be combined linearly with the latter (for more details see Planck Collaboration V 2016).

In total, these four improvements give an overall increase in gain calibration for LFI of +0.17, +0.36, and +0.54% at 30, 44, and 70 GHz, respectively. Adding the 0.28% error introduced by the WMAP Solar dipole in 2013 (discussed in Sect. 5.4.1), for the three LFI frequency channels we find overall shifts of about 0.5, 0.6 and 0.8% in gain calibration with respect to our LFI 2013 analysis (see Table 2).

As shown in Planck Collaboration V (2016), relative calibration between LFI radiometer pairs is consistent within their statistical uncertainties. At 70 GHz, using the deviations of the calibration of single channels, we estimate that the relative calibration error is about 0.1%.

HFI – There were three significant changes related to HFI calibration between the 2013 and the 2015 results: improved determination and handling of near and far sidelobes; improved ADC nonlinearity correction; and improved handling of very long time constants. The most significant changes arise from the introduction of near sidelobes of the main beam in the range of angles 0.°5 to 5°, and from the introduction of very long time constants. We consider these in turn.

Observations of Jupiter were not used in the 2013 results, because its signal is so strong that it saturates some stages of the readout electronics. The overall transfer function for each detector is corrected through the deconvolution of a time transfer function, leaving a compact effective beam that is used together with the maps in the science analysis. In the subsequent "consistency paper" (Planck Collaboration XXXI 2014), it was found that lower-noise hybrid beams built using observations of Mars, Saturn, and Jupiter reveal near sidelobes leading to significant corrections of 0.1 to 0.3%. Far sidelobes give a very small calibration correction that is almost constant for $\ell > 3$. The zodiacal contribution was removed in the timelines, since it does not project properly on the sky; it gives an even smaller and negligible correction except in the submillimetre channels at 545 and 857 GHz.

The most significant change results from the recognition of the existence of very long time constants (VLTC) and their inclusion in the analysis. VLTCs introduce a significant shift in the apparent position of the dominant anisotropy in the CMB, the Solar dipole, away from its true position. This in effect creates a leakage of the Solar dipole into the orbital dipole. This is the reason why calibration on the orbital dipole did not work as expected from simulations, and why calibration in 2013 was instead based on the WMAP5 Solar dipole. As discussed in

Table 3. HFI calibration changes at map level, 2013 → 2015.

	Sidelobes		Orbital dipole		
Frequency	Near	Far	Dipole[a]	VLTC	Total
[GHz]	[%]	[%]	[%]	[%]	[%]
100	0.2	0.087	0.28	0.49	1.06
143	0.2	0.046	0.28	0.47	1.00
217	0.2	0.043	0.28	0.66	1.17
353	0.275	0.006	0.28	1.5	2.06

Notes. [(a)] Change from not being dependent on the amplitude error of the WMAP9 Solar dipole (Sect. 5.4.1).

Sect. 5.4.1, the WMAP5 Solar dipole was underestimated by 0.28% when compared with the *Planck* best-measured amplitude, leading to an under-calibration of 0.28% in the *Planck* 2013 maps. With VLTCs included in the analysis, calibration on the orbital dipole worked as expected, and gave more accurate results, while at the same time eliminating the need to adopt the WMAP5 Solar dipole and removing the 0.28% error that it introduced in 2013.

These HFI calibration changes are summarized in Table 3. Together, they give an average shift of gain calibration of typically 1% (Planck Collaboration VIII 2016) for the three CMB channels, accounting for the previously unexplained difference in calibration on the first acoustic peak observed between HFI and WMAP.

The relative calibration between detectors operating at the same frequency is within 0.05% for 100 and 143 GHz, 0.1% at 217 GHz, and 0.4% at 353 GHz (Planck Collaboration VIII 2016). These levels for the CMB channels are within a factor of 3 of the accuracy floor set by noise in the low-ℓ polarization (Tristram et al. 2011).

The 545 and 857 GHz channels are calibrated separately using models of planetary atmospheric emission. As in 2013, we used both Neptune and Uranus. The main difference comes from better handling of the systematic errors affecting the planet flux density measurements. Analysis is now performed on the timelines, using aperture photometry, and taking into account the inhomogeneous spatial distribution of the samples. For the frequency maps, we estimate statistical errors on absolute calibration of 1.1% and 1.4% at 545 and 857 GHz, respectively, to which we add the 5% systematic uncertainty arising from the planet models. Errors on absolute calibration are therefore 6.1 and 6.4% at 545 and 857 GHz, respectively. Since the reported relative uncertainty of the models is of the order of 2%, we find the relative calibration between the two HFI high-end frequencies to be better than 3%. Relative calibration based on diffuse foreground component separation gives consistent numbers (see table 6 of Planck Collaboration X 2016). Compared to 2013, calibration factors changed by 1.9 and 4.1% at 545 and 857 GHz, respectively. Combined with other pipeline changes (such as the ADC corrections), the brightness of the released 2015 frequency maps has decreased by 1.8 and 3.3% compared to 2013.

5.4.3. Relative calibration and consistency

The relative calibration of LFI, HFI, and WMAP can be assessed on several angular scales. At $\ell = 1$, we can compare the amplitude and direction of the Solar dipole, as measured in the frequency maps of the three instruments. On smaller scales, we can compare the amplitude of the CMB fluctuations measured frequency by frequency by the three instruments, during and after component separation.

– *Comparison of independent measurements of the Solar dipole.* Table 1 gives the LFI and HFI measurements of the Solar dipole, showing agreement well within the uncertainties. The amplitudes agree within 1.2 μK (0.04%), and the directions agree within 4′. Table 1 also gives the "nominal" *Planck* dipole that has been subtracted from the *Planck* frequency maps in the 2015 release. This is a plausible combination of the LFI and HFI values, which satisfied the need for a dipole that could be subtracted uniformly across all *Planck* frequencies early in the data processing, before the final systematic uncertainties in the dipole measurements were available and a rigorous combination could be determined. See Planck Collaboration VIII (2016) Sect. 5.1 for additional measurements.

Nearly independent determinations of the Solar dipole can be extracted from individual frequency maps using component-separation methods relying on templates from low and high frequencies where foregrounds dominate (Planck Collaboration V 2016; Planck Collaboration VIII 2016). The amplitude and direction of these Solar dipole measurements can be compared with each other and with the statistical errors. This leads to relative gain calibration factors for the $\ell = 1$ mode of the maps expressed in K_{CMB} units, as shown for frequencies from 70 to 545 GHz in Table 4. For components of the signal with spectral distribution different from the CMB, a colour correction is needed to take into account the broad bands of these experiments.

– *Comparison of the residuals of the Solar dipole left in the CMB maps after removal of the best common estimate.* Another measurement of relative calibration is given by the residuals of the Solar dipole left in CMB maps after removing the best common estimate, i.e., the nominal *Planck* dipole. (See Sects. 4 and 5.4.1 for details about how the dipole and quadrupole are handled.) The residual dipole comes from two terms, as illustrated in Fig. 5, one associated with the error in direction, with an axis nearly orthogonal to the Solar dipole, and one associated with the error in amplitude aligned with the Solar dipole. Using the 857 GHz map as a dust template (extrapolated with optimized coefficients derived per patch of sky), we find residual dipoles dominated by errors orthogonal to the direction of the Solar dipole at 100 and 143 GHz, and residuals associated with calibration errors for the other frequencies. The relative residual amplitudes are given in Table 4. This shows that a minimization of the dipole residuals can and will be introduced in the HFI calibration pipeline for the final 2016 release.

– *Comparison of CMB anisotropies frequency by frequency during and after component separation.* Table 4 also shows the relative calibration between frequencies and detectors determined by `SMICA` (Planck Collaboration XV 2014; Planck Collaboration IX 2016) and `Commander` (Planck Collaboration IX 2016; Planck Collaboration X 2016), two of the map-based diffuse component-separation codes used by *Planck*. The calculation is over different multipole ranges for the two methods, so variation between the two could reflect uncertainties in transfer functions. Moreover, `Commander` uses different constraints in order to deal with the complexities and extra degrees of freedom involved in fitting foregrounds individually (see Planck Collaboration X 2016 for details), so we do not expect identical results with the two codes. Nevertheless, the agreement is excellent, at the 0.2% level between the first

Table 4. Intercalibration factors by frequency between LFI, HFI, and WMAP.

Frequency [GHz] (Detector)	Solar dipole [%] $\ell = 1$	CMB Anisotropy [%] Commander $25 \le \ell \le 100$	CMB Anisotropy [%] SMICA $50 \le \ell \le 500$
30	...	$-0.3^a \pm 0.1$	...
44	...	$0.3^a \pm 0.1$	...
70	0.04^a	$0.0^a \pm 0.1$	$0.21^a \pm 0.06$
100	0.03	0.09 ± 0.02	0.03 ± 0.02
143	0^b	$0;\ -0.1 \pm 0.1^c$	0^b
217	0.20	$0;\ 0.02 \pm 0.03^c$	0.28 ± 0.02
353	0.53	0.5 ± 0.1	0.73 ± 0.11
545	1.25	-1.0^d	1.09 ± 1.5
WMAP 23 (K)	...	0^b	...
WMAP 33 (Ka)	...	0.1 ± 0.1	...
WMAP 41 (Q)	...	0.1 ± 0.1	...
WMAP 61 (V)	...	0.2 ± 0.1	...
WMAP 94 (W)	−0.26	0.2 ± 0.1	0.28 ± 0.15

Notes. [(a)] LFI map rescaling factors that are incorporated in the beam transfer functions, as described in Planck Collaboration II (2016), have been applied. [(b)] Reference frequency; no intercalibration calculated. [(c)] For Commander at 143 GHz, detector set "ds1" was used as a reference (intercalibration factor = 0). The mean intercalibration factor for detectors ds2+5+6+7 was -0.1 ± 0.1. Similarly, at 217 GHz detector "1" was used as a reference (intercalibration factor = 0), and the mean intercalibration factor for detectors 2+3+4 was 0.02 ± 0.03. See table 6 in Planck Collaboration X (2016) for details. [(d)] For Commander, the effective recalibration of the 545 GHz channel measured in units of μK_{cmb} is the product of a multiplicative calibration factor and a unit conversion correction due to revised bandpass estimation. See Sect. 5.3 in Planck Collaboration X (2016) for details.

acoustic peak, intermediate ℓ, and dipole residuals, and with intercalibration offsets between frequencies within 0.3% of zero from 30 GHz to 217 GHz.

The following points highlight the remarkable internal consistency of the *Planck* calibration.

- The small Solar dipole residuals measured for the 100 and 143 GHz channels (<4 μK) are close to 90° away from the adopted *Planck* Solar dipole, reflecting in both cases a small 2.′8 shift in the measured direction of the dipole compared to the adopted dipole, but amplitudes (hence calibrations) within 0.1% of the adopted ("mean") value. The Commander and SMICA inter-comparisons below and on the first acoustic peak give a calibration difference between 100 and 143 GHz of ≤0.09%, confirming the very high calibration accuracy of these two channels.
- The amplitude of the Solar dipole measured by the 70 GHz channel shows a difference of 1 μK (0.03%) with respect to the best HFI Solar dipole amplitude.
- The 217, 353, and 545 GHz channels show dipole residuals aligned with the Solar dipole, which thus measure directly calibration errors with respect to 143 GHz of 0.2, 0.53, and 1.25%.
- The SMICA first peak intercalibration of 217 and 353 GHz with respect to 143 GHz shows similar intercalibration to the dipole residuals, with differences of 0.08 and 0.20%. In fact, Table 4 suggests that we can now achieve significantly better intercalibration of all CMB channels from 70 to 353 GHz.
- Comparison of the Solar dipole and first acoustic peak intercalibration factors for the 545 GHz channel gives a difference of only 0.16%. This shows that the 545 GHz channel could be calibrated using the first acoustic peak of the CMB instead of planets. Use of the planet model could then be limited to intercalibration between 545 and 857 GHz. The roughly 1% agreement between the planets and CMB absolute calibrations also shows that the current uncertainties in the absolute

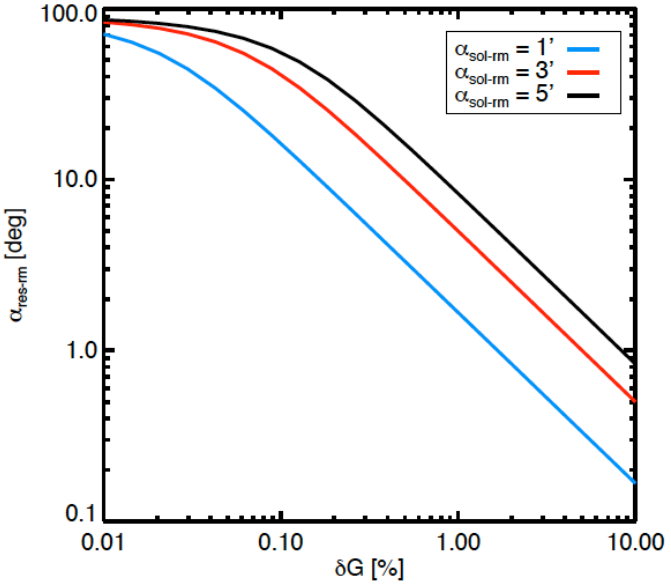

Fig. 5. Angle difference α_{res-rm} between the removed Solar dipole and the residual dipole for given errors on the dipole direction (i.e., the angle difference between the removed dipole and the true Solar dipole, α_{sol-rm}), and on the calibration ($\delta G = 1 - A_{rm}/A_{sol}$, expressed as a percentage).

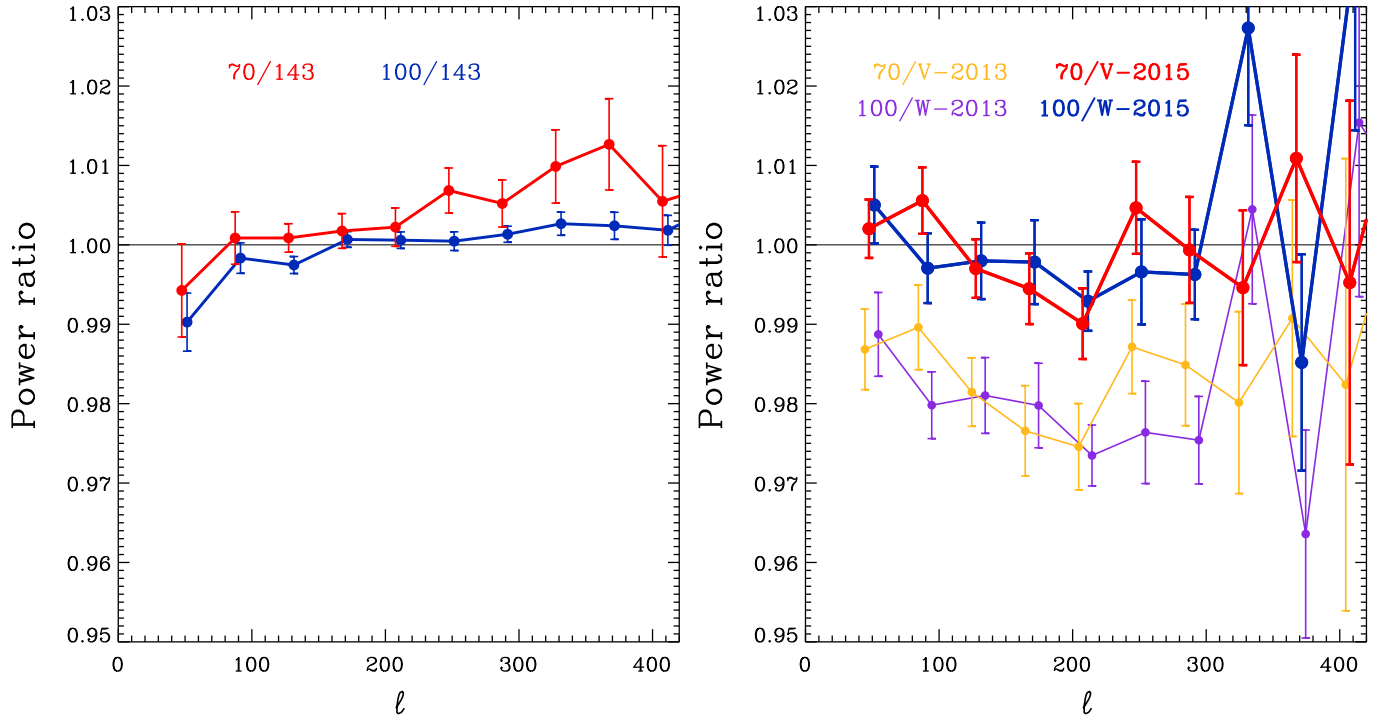

Fig. 6. Ratios of power spectra spanning the region of the first acoustic peak, uncorrected for foregrounds (which vary across the three frequencies), over 60% of the sky. The uncertainties are the errors in the mean within each $\Delta\ell = 40$ bin of the ratios computed ℓ by ℓ. *Left*: ratios of 70 and 100 GHz TT spectra to 143 GHz. The low values at $\ell = 50$ are due to diffuse foregrounds at 143 GHz. The rise to higher multipoles in the 70/143 ratio is due to discrete foregrounds. *Right*: ratio of TT spectra of *Planck* 70 and 100 GHz to WMAP V and W bands, as calculated for *Planck* 2013 data (Planck Collaboration XXXI 2014) and for the 2015 data. The near overlap of frequencies between the *Planck* and WMAP bands means that foregrounds have no appreciable effect on the ratios. The effect of the calibration changes in *Planck* between 2013 and 2015, which are discussed in this paper, is clear. There is now excellent agreement within statistical errors between *Planck* and WMAP in the region of the spectrum where both have high S/N.

calibration of the high-frequency channels, dominated by the roughly 5% error on the models, are probably overestimated.

– The intercalibration factors derived from `Commander` in all frequency bands from 70 GHz to 217 GHz are less than 0.1%. Considering all *Planck* bands from 30 GHz to 353 GHz, they are within 0.5%.

This comparison can also be made at the power spectrum level. The left-hand panel in Fig. 6 compares the 70, 100, and 143 GHz channels of LFI and HFI in the multipole range of the first acoustic peak, $50 < \ell < 500$, uncorrected for foregrounds, over 60% of the sky. The low values at $\ell = 50$ show the effect of unremoved diffuse foregrounds at 143 GHz, and the rise of the 70/143 ratio is at least partly driven by unremoved discrete foregrounds; the uncertainties are larger at 70 GHz as well. In the middle region, the agreement is very good, at a level of a few tenths of a percent. This result is a direct test that all systematic effects in calibration have been corrected on both instruments to better than this value.

The right-hand panel of Fig. 6 shows the ratios of *Planck* TT spectra at 70 and 100 GHz to those of WMAP in the V and W bands, as calculated for *Planck* 2013 data (Planck Collaboration XXXI 2014) and for the 2015 data. While the scatter is significantly larger than that in the left-hand panel, due to the higher noise in WMAP, the agreement is very good, and within the statistical errors. We can now say that within the uncertainties, LFI, HFI, and WMAP agree, and the difference seen in the 2013 data (Planck Collaboration XXXI 2014) is gone.

5.4.4. Summary of calibration

The *Planck* 70 and 100 GHz channels belong to instruments based on different technologies, with different systematic effects, and operating close to the minimum of the diffuse foregrounds. They thus provide a very good test of the consistency of calibration and transfer functions. The internal consistency between LFI and HFI is remarkable. Figure 6 represents a stringent test of calibration, systematic effects, beams, and transfer functions, and demonstrates overall consistency at a level of a few parts per thousand between independent instruments and spacecraft.

The *Planck* CMB-channels from 70 to 217 GHz show calibration differences below 0.3%, measured from both residual dipoles and the first acoustic peak. Using a Solar dipole reference established on the 100 and 143 GHz channels, it is likely that all detectors could be inter-calibrated to 0.05% in subsequent data processing versions. The agreement of the measured calibration factors from dipole residuals ($\ell = 1$) and the first acoustic peak ($\ell \approx 200$) shows that the transfer functions are controlled to better than 0.2% in this multipole range. Corrections for systematic effects in HFI cover a dynamic range from detector to detector larger than 2 at 100 and 143 GHz, but have reduced the calibration errors by an order of magnitude. This suggests that the corrections lead now to an absolute photometric calibration accuracy on the orbital dipole (limited only by systematics and noise) of 0.1%.

As in other instances in the *Planck* data processing, when very small systematic effects are detected and measured in a posteriori characterization, their removal from the data is complicated. Their determinations are often degenerate, and complete

Table 5. Main characteristics of LFI full mission maps.

Characteristic	Frequency band		
	30 GHz	44 GHz	70 GHz
Centre frequency [GHz]	28.4	44.1	70.4
Effective beam FWHM[a] [arcmin]	32.29	27.00	13.21
Effective beam ellipticity[a]	1.32	1.04	1.22
Temperature noise (1°)[b] [μK_{CMB}]	2.5	2.7	3.5
Polarization noise (Q and U; 1°)[b] [μK_{CMB}]	3.5	4.0	5.0
Overall calibration uncertainty[c] [%]	0.35	0.26	0.20
Systematic effects uncertainty in Stokes I^d [μK_{CMB}]	0.19	0.39	0.40
Systematic effects uncertainty in Stokes Q^d [μK_{CMB}]	0.20	0.23	0.45
Systematic effects uncertainty in Stokes U^d [μK_{CMB}]	0.40	0.45	0.44

Notes. [(a)] Calculated from the main beam solid angle of the effective beam, Ω_{eff} = mean(Ω). These values are used in the source extraction pipeline (Planck Collaboration XXVI 2016). [(b)] Noise rms computed after smoothing to 1°. [(c)] Sum of the error determined from the absolute and relative calibration, see Planck Collaboration IV (2016). [(d)] Estimated rms values over the full sky and after full mission integration. Not included here are gain reconstruction uncertainties, estimated to be of order 0.1%.

reprocessing is necessary. The calibration improvement demonstrated by the minimization of the dipole residuals using the 857 GHz dust template will be introduced in a self-consistent way in the HFI calibration pipeline and overall processing for the final 2016 release. Furthermore, the use of the Solar dipole parameters from the best *Planck* CMB channels (100 and 143 GHz) will be introduced in the processing of the channels more affected by foregrounds and noise. The LFI calibration accuracy is now close to noise-limited, but improvements will be made in 2016 according to a complete simulation plan to improve our understanding of calibration and systematics affecting low multipoles, particularly for polarization analysis.

6. Timelines

For the first time, the 2015 *Planck* release includes time series of the observations acquired by individual detectors in LFI and HFI (see Planck Collaboration II 2016 and Planck Collaboration VII 2016 for details). These timelines will be of use for those wishing to construct maps using specific time periods or mapmaking algorithms.

The delivered timelines have been cleaned of all major instrumental systematic effects. For LFI timelines, this cleaning means that the raw timelines are ADC-corrected, despiked, and demodulated; furthermore, the raw diode outputs (two per receiver) are combined and gain regularization is applied before calibration. For HFI timelines, this cleaning means that the raw timelines are ADC-corrected, demodulated, despiked, corrected for rare baseline jumps, and a dark template has been removed; they are converted to absorbed power units, and the time transfer function has been deconvolved.

The timelines are calibrated to astrophysical units and corrected for a zero-point value (determined at map level). The Solar and orbital dipole signals have been removed. In addition, for LFI, an estimation of Galactic stray light has been removed.

The timelines still contain the low-frequency noise that is later removed by destriping at the mapmaking stage. However, sets of offsets are provided (determined during mapmaking), which can be used to convert the calibrated timelines to maps without destriping. For LFI, the offsets are computed every 0.246, 0.988, and 1.000 s for the 30, 44, and 70 GHz channels, respectively, using the full mission data and all valid detectors per channel. These offsets are used to produce the full-mission LFI maps. For shorter period maps, different offsets are used that optimize noise cross-correlation effects; these are not delivered. For HFI, a single offset per ring is determined during mapmaking using the full mission data set and all valid detectors per channel. These offsets are then applied to all maps produced using any fraction of the mission (year, survey) or any subset of detectors (single detector, detector set).

The timelines are accompanied by flags that determine which data have been used for mapmaking, as well as pointing timelines, which are sampled at the same frequency as the data themselves.

7. Frequency maps

Figures 7 and 8 show the *Planck* 2015 maps. Note that *Planck* uses `HEALPix` (Górski et al. 2005) as its basic representation scheme for maps, with resolution labelled by the N_{side} value.

7.1. Mapmaking

7.1.1. LFI

Mapmaking takes as input the calibrated timelines, from which the cosmological and orbital dipole signals have been removed. An estimate of Galactic stray light is subtracted from the timelines prior to mapmaking, since this is difficult to correct at map level. As for the 2013 release, the LFI maps are produced using the `Madam` destriping code (Keihänen et al. 2010), enhanced with a noise prior, which enables accurate removal of correlated $1/f$ noise, while simultaneously minimizing systematic errors by judicious use of masks. The production of maps and covariance matrices is validated using the FFP8 simulations. The output of the code consists of sky maps of temperature and Stokes Q and U polarization, and a statistical description of residual noise in the maps in the form of pixel-pixel noise covariance matrices. These matrices are produced at N_{side} = 64. In addition to full-mission maps at both high and low resolution (N_{side} = 16), many other types of maps are produced, including those from single horns, single radiometers, single surveys, odd and even surveys, single years, and halves of the mission. The LFI maps are not corrected for beam shape, so that point sources in the map have

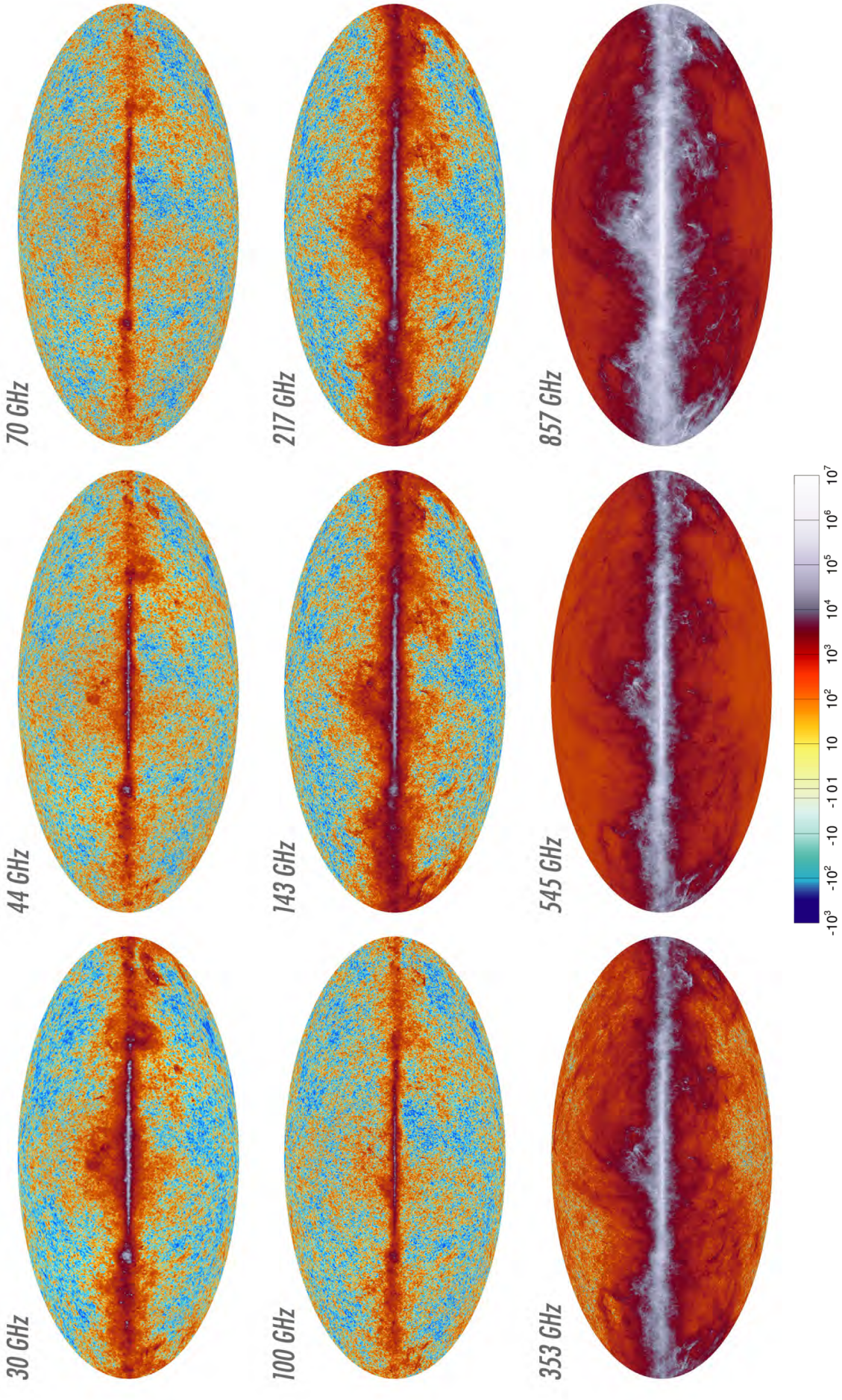

Fig. 7. The nine *Planck* frequency maps from 30 to 857 GHz. The colour scale (identical to the one used in 2013), based on inversion of the function $y = 10^x - 10^{-x}$, is tailored to show the full dynamic range of the maps.

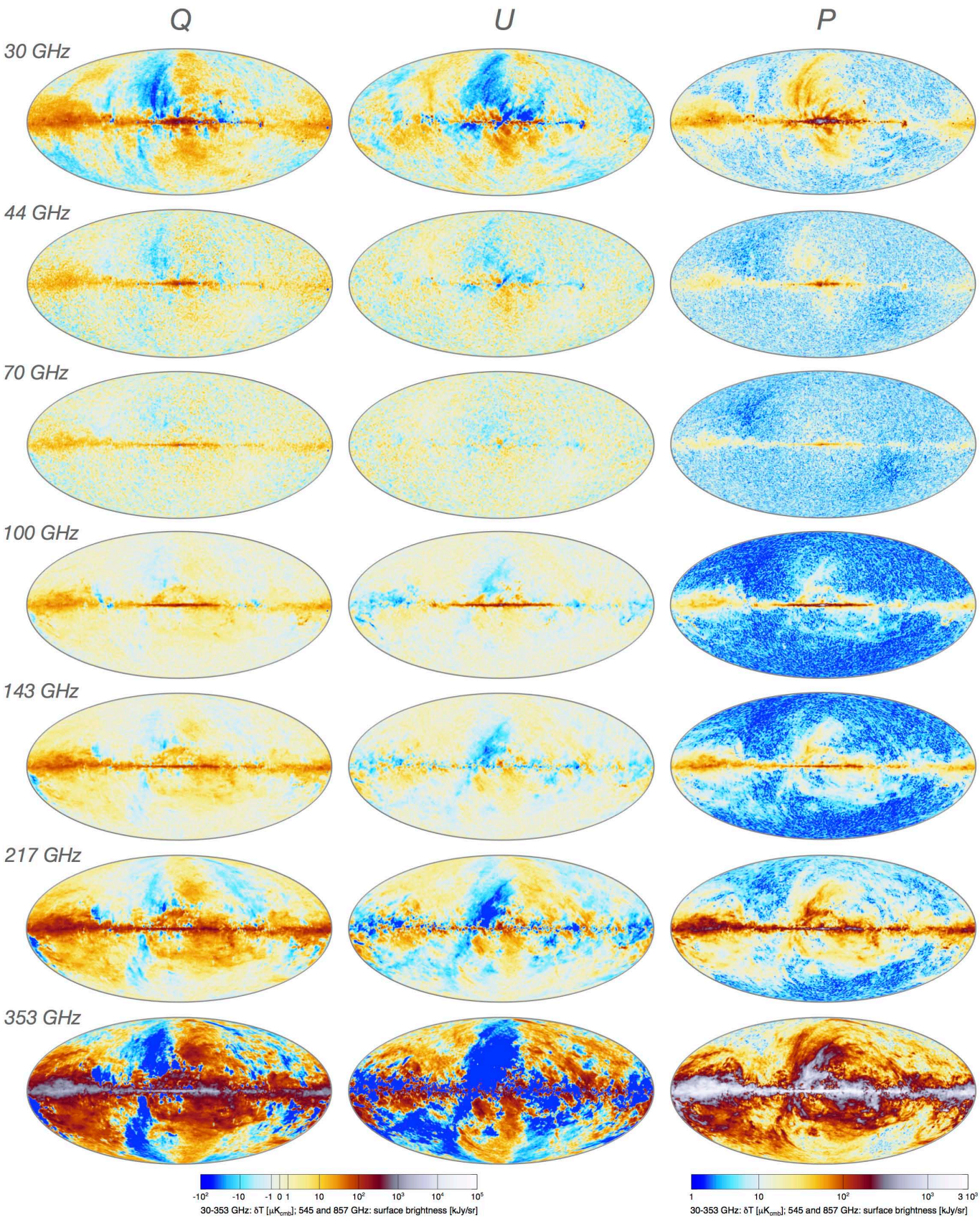

Fig. 8. The seven *Planck* polarization maps from 30 to 353 GHz, shown in Stokes Q and U, and in total polarized intensity (P). All maps are corrected for temperature-to-polarization leakage due to bandpass mismatch. The colour scale uses the same function as in Fig. 7, but the range limits have been adjusted.

Table 6. Main characteristics of HFI full mission maps.

Characteristic	Reference frequency ν [GHz]						Notes
	100	143	217	353	545	857	
Number of bolometers	8	11	12	12	3	4	$a1$
Effective beam FWHM$_1$ [arcmin]	9.68	7.30	5.02	4.94	4.83	4.64	$b1$
Effective beam FWHM$_2$ [arcmin]	9.66	7.22	4.90	4.92	4.67	4.22	$b2$
Effective beam ellipticity ϵ	1.186	1.040	1.169	1.166	1.137	1.336	$b3$
Noise per beam solid angle [μK$_{\rm CMB}$]	7.5	4.3	8.7	29.7			$c1$
[kJy sr^{-1}]					9.1	8.8	$c1$
Temperature noise [μK$_{\rm CMB}$ deg]	1.29	0.55	0.78	2.56			$c2$
[kJy sr^{-1} deg]					0.78	0.72	$c2$
Polarization noise (Q and U) [μK$_{\rm CMB}$ deg]	1.96	1.17	1.75	7.31			$c3$
Calibration accuracy [%]	0.09	0.07	0.16	0.78	1.1(+5)	1.4(+5)	d
CIB monopole prediction [MJy sr^{-1}]	0.0030	0.0079	0.033	0.13	0.35	0.64	e
Zodiacal light level correction [K$_{\rm CMB}$]	4.3×10^{-7}	9.4×10^{-7}	3.8×10^{-6}	3.4×10^{-5}			$e2$
[MJy sr^{-1}]					0.04	0.12	$e2$

Notes. $^{(a1)}$ Number of bolometers whose data were used in producing the channel map. $^{(b1)}$ FWHM$_1$ is the FWHM of the Gaussian whose solid angle is equivalent to that of the effective beams. $^{(b2)}$ FWHM$_2$ is the FWHM of the elliptical Gaussian fit. $^{(b3)}$ Ratio of the major to minor axis of the best-fit Gaussian averaged over the full sky. $^{(c1)}$ Estimate of the noise per beam solid angle, as given in $b1$. $^{(c2)}$ Estimate of the noise in intensity, scaled to 1°, assuming that the noise is white. $^{(c3)}$ Estimate of the noise in polarization, scaled to 1°, assuming that the noise is white. $^{(d)}$ Calibration accuracy (at 545 and 857 GHz, the 5% accounts for the model uncertainty). $^{(e)}$ According to the Béthermin et al. (2012) model, whose uncertainty is estimated to be at the 20% level (also for constant νI_ν). $^{(e2)}$ Zero-level correction to be applied on zodiacal-light corrected maps.

the shape of the effective beam at that location. Zero-levels are estimated by fitting a cosecant-law Galactic latitude model to the CMB-subtracted maps, and subtracting this from the maps. The polarization maps must be corrected for bandpass leakage through multiplication with leakage template maps, which are estimated via a process similar to component separation.

A summary of the characteristics of the LFI maps is presented in Table 5.

7.1.2. HFI

As for the *Planck* 2013 release, the measurements in each `HEALPix` pixel visited during a stable pointing period (i.e., "ring") are averaged for each detector, keeping track of the bolometer orientations on the sky. The calibration and mapmaking operations use this intermediate product as an input. For each detector, the TOIs are only modified by a single offset value per ring, determined using the destriping method described in Tristram et al. (2011). The offsets are computed simultaneously for all bolometers at a given frequency, using the full mission data. For a given bolometer, the same offset per ring is applied whatever the map (e.g., full-mission, half-mission, detector-set maps; but for half-ring maps, see Planck Collaboration VII 2016). Each data sample is calibrated in $K_{\rm CMB}$ for the 100, 143, 217, and 353 GHz channels, and MJy sr^{-1} (assuming νI_ν = constant) for the 545 and 857 GHz channels, using the calibration scheme presented in Sect. 5.4.2. Unlike in the 2013 release, the bolometer gains are assumed to be constant throughout the mission. The final mapmaking is a simple projection of each unflagged sample to the nearest grid pixel. For polarization data, when several detectors are solved for simultaneously, the polarization mapmaking equation is inverted on a per-pixel basis (Planck Collaboration VII 2016).

The products of the HFI mapmaking pipelines are pixelized maps of I, Q, and U, together with their covariances. Map resolution is $N_{\rm side}$ = 2048, and the pixel size is 1.′7. The basic characteristics of the maps are given in Table 6. For details, see (Planck Collaboration VII 2016).

Maps are cleaned for the zodiacal light component, which varies in time, based on templates fitted to the survey difference maps (see Planck Collaboration XIV 2014). These templates are systematically subtracted prior to mapmaking. The *Planck* total dipole (Solar and orbital) is computed and also subtracted from the data. In contrast to 2013, the far sidelobes (FSL) are not removed from the maps.

The 2015 HFI maps delivered via the PLA have had zodiacal light removed, and include CIB emission. In addition, the zero level of the temperature maps has been adjusted for Galactic emission. However, the zero level adjustment was based on maps that contained zodiacal light, and therefore the released maps require an additional frequency-dependent correction that must be applied manually. For work requiring all astrophysical sources of emission to be present in the maps, the "Zodiacal light level correction" ("e2" in the "Notes" column of Table 6) must be added to the maps. For work requiring Galactic emission only, the "e2" corrections should be added to the maps, but the "CIB monopole prediction" ("e" in the "Notes" column) should be removed.

8. CMB products

8.1. CMB maps

As for the *Planck* 2013 release, we use four different methods to separate the *Planck* 2015 frequency maps into physical components (Planck Collaboration IX 2016). The four methods

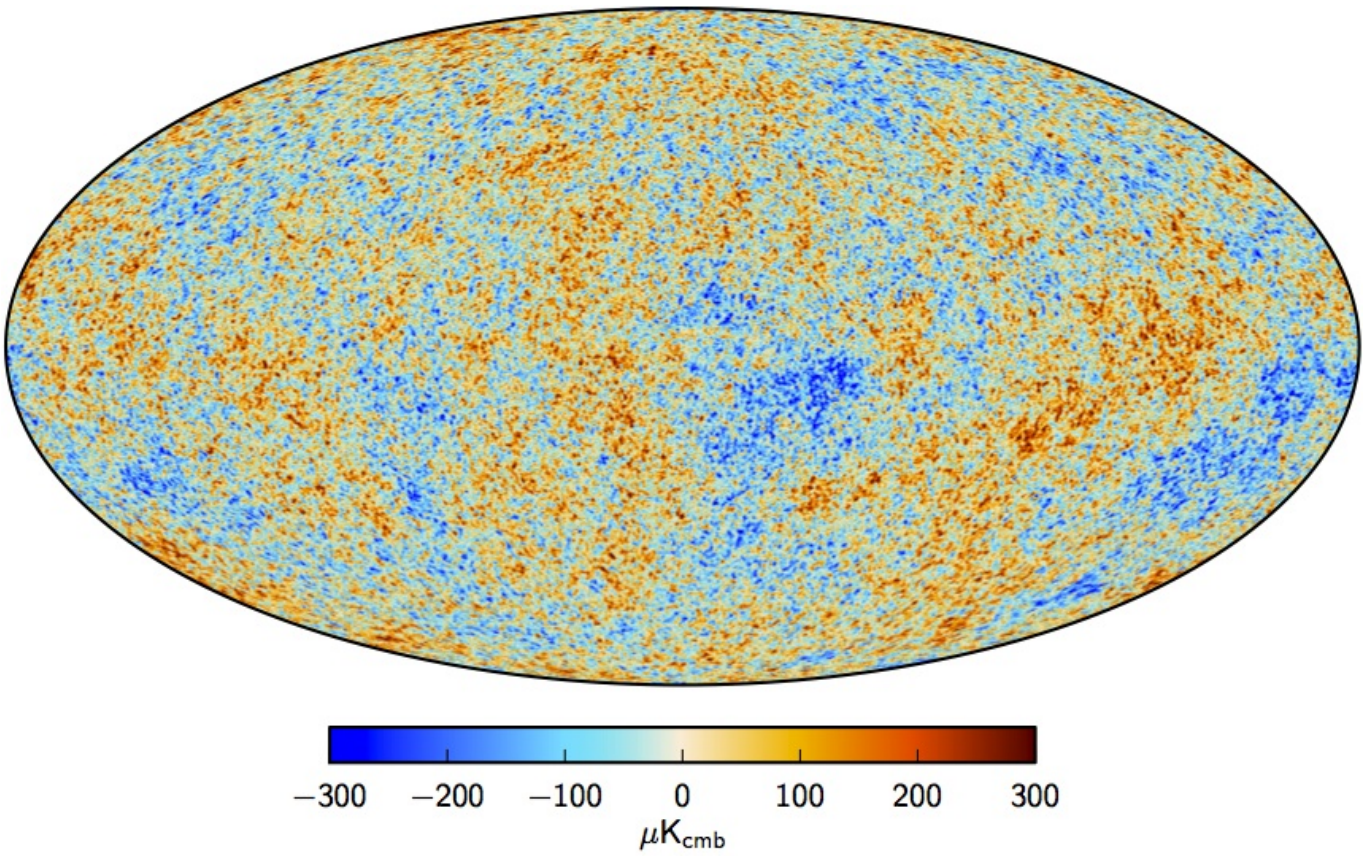

Fig. 9. Maximum posterior CMB intensity map at 5′ resolution derived from the joint baseline analysis of *Planck*, WMAP, and 408 MHz observations. A small strip of the Galactic plane, covering 1.6% of the sky, is filled in by a constrained realization that has the same statistical properties as the rest of the sky (Planck Collaboration IX 2016).

are: SMICA, which uses an independent component analysis of power spectra (Delabrouille et al. 2003; Cardoso et al. 2008); NILC, a needlet-based internal linear combination approach (Delabrouille et al. 2009); Commander, a pixel-based parameter and template fitting procedure with Gibbs sampling (Eriksen et al. 2006, 2008); and SEVEM, which employs template fitting (Fernández-Cobos et al. 2012). The methods used are conceptually the same as in 2013, but we now apply them independently to the temperature and polarization maps. Similarly to what was done in 2013, simulations (in this case FFP8, Planck Collaboration XII 2016) are used to test the methods and estimate uncertainties in the recovery of components.

All four methods produce CMB maps in Stokes I, Q, and U. In addition, Commander and SMICA separate diffuse astrophysical "foregrounds" characterized by their different spectral signatures. Commander does so by fitting physical models of these foregrounds and the CMB to the sky, whereas SMICA extracts a fixed set of independent components representing CMB, foregrounds, and noise. Typically, SMICA assumes that two "foregrounds" are present at low and high frequencies, respectively. An important change in the implementation of Commander in 2015 is in the input maps used, which now include detector-level maps rather than maps that combine all detectors at a given frequency, a map of 408 MHz emission, and the 9 yr WMAP maps. The significant increase in the number of input maps allows Commander to control much better several factors, such as relative calibration and the frequency response of individual channels, and to extract a larger number of foreground temperature components, now matching those that are expected to be present in the sky.

The 2015 *Planck* CMB temperature maps produced by all four methods (see an example in Fig. 9) have significantly lower noise than those produced in 2013 (by a factor of 1.3). They are used mainly for non-Gaussianity analysis (Planck Collaboration XVII 2016; Planck Collaboration XVI 2016) and for the extraction of lensing deflection maps (Planck Collaboration XV 2016). For these analyses, all four methods are considered to give equivalently robust results, and the dispersion between the four gives a reasonable estimate of the uncertainty of the CMB recovery. We emphasize, however, that these maps are not cleaned of high-ℓ foregrounds, such as unresolved extragalactic sources, or of SZ emission. Although the strongest compact sources are removed through a masking procedure based on optimal filters such as Mexican Hat wavelets, unresolved sources escaping this process introduce small-scale power beyond $\ell \approx 2000$, which if uncorrected will bias cosmological parameters. Cosmological analyses using small angular scales must therefore take care to marginalize over such foregrounds as appropriate (see Planck Collaboration IX 2016 and Planck Collaboration XIII 2016).

Although the statistical properties of these maps give good results when used to fit cosmological models, the best *Planck* 2015 cosmological parameters are derived from a likelihood code that allows more detailed tuning of the contribution of individual frequencies and ℓ-by-ℓ removal of foregrounds (Planck Collaboration XIII 2016).

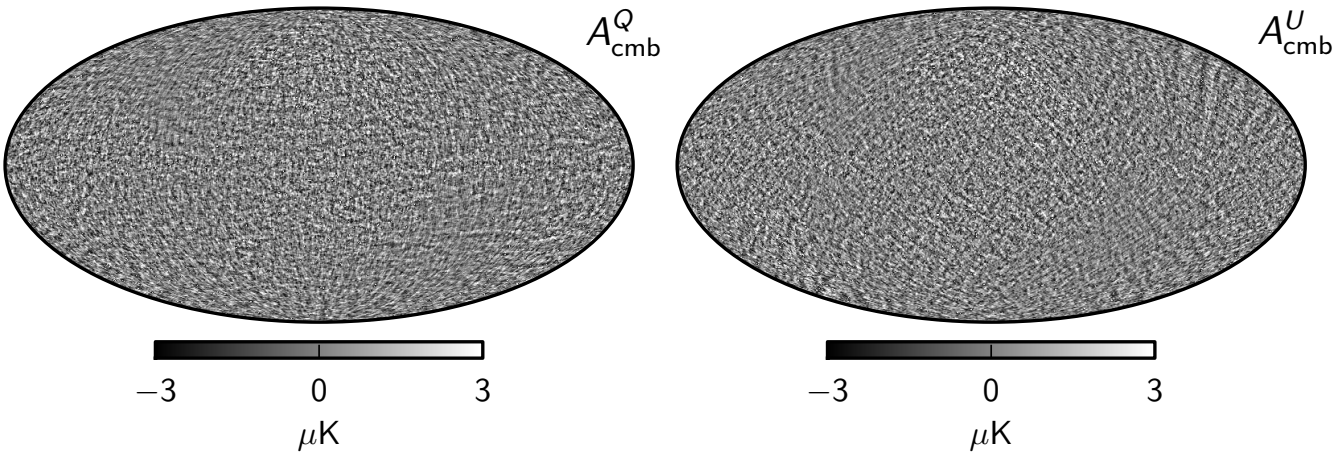

Fig. 10. Maximum posterior amplitude Stokes Q (*left*) and U (*right*) maps derived from *Planck* observations between 30 and 353 GHz. These maps have been highpass-filtered with a cosine-apodized filter between $\ell = 20$ and 40, and a 17% region of the Galactic plane has been replaced with a constrained Gaussian realization (Planck Collaboration IX 2016). From Planck Collaboration X (2016).

A low-resolution version of the Commander map is also used in the pixel-based low-ℓ likelihood component of our best-fit 2015 cosmology (Planck Collaboration XI 2016).

In polarization, the CMB maps resulting from the 2015 *Planck* component-separation methods represent a dramatic advance in terms of coverage, angular resolution, and sensitivity. Nonetheless, they suffer from a significant level of anomalous features at large angular scales, arising from corresponding systematic effects in the input frequency maps between 100 and 217 GHz. The characterization of these systematic effects is ongoing, and it is currently suspected that low-level spurious signals are also present at intermediate angular scales (Planck Collaboration VII 2016; Planck Collaboration VIII 2016). For this reason, the CMB polarization maps presented here have been highpass-filtered with a cosine-apodized filter between $\ell = 20$ and 40 (Fig. 10). They are used only for a very limited number of cosmological analyses, which have been shown to be immune to the undesired features still present: estimation of primordial non-Gaussianity levels (Planck Collaboration XVII 2016); stacking analysis (Planck Collaboration XVI 2016); estimation of primordial magnetic field levels (Planck Collaboration XIX 2016); and estimation of lensing potential (Planck Collaboration XV 2016).

In contrast, the low-ℓ polarization likelihood used in Planck Collaboration XIII (2016) is based exclusively on the 70 GHz polarization map, cleaned of foregrounds by use of the 30 and 353 GHz polarization maps. Both of these frequencies have been shown to be free of the kind of systematic errors that still affect intermediate frequencies (Planck Collaboration II 2016; Planck Collaboration VIII 2016).

8.2. CMB power spectra

The foreground-subtracted, frequency-averaged, cross-half-mission TT spectrum is plotted in Fig. 11, together with the Commander power spectrum at multipoles $\ell < 29$. The figure also shows the best-fit base ΛCDM theoretical spectrum fitted to the PlanckTT+lowP likelihood, together with residuals (bottom panel) and $\pm1\sigma$ uncertainties. Note that we use the notation "PlanckTT" when we are referring to the likelihood deriving from the TT spectrum, and so on.

8.2.1. Polarization power spectra

In addition to the TT spectra, the 2015 *Planck* likelihood includes the TE and EE spectra, shown in Fig. 12. The theory curve in Fig. 12 is the best-fit base ΛCDM model fitted to the temperature spectra using the PlanckTT+lowP likelihood. The residuals are higher than expected from noise alone, and provide evidence of residual systematic errors in the TE and EE spectra. It is currently believed that the dominant source of such errors is beam mismatch generating leakage from temperature to polarization at the level of a few μK^2 in $\mathcal{D}_\ell$. We urge caution in the interpretation of any features in these spectra, which should be viewed as work in progress. Nonetheless, we find a high level of consistency in results between the PlanckTT and the full TT+TE+EE likelihoods. Furthermore, the cosmological parameters (which do not depend strongly on τ) derived from the TE spectra have comparable errors to the TT-derived parameters, and they are consistent typically within 0.5σ or better.

8.2.2. Number of modes

One way of assessing the constraining power contained in a particular measurement of CMB anisotropies is to determine the effective number of $a_{\ell m}$ modes that have been measured. This is equivalent to estimating 2 times the square of the total S/N in the power spectra, a measure that contains *all* the available cosmological information if we assume that the anisotropies are purely Gaussian (and hence ignore all non-Gaussian information coming from lensing, the CIB, cross-correlations with other probes, etc.). Carrying out this procedure for the *Planck* 2013 TT power spectrum data provided in Planck Collaboration XV (2014) and Planck Collaboration XVI (2014) yields the number 826 000 (which includes the effects of instrumental noise, cosmic variance, and masking). The 2015 TT data have increased this value to 1 114 000, with TE and EE adding a further 60 000 and 96 000 modes, respectively[6]. From this perspective the 2015 *Planck* data constrain approximately 55% more modes than in the 2013 release. Of course this is not the whole story, since some pieces of information are more valuable than others, and in fact *Planck* is able to place considerably tighter constraints on

[6] Here we have used the basic (and conservative) likelihood; more modes are effectively probed by *Planck* if one includes larger sky fractions.

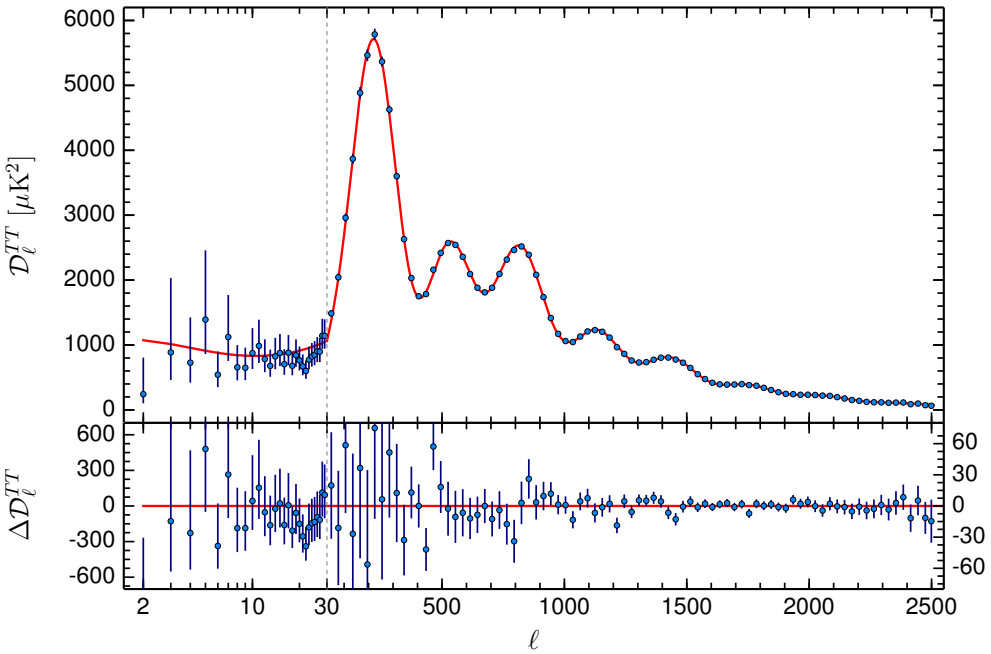

Fig. 11. *Planck* 2015 temperature power spectrum. At multipoles $\ell \geq 30$, we show the maximum-likelihood, frequency-averaged temperature spectrum computed from the cross-half-mission likelihood, with foreground and other nuisance parameters determined from the MCMC analysis of the base ΛCDM cosmology. In the multipole range $2 \leq \ell \leq 29$, we plot the power spectrum from the `Commander` component-separation algorithm computed over 94% of the sky. The best-fit base ΛCDM theoretical spectrum fitted to the PlanckTT+lowP likelihood is plotted in the *upper panel*. Residuals with respect to this model are shown in the *lower panel*. The error bars show $\pm 1\sigma$ uncertainties. From Planck Collaboration XIII (2016).

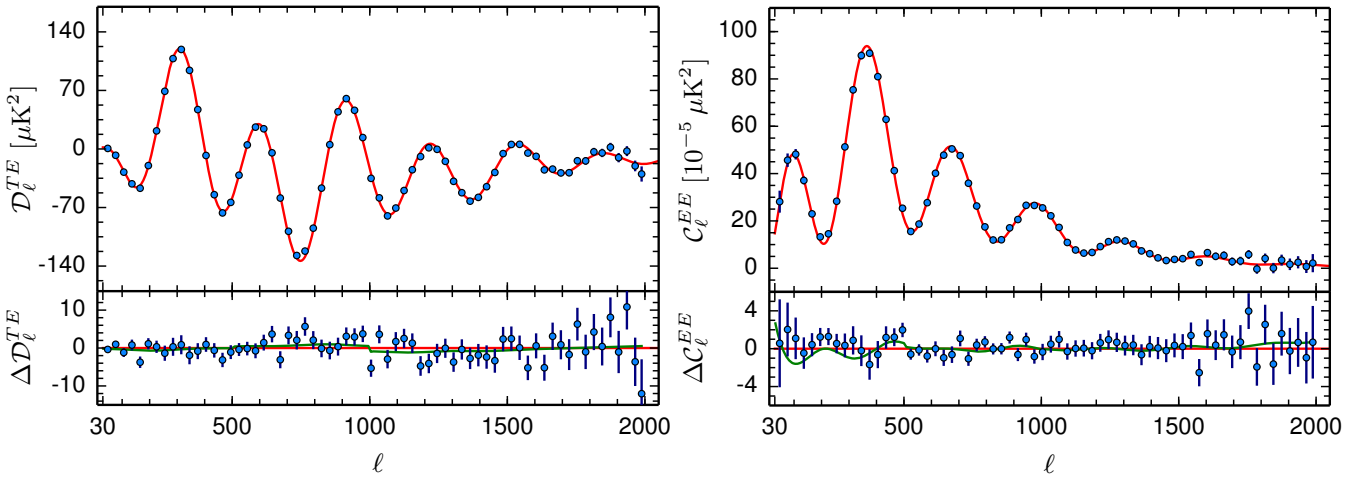

Fig. 12. Frequency-averaged TE (*left*) and EE (*right*) spectra, not corrected for T-to-P leakage (see text). The theoretical TE and EE spectra plotted in the *upper panels* are computed from the best-fit model of Fig. 11. Residuals with respect to this theoretical model are shown in the *lower panels*. The error bars show $\pm 1\sigma$ uncertainties. The green lines in the lower panels show the best-fit temperature-to-polarization leakage model, fitted separately to the TE and EE spectra. From Planck Collaboration XIII (2016).

particular parameters (e.g., reionization optical depth or certain extensions to the base ΛCDM model) by including new polarization data.

8.2.3. Peaks in the power spectra

The fidelity with which *Planck* has measured the C_ℓ^{TT}, C_ℓ^{TE}, and C_ℓ^{EE} power spectra enables us to estimate precisely the underlying cosmological parameters (see Sect. 10), but the C_ℓs are themselves a set of cosmological observables, whose properties can be described independently of any model. The acoustic peaks in the C_ℓs reveal the underlying physics of oscillating sound waves in the coupled photon-baryon fluid, driven by dark matter potential perturbations, and one can talk about the fundamental mode, the first harmonic, and so on. Hence it is natural to ask about the positions of the individual peaks in the power spectra as empirical information that becomes part of the canon of facts now known about our Universe.

Here we use the *Planck* data directly to fit for the multipoles of individual features in the measured TT, TE, and EE power spectra. We specifically use the CMB-only bandpowers given in Planck Collaboration XI (2016), adopting the same weighting scheme within each bin. Fitting for the positions and amplitudes of features in the bandpowers is a topic with a long history, with approaches becoming more sophisticated as the fidelity of the

Table 7. *Planck* power spectra peak positions and amplitudes.

Peak		
Number	Position [ℓ]	Amplitude [μK^2]
TT power spectrum		
First	220.0 ± 0.5	5717 ± 35
Second	537.5 ± 0.7	2582 ± 11
Third	810.8 ± 0.7	2523 ± 10
Fourth	1120.9 ± 1.0	1237 ± 4
Fifth	1444.2 ± 1.1	797.1 ± 3.1
Sixth	1776 ± 5	377.4 ± 2.9
Seventh	2081 ± 25	214 ± 4
Eighth	2395 ± 24	105 ± 4
TE power spectrum		
First	308.5 ± 0.4	115.9 ± 1.1
Second	595.3 ± 0.7	28.6 ± 1.1
Third	916.9 ± 0.5	58.4 ± 1.0
Fourth	1224 ± 1.0	0.7 ± 0.5
Fifth	1536 ± 2.8	5.6 ± 1.3
Sixth	1861 ± 4	1.2 ± 1.0
EE power spectrum		
First	137 ± 6	1.15 ± 0.07
Second	397.2 ± 0.5	22.04 ± 0.14
Third	690.8 ± 0.6	37.35 ± 0.25
Fourth	992.1 ± 1.3	41.8 ± 0.5
Fifth	1296 ± 4	31.6 ± 1.0

data has improved (e.g., Scott & White 1994; Hancock & Rocha 1997; Knox & Page 2000; de Bernardis et al. 2002; Bond et al. 2003; Page et al. 2003; Durrer et al. 2003; Readhead et al. 2004; Jones et al. 2006; Hinshaw et al. 2007; Corasaniti & Melchiorri 2008; Pryke et al. 2009). Following earlier approaches, we fit Gaussians to the peaks in C_ℓ^{TT} and C_ℓ^{EE}, but parabolas to the peaks in C_ℓ^{TE}. We have to remove a featureless damping tail to fit the higher C_ℓ^{TT} region, and care has to be taken to treat the lowest-ℓ "recombination" peak in C_ℓ^{EE}. We explicitly focus on peaks (ignoring the troughs) in the conventional quantity $\mathcal{D}_\ell \equiv \ell(\ell+1)C_\ell/2\pi$; note that other quantities (e.g., C_ℓ) will have maxima at slightly different multipoles, and that the choice of bandpowers to use for fitting each peak is somewhat subjective. Our numerical values, presented in in Table 7, are consistent with previous estimates, but with a dramatically increased number of peaks measured. *Planck* detects 19 peaks (including marginal detection of the eighth C_ℓ^{TT} peak), and an essentially equivalent number of troughs.

8.3. CMB lensing products

Planck is the first experiment with the sky coverage, angular resolution, and sensitivity to form a full-sky reconstruction of the projected mass, along every line of sight back to the surface of last scattering. Figure 13 shows the 2015 *Planck* lensing map (Planck Collaboration XV 2016), which uses as input the CMB maps produced by the SMICA code. The map combines five possible quadratic estimators based on the various correlations of the CMB temperature (T) and polarization (E and B).

8.4. Likelihood code

8.4.1. CMB likelihood

We adopt the same general methodology for the 2015 likelihood as in 2013, extended to include *Planck* polarization data. The likelihood is a hybrid combination of a low-multipole pixel-based likelihood with a high-multipole likelihood constructed from cross-spectra (see Planck Collaboration XI 2016 for details).

At low multipoles we now use *Planck* instead of WMAP for polarization information. The 70 GHz LFI polarization maps are cleaned with the LFI 30 GHz and HFI 353 GHz maps to mitigate foreground contamination. Based on null tests, these cleaned polarization maps are then used over 46% of the sky to construct the low-multipole likelihood (referred to as "lowP"). The Commander temperature solution, constructed from all *Planck* frequency maps, together with the Haslam 408 MHz and WMAP maps, is used over 93% of the sky. The temperature and polarization data are then treated in a unified, low-resolution, pixel-based manner for the multipole range $2 \le \ell \le 29$.

The high-ℓ likelihood uses pseudo-C_ℓ cross-spectra from HFI 100, 143, and 217 GHz maps in a "fiducial Gaussian" approximation, employing analytic covariance matrices calculated for a fiducial cosmological model. Unresolved foregrounds are modelled parametrically using power spectrum templates, with only minor changes to the model adopted in the 2013 analysis. To reduce any possible biases from co-temporal systematics, the baseline high-multipole likelihood uses cross-spectra between frequency maps constructed from the first and second halves of the full mission data. We also make more aggressive use of sky at all frequencies in the 2015 analysis. The most significant change is the addition of the option to include the TE and EE power spectra and the associated covariance matrices into the scheme, to form a combined TT, TE, EE likelihood at high multipoles (referred to as PlanckTT,TE,EE). Although we find firm evidence for systematics associated with temperature-to-polarization leakage in the TE and EE spectra, these systematics are at low levels. We find a high degree of consistency between the TT, TE, and EE spectra for the cosmological models analysed in the 2015 *Planck* papers; however, in this data release, we regard the combined TT, TE, and EE *Planck* results as preliminary and hence recommend the TT likelihood as the baseline.

8.4.2. Lensing likelihood

Our power spectrum measurement constrains the lensing potential power spectrum to a precision of ±2.5%, corresponding to a 1.2% constraint on the overall amplitude of matter fluctuations (σ_8), a measurement with considerable power for constraining cosmology. We have constructed two Gaussian bandpower likelihoods based on the lensing power spectrum measurement, plotted in Fig. 20. The first likelihood uses a conservative bandpower range, $40 \le L \le 400$, with linear binning, following the temperature-only likelihood released in 2013. The second likelihood uses a more aggressive range with $8 \le L \le 2048$, and bins that are linear in $L^{0.6}$. Both likelihoods combine temperature and polarization data. We incorporate uncertainties in the estimator normalization and bias corrections directly into the likelihood, using pre-calculated derivatives of these terms with respect to the CMB temperature and polarization power spectra. The construction of the lensing likelihood is described in Planck Collaboration XV (2016), and its cosmological implications are discussed in detail in Planck Collaboration XIII (2016).

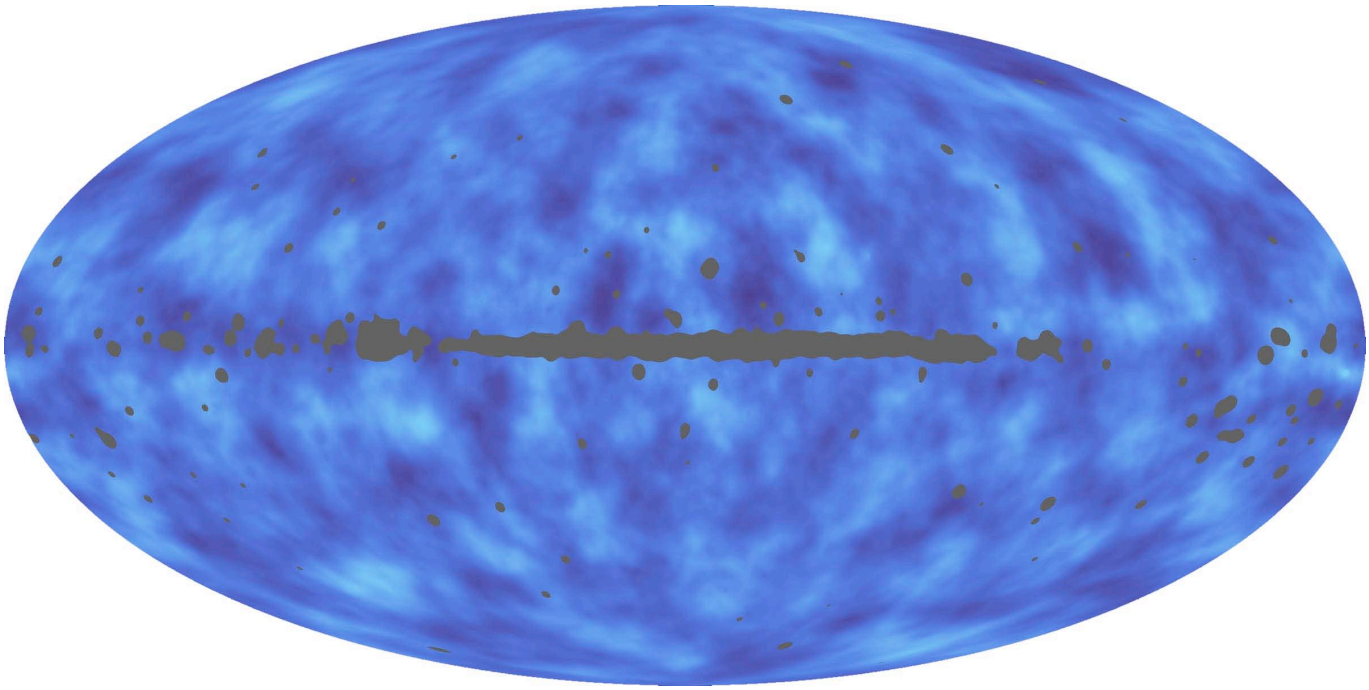

Fig. 13. Wiener-filtered lensing potential estimate with minimal masking (using the SMICA component-separated map), in Mollweide projection in Galactic coordinates (Planck Collaboration XV 2016). The reconstruction has been band-limited to $8 \leq L \leq 2048$ (where, following convention, L is used as the multipole index in the lensing power spectrum).

9. Astrophysics products

9.1. The Second Planck Catalogue of Compact Sources

The Second Planck Catalogue of Compact Sources (PCCS2; Planck Collaboration XXVI 2016) is the catalogue of sources detected from the full duration of *Planck* operations, referred to as the "extended" mission. It comprises compact Galactic and extragalactic sources detected over the entire sky. Compact sources are detected in the single-frequency maps and assigned to one of two sub-catalogues, the PCCS2 or PCCS2E. The first of these allows the user to produce additional sub-catalogues at higher reliability than the target 80% reliability of the full catalogue. The second contains sources whose reliability cannot be estimated, because they are embedded in a bright and complex (e.g., filamentary) background of emission.

The number of sources in the catalogue ranges from 1560 at 30 GHz up to 48 181 sources at 857 GHz. Both sub-catalogues include polarization measurements, in the form of polarized flux densities and orientation angles (or upper-limits) for all seven polarization-sensitive *Planck* channels. The number of sources with polarization information (other than upper-limits) in the catalogue ranges from 113 at 30 GHz up to 666 at 353 GHz. The improved data processing of the full-mission maps and their reduced instrumental noise levels allow us to increase the number of objects in the catalogue, improving its completeness at the target 80% reliability compared with previous versions, the PCCS (Planck Collaboration XXVIII 2014) and the Early Release Compact Source Catalogue (ERCSC; Planck Collaboration XIII 2011). The improvements are most pronounced for the LFI channels, due to the much larger increase in the data available. The completeness of the 857 GHz channel, however, has not increased, because a more refined reliability assessment resulted in a higher S/N threshold being applied in the selection function of this catalogue. Nevertheless the reliability of the PCCS2 catalogue at 857 GHz is higher than that of the PCCS.

9.2. The Second Planck Catalogue of Clusters

The Second Planck Catalogue of SZ Sources (PSZ2; Planck Collaboration XXVII 2016), based on the full mission data, is the largest SZ-selected sample of galaxy clusters yet produced and the deepest all-sky catalogue of galaxy clusters. It contains 1653 detections, of which 1203 are confirmed clusters with identified counterparts in external data sets, and is the first SZ-selected cluster survey containing $>10^3$ confirmed clusters. A total of 937 sources from the half-mission catalogue (PSZ1) released in 2013 are included, as well as 716 new detections. The completeness, which is provided as a product with the catalogue, is determined using simulated signal injection, validated through comparison to external data, and is shown to be consistent with semi-analytic expectations. The reliability is characterized using high-fidelity simulated observations and a machine-learning-based quality assessment, which together place a robust lower limit of 83% on the reliability. Using simulations, we find that the Y_{5R500} estimates are robust to pressure-profile variations and beam systematics; however, accurate conversion to Y_{500} requires the use of prior information on the cluster extent. Results of a multi-wavelength search for counterparts in ancillary data, which makes use of radio, microwave, infrared, optical, and X-ray data sets, and which places emphasis on the robustness of the counterpart match, are included in the catalogue. We discuss the physical properties of the new sample and identify a population of low-redshift, X-ray, under-luminous clusters revealed by SZ selection. Figure 14 shows the masses and redshifts for the 1093 PSZ2 clusters with known redshifts.

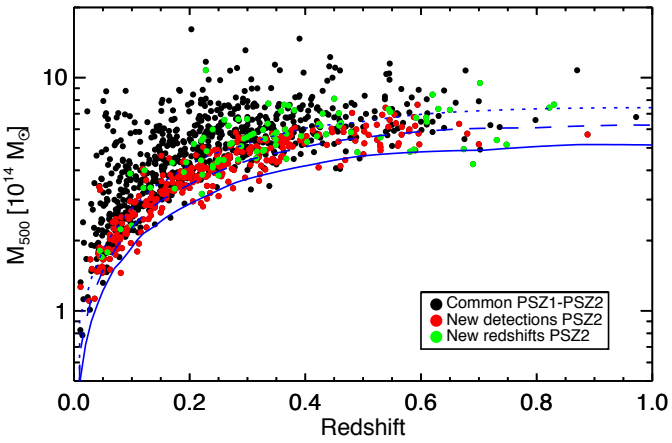

Fig. 14. M_{500}–z plane distribution of the 1093 PSZ2 clusters with known redshift. New PSZ2-detected clusters are indicated by red dots, while commmon PSZ1 and PSZ2 clusters are indicated by black dots. Green dots mark the common PSZ2–PSZ1 detections with updated redshifts in PSZ2. The solid, dashed, and dotted lines indicate the limiting mass at 20%, 50%, and 80% survey completeness, respectively.

9.3. The Planck Catalogue of Galactic Cold Clumps

The *Planck* catalogue of Galactic Cold Clumps (PGCC, Planck Collaboration XXVIII 2016) contains Galactic sources identified as cold using the `CoCoCoDeT` (Montier et al. 2010) multi-frequency point source detection algorithm on the *Planck* 857, 545, and 353 GHz data and the IRIS 3 THz data (Miville-Deschênes & Lagache 2005), at a resolution of 5′. This selects point sources exhibiting submillimetre excess in the 353, 545, and 857 GHz *Planck* bands simultaneously, compared to the average colour of the background, which is typical of sources appearing colder than their environment.

The PGCC catalogue is the full-mission version of the Early Cold Core (ECC) catalogue released in 2011 as part of the ERCSC (Planck Collaboration VII 2011). The ECC catalogue was built from the first 295 days of *Planck* data, and contains 915 sources selected to ensure $T < 14$ K and $S/N > 15$. A statistical description of the ECC and the extended catalogue (including sources at all temperatures and with $S/N > 4$) is given in Planck Collaboration XXII (2011), while a detailed description of a subsample of 10 sources was presented in Planck Collaboration XXIII (2011). The PGCC catalogue, included in the 2015 *Planck* release, is built on the full *Planck* mission data, and contains 13 188 Galactic sources, plus 54 sources located in the Large and Small Magellanic Clouds.

The morphology of each source is obtained using a Gaussian elliptical fit, which is then used to estimate flux densities in all bands through aperture photometry. Depending on the S/N of the flux density estimates, three categories of source are identified: 6993 sources with reliable flux densities in all bands (`FLUX_QUALITY`=1); 3755 sources with flux density estimates in all bands except 3 THz (`FLUX_QUALITY`=2), which are considered very cold candidates; and 2440 sources without reliable flux density estimates (`FLUX_QUALITY`=3), usually due to a complex environment, which are considered poor candidates.

Distance estimates have been obtained for 5574 PGCC sources by combining seven different methods. While PGCC sources are mainly located in the Solar neighbourhood, with 88% of sources with reliable distance estimates lying within 2 kpc of the Sun, distance estimates range from a few hundred parsecs towards local molecular clouds to 10.5 kpc towards the Galactic centre.

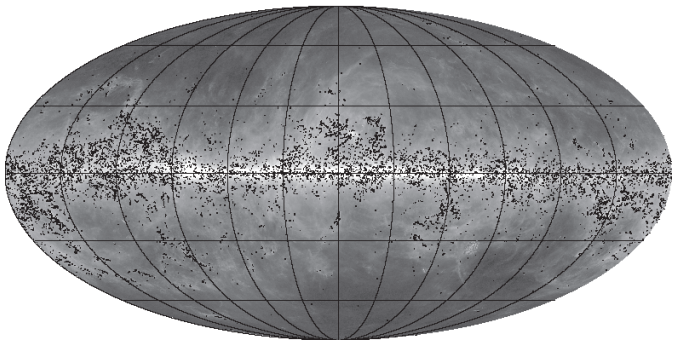

Fig. 15. All-sky distribution of the 13 188 PGCC Galactic cold clumps (black dots) and the 54 cold sources (grey dots) located in the Large and Small Magellanic Clouds. The background map is the 857 GHz *Planck* band, shown in logarithmic scale from 10^{-2} to 10^{2} MJy sr^{-1}.

The temperature of each source is obtained by fitting a modified blackbody to the spectral energy density from 353 GHz to 3 THz, considering the spectral index β as a free parameter when possible. PGCC sources have an average temperature of 13–14.5 K, depending on their flux quality category, and range from 5.8 to 20 K. Other physical parameters have been derived, such as the H_2 column density, the physical size, the mass, the density, and the luminosity. It appears that the PGCC contains a large variety of objects with very different properties, from compact and dense cores to large and massive molecular clouds, located all over the sky. While a large *Herschel* programme (HKP-GCC) already followed up 315 PGCC sources with the PACS and SPIRE instruments, the PGCC catalogue is the first all-sky sample of Galactic cold sources obtained with a homogeneous method, and hence represents a gold mine for investigations of the early phases of star formation in various environments.

9.4. Diffuse Galactic foregrounds from CMB component separation

As in 2013 (Planck Collaboration X 2016), we establish a single parametric model of the microwave sky, accounting simultaneously for all significant diffuse astrophysical components and relevant instrumental effects using the Bayesian `Commander` analysis framework (Eriksen et al. 2004, 2006, 2008). The 2015 analysis is extended in multiple directions. First, instead of 15.5 months of temperature data, we include the full *Planck* mission data – 50 months of LFI and 29 months of HFI data – in both temperature and polarization. Second, we include the 9-year WMAP observations between 23 and 94 GHz (Bennett et al. 2013), and a 408 MHz survey map (Haslam et al. 1982), providing enough frequency constraints to decompose the low-frequency foregrounds into separate synchrotron, free-free, and spinning dust components. Third, we include the *Planck* 545 and 857 GHz frequency bands, allowing us to constrain the thermal dust temperature and emissivity index with greater precision, thereby reducing degeneracies between CMB, CO, and free-free emission. Fourth, we implement a multi-resolution technique to provide component maps at high angular resolution. Specifically, the CMB is recovered with angular resolution 5′ FWHM (Planck Collaboration IX 2016), thermal dust emission and CO $J = 2 \rightarrow 1$ lines are recovered at 7.′5 FWHM, and synchrotron, free-free, and spinning dust are recovered at 1° FWHM. Fifth, we use individual detector and detector-set maps as inputs, instead of fully-combined frequency maps. The increase in the number of input maps allows many null tests that are used to

reject individual maps exhibiting significant levels of systematic effects. Sixth, we fit for two important instrumental effects: relative calibration between detectors; and bandpass uncertainties.

The combination of these improvements allows us to reconstruct a total of six primary emission mechanisms in temperature, namely CMB, synchrotron, free-free, spinning dust, CO, and thermal dust emission, in addition to two secondary components, namely thermal SZ emission around the Coma and Virgo regions, and molecular line emission between 90 and 100 GHz. For polarization, we reconstruct three primary emission mechanisms: CMB; synchrotron; and thermal dust. All of these components are delivered as part of the 2015 *Planck* release.

Figures 16 and 17 (from Planck Collaboration X 2016) show the diffuse, high-latitude, Galactic foreground components determined from component separation in temperature and polarization. Figure 18 shows the frequency spectra of fluctuations of diffuse foreground components in temperature and polarization, compared to that of the CMB. The sky model presented in this paper provides an impressive fit to the current data, with temperature residuals at the few microkelvin level at high latitudes across the CMB-dominated frequencies, and with median fractional errors below 1% in the Galactic plane across the *Planck* frequencies. For polarization, the residuals are statistically consistent with instrumental noise at high latitudes, but limited by significant temperature-to-polarization leakage in the Galactic plane. Overall, this model represents the most accurate and complete description currently available of the astrophysical sky between 20 and 857 GHz.

9.5. Carbon monoxide emission

Carbon monoxide emission lines are present in all HFI frequency bands except 143 GHz. Using component-separation techniques, the three lowest rotational transitions can be extracted from *Planck* data, providing full-sky maps of the CO $J = 1 \rightarrow 0$, $J = 2 \rightarrow 1$, and $J = 3 \rightarrow 2$ transitions (Planck Collaboration XIII 2014). For the 2015 release, data from the full mission and better control of systematic errors lead to better maps. Table 8 summarizes the products. Figure 16 shows the `Commander` maps of all three transitions.

TYPE 1 maps are produced by a single-channel analysis, where individual bolometer maps are linearly combined to produce maps of the CO(1→0), CO(2→1), and CO(3→2) emission lines at the native resolution of the *Planck* maps. Although noisier than the other approaches, using information from a single channel strongly limits contamination from other Galactic components, such as dust or free-free emission. This makes TYPE 1 maps suitable for studying emission in the Galactic disk and CO-rich regions, but not for the high-Galactic latitudes where the CO emission is below the noise level.

TYPE 2 maps of CO(1→0) and CO(2→1) are produced using multi-channel information (i.e., using linear combinations of *Planck* channel maps smoothed to 15′). Using frequency maps, these types of product have a higher signal-to-noise ratio, allowing for their use in fainter high-Galactic latitude regions. They are, however, more susceptible to dust contamination, especially for CO(2→1), which makes them less suitable in the Galactic plane than TYPE 1 maps.

A high-resolution TYPE 3 map, as defined in Planck Collaboration XIII (2014), is not being delivered in the 2015 data release. Alternatively, another set of CO maps has been produced as part of the full `Commander` baseline multi-component model, which is described in Planck Collaboration X (2016).

TYPE 1 and TYPE 2 maps are released with associated standard deviation maps, error maps, and masks. The suite of tests detailed in Planck Collaboration XIII (2014) has been repeated on the new TYPE 1 and TYPE 2 maps, which have been found to perform as well as their 2013 counterparts, even though small variations ($\lesssim$ 2–5 K km s^{-1}) exist in the Galactic plane.

9.5.1. All-sky Sunyaev-Zeldovich emission

The 30 to 857 GHz frequency channel maps from the *Planck* satellite survey were used to construct an all-sky map of the thermal SZ effect Planck Collaboration XXII (2016). As discussed in Planck Collaboration XXI (2014), we apply to those maps specifically tailored component-separation algorithms, `MILCA` Hurier et al. (2013) and `NILC` Remazeilles et al. (2011), that allow us to separate the thermal SZ emission from both the foreground contamination and the CMB. An orthographic view of this Compton y-map is shown in Fig. 19. This map has been characterized in terms of noise properties and residual foreground contamination, mainly thermal dust emission at large angular scales, and CIB and extragalactic point sources at small angular scales. Blindly-detected clusters in this map are consistent with those from the PSZ2 catalogue (Planck Collaboration XXVII 2016), both in terms of cluster number and integrated flux. Furthermore, by stacking individually undetected groups and clusters of galaxies we find that the y-map is consistent with thermal SZ emission even for low S/N regions. Using foreground models derived in Planck Collaboration XXIII (2016), we are able to measure the thermal SZ angular power spectrum over 50% of the sky. We conclude that the y-map is dominated by thermal SZ signal in the multipole range $20 < \ell < 800$. Similar results are obtained from a high-order-statistic analysis. The reconstructed y-map is delivered as part of the *Planck* 2015 release. We also deliver a foreground mask (which removes known point sources and regions with strong contamination from Galactic emission), a noise variance map, the estimated power spectrum, and the weights for the `NILC` algorithm.

10. *Planck* 2015 cosmology results

Since their discovery, anisotropies in the CMB have contributed significantly to defining our cosmological model and measuring its key parameters. The standard model of cosmology is based upon a spatially flat, expanding Universe whose dynamics are governed by General Relativity and dominated by cold dark matter and a cosmological constant (Λ). The seeds of structure have Gaussian statistics and form an almost scale-invariant spectrum of adiabatic fluctuations. The 2015 *Planck* data remain in excellent agreement with this paradigm, and continue to tighten the constraints on deviations and reduce the uncertainties on the key cosmological parameters.

The major methodological changes in the steps going from sky maps to cosmological parameters are discussed in Planck Collaboration XI (2016) and Planck Collaboration XIII (2016). These include the use of *Planck* polarization data instead of WMAP, changes to the foreground masks to include more sky and dramatically reduce the number of point source "holes", minor changes to the foreground models, improvements to the data processing, and use of cross-half-mission likelihoods (Planck Collaboration XI 2016; Planck Collaboration XIII 2016). We find good agreement with our earlier results, with increased precision.

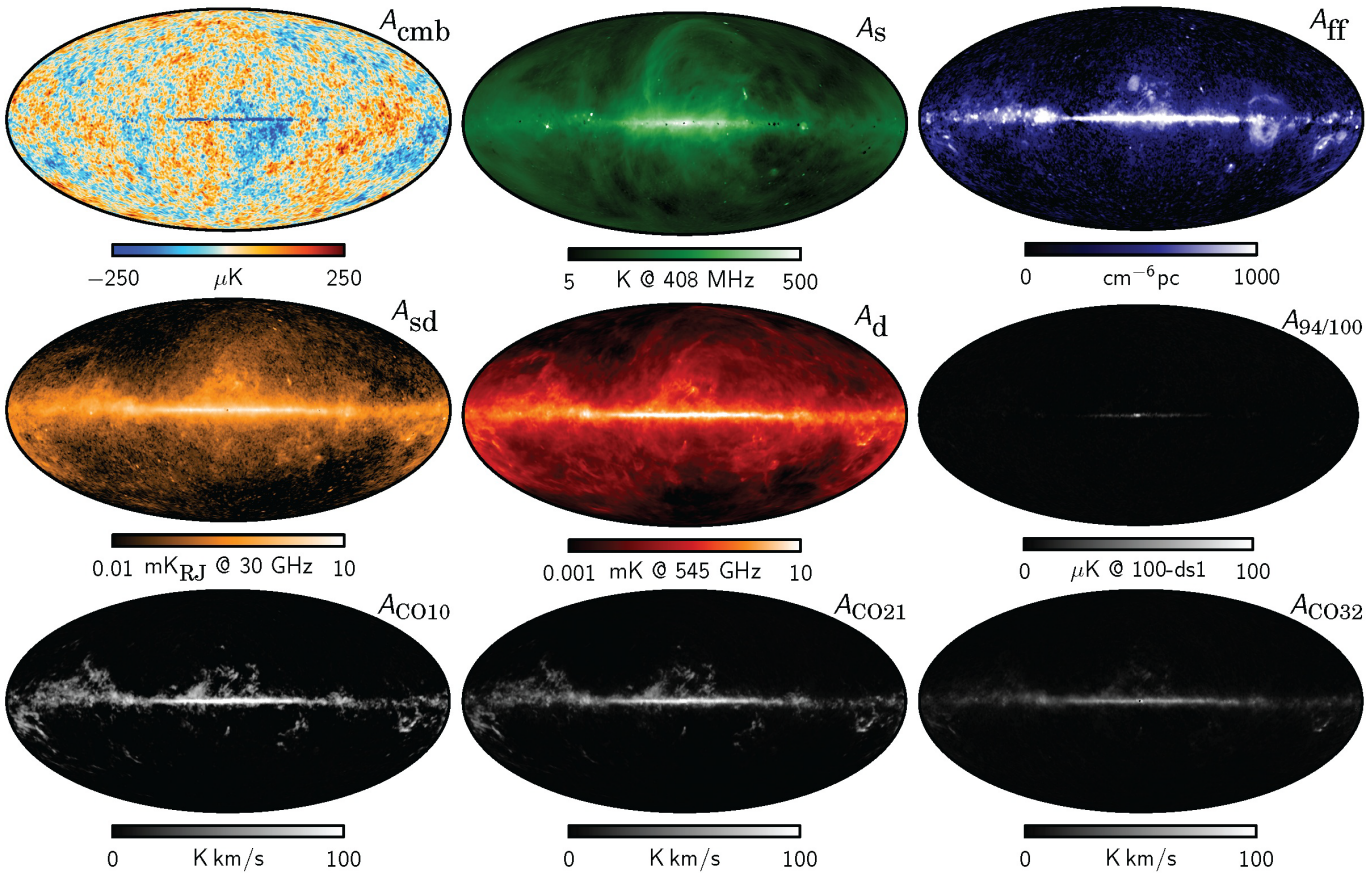

Fig. 16. Maximum posterior intensity maps derived from the joint analysis of *Planck*, WMAP, and 408 MHz observations (Planck Collaboration X 2016). *From left to right and top to bottom*: CMB; synchrotron; free-free; spinning dust; thermal dust; line emission around 90 GHz; CO $J = 1 \rightarrow 0$; CO $J = 2 \rightarrow 1$; and CO $J = 3 \rightarrow 2$.

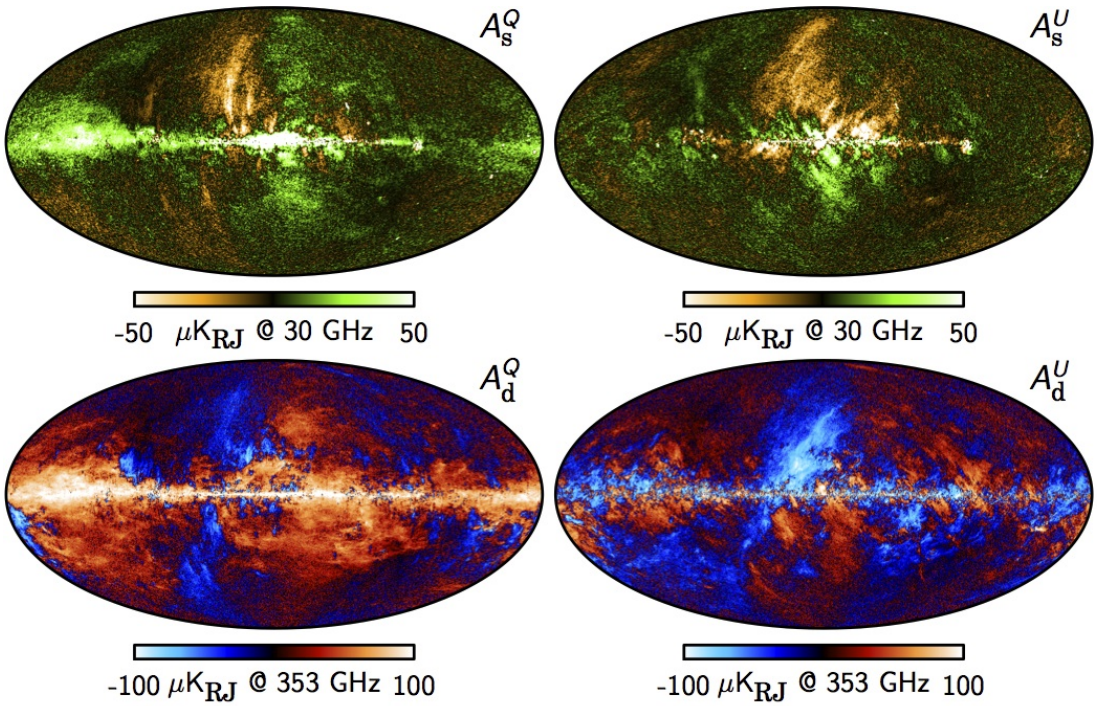

Fig. 17. Maximum posterior foreground polarization maps derived from the *Planck* observations between 30 and 353 GHz (Planck Collaboration X 2016). The *left and right columns* show Stokes Q and U parameters, respectively. *Top*: synchrotron polarization at 30 GHz. *Bottom*: thermal dust polarization at 353 GHz.

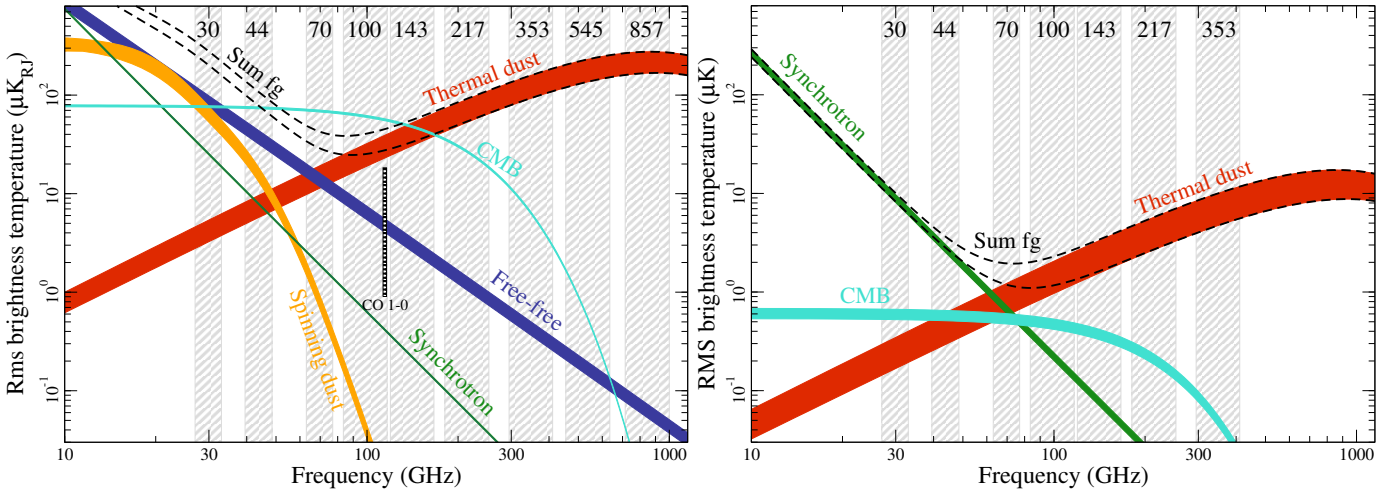

Fig. 18. Brightness temperature rms of the high-latitude sky as a function of frequency and astrophysical component for temperature (*left*) and polarization (*right*). For temperature, each component is smoothed to an angular resolution of 1° FWHM, and the lower and upper edges of each line are defined by masks covering 81 and 93% of the sky, respectively. For polarization, the corresponding smoothing scale is 40′, and the sky fractions are 73 and 93%.

Table 8. Summary of main CO product characteristics.

				Noise rms [K_{RJ} km s^{-1}]		Analysis details	
Map	Algorithm	CO line	Resolution [arcmin]	15′ FWHM	60′ FWHM	Frequencies [GHz]	Model
TYPE 1	MILCA	$J=1\rightarrow0$	9.6	1.4	0.34	100 (bol maps)[a]	CO, CMB
	MILCA	$J=2\rightarrow1$	5.0	0.53	0.16	217 (bol maps)[a]	CO, CMB, dust
	MILCA	$J=3\rightarrow2$	4.8	0.55	0.18	353 (bol maps)[a]	CO, dust
TYPE 2	MILCA	$J=1\rightarrow0$	15	0.39	0.085	70, 100, 143, 353	CO, CMB, dust, free-free
	MILCA	$J=2\rightarrow1$	15	0.11	0.042	70, 143, 217, 353	CO, CMB, dust, free-free
	Commander	$J=1\rightarrow0$	60	···	0.084	0.408–857	Full
	Commander	$J=2\rightarrow1$	60	···	0.037	0.408–857	Full
	Commander	$J=3\rightarrow2$	60	···	0.060	0.408–857	Full
TYPE 3	Commander	$J=2\rightarrow1$[b]	7.5	0.090	0.031	143–857	CO, CMB, dust
	Commander-Ruler	$J=1\rightarrow0$[c,d]	5.5	0.19	0.082	30–353	CO, CMB, dust, low-freq

Notes. [(a)] Built from single-bolometer maps within a given frequency (see Planck Collaboration X 2016). [(b)] Formally a weighted average of CO $J=2\rightarrow1$ and $J=3\rightarrow2$, but strongly dominated by CO $J=2\rightarrow1$. [(c)] Formally a weighted average of CO $J=1\rightarrow0$, $J=2\rightarrow1$ and $J=3\rightarrow2$, but strongly dominated by CO $J=1\rightarrow0$. [(d)] Only published in 2013.

10.1. Cosmological parameters

Planck's measurements of the cosmological parameters derived from the full mission are presented and discussed in Planck Collaboration XIII (2016). As in our previous release, the data are in excellent agreement with the predictions of the 6-parameter ΛCDM model (see Table 9), with parameters tightly constrained by the angular power spectrum. The best-fit model parameters from the full mission are typically within a small fraction of a standard deviation of their values from Planck Collaboration XVI (2014), with no outliers. The constraints on the parameters of the base ΛCDM model have improved by up to a factor of 3. The largest shifts are in the scalar spectral index, n_s, which has increased by 0.7σ, and the baryon density, $\omega_b \equiv \Omega_b h^2$, which has increased by 0.6σ. Both of these shifts are partly due to correction of a systematic error that contributed to a loss of power near $\ell = 1800$ in the 2013 results (Planck Collaboration XIII 2016). This systematic also biased the inferences on H_0 slightly low (by less than 0.5σ). In addition, the overall amplitude of the observed spectrum has shifted upwards by about 2% (in power) due to the calibration changes described in Sect. 5.4, and the optical depth to Thomson scattering, τ, has shifted down by nearly 1σ. These shifts approximately cancel in the derived normalization of the matter power spectrum. The remaining shifts are consistent with the known changes in noise level, time-stream filtering, absolute calibration, beams, and other aspects of the data processing.

Both the angular size of the sound horizon, θ_*, and the cold dark matter density, ω_c, have become significantly better determined. The data at high ℓ are now so precise, and the polarization data so constraining, that we not only see very strong evidence for three species of light neutrinos, but can measure the effective viscosity of the neutrino "fluid" to be non-zero at the 9σ level. The constraint on the baryon density, ω_b, is now comparable with the best quoted errors from big bang nucleosynthesis and suggests the possibility of calibrating nuclear capture

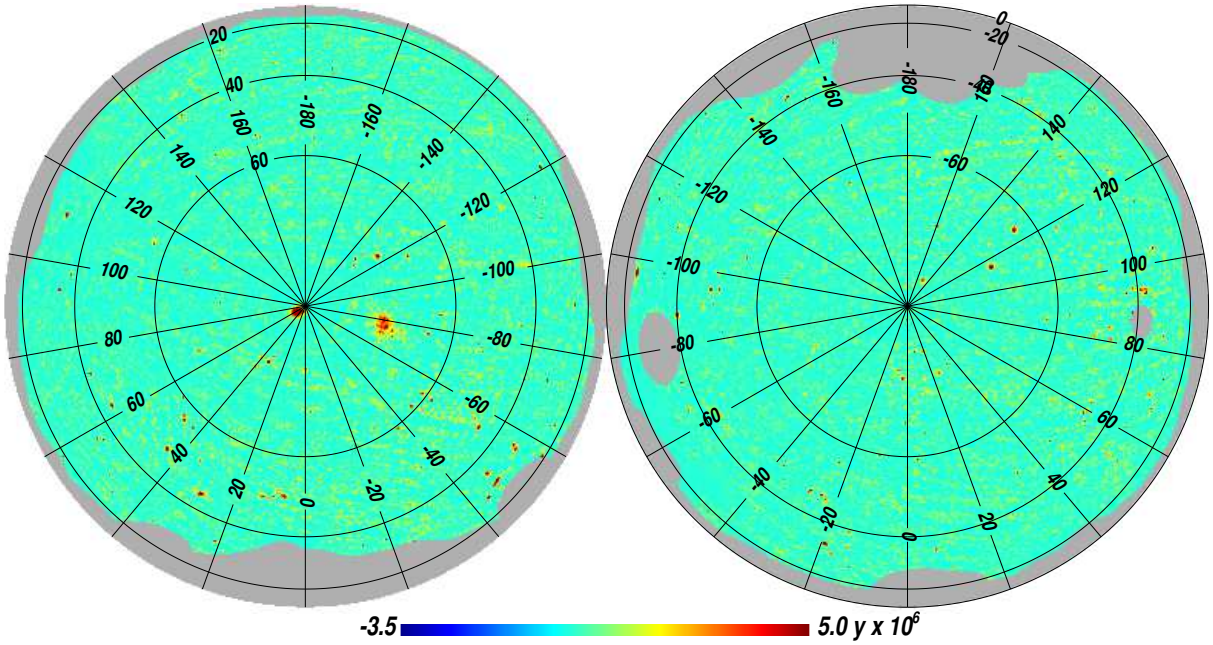

Fig. 19. Orthographic projection of the reconstructed *Planck* all-sky y-map in Compton parameter units (Planck Collaboration XXII 2016). For illustration purposes and to enhance the thermal SZ signal-to-noise ratio, the y-map has been Wiener filtered. Positive sources in the map correspond to clusters and super-clusters of galaxies with strong thermal SZ emission. In particular, the Coma and Virgo clusters are clearly visible near the north Galactic pole. The region of strongest contamination from Galactic foreground emission in the Galactic plane has been partially masked.

Table 9. Parameter best-fit values and 68% confidence levels for the base ΛCDM cosmology, computed from the *Planck* CMB power spectra, in combination with the CMB lensing likelihood ("lensing") and a compilation of external data sets ("ext").

Parameter	PlanckTT+lowP+lensing	PlanckTT, TE, EE+ lowP+lensing+ext
$\Omega_b h^2$ . . .	0.02226 ± 0.00023	0.02230 ± 0.00014
$\Omega_c h^2$ . . .	0.1186 ± 0.0020	0.1188 ± 0.0010
$100\theta_{MC}$.	1.04103 ± 0.00046	1.04093 ± 0.00030
τ	0.066 ± 0.016	0.066 ± 0.012
$\ln(10^{10}A_s)$	3.062 ± 0.029	3.064 ± 0.023
n_s	0.9677 ± 0.0060	0.9667 ± 0.0040
H_0	67.8 ± 0.9	67.74 ± 0.46
Ω_Λ	0.692 ± 0.012	0.6911 ± 0.0062
Ω_b	0.0484 ± 0.0010	0.04860 ± 0.00051
Ω_c	0.258 ± 0.011	0.2589 ± 0.0057
Ω_m	0.308 ± 0.012	0.3089 ± 0.0062
$\Omega_m h^2$ . . .	0.1415 ± 0.0019	0.14170 ± 0.00097
$\Omega_m h^3$ . . .	0.09591 ± 0.00045	0.09598 ± 0.00029
σ_8	0.815 ± 0.009	0.8159 ± 0.0086
$\sigma_8\Omega_m^{0.5}$ . .	0.4521 ± 0.0088	0.4535 ± 0.0059
Age[Gyr]	13.799 ± 0.038	13.799 ± 0.021
r_{drag}	147.60 ± 0.43	147.50 ± 0.24
k_{eq}	0.01027 ± 0.00014	0.010288 ± 0.000071

Notes. While we see no evidence that systematics in the high-ℓ polarization are biasing parameters in the base ΛCDM model, a conservative choice would be to take the parameters listed in Col. 2.

cross-sections from CMB observations. The addition of polarization data has improved by an order of magnitude our upper limit on the annihilation rate of dark matter.

Despite trying a wide range of extensions to the basic, 6-parameter ΛCDM model, we find no significant evidence for a failure of the model. Within each extension of the parameter space, the default parameter values for the ΛCDM model remain a good fit to the data. This continues to hold when we combine the *Planck* data with other measurements, such as the distance scale measured by baryon acoustic oscillations (BAO) in galaxy surveys or Type Ia supernovae, or the growth of structure determined by redshift-space distortions. Since our best-fit cosmology has shifted by very little since our 2013 release, we continue to see tensions with some analyses of other astrophysical data sets (e.g., the abundance of clusters of galaxies, weak gravitational lensing of galaxies or cosmic shear, and distances measured by BAO in the Lyα forest at high z). Planck Collaboration XIII (2016) shows that these tensions cannot be resolved with standard single parameter extensions of the base ΛCDM model. Resolving these discrepancies remains an area of active research.

10.2. Constraints from large angular scales

The anisotropy at large angular scales, particularly the polarization, allows us to place tight constraints on the optical depth to Thomson scattering, τ, and the tensor-to-scalar ratio, r. The *Planck* temperature data, in combination with CMB lensing and low-ℓ polarization measured at 70 GHz, prefer a lower optical depth, $\tau = 0.066 \pm 0.016$, than the earlier inference from WMAP9 ($\tau \approx 0.09$, which was used in our 2013 analysis), which implies a lower redshift of reionization ($z_{re} = 8.8^{+1.7}_{-1.4}$). However, when cleaned of foregrounds using our 353 GHz channel, the WMAP polarization data are in good agreement with a lower optical depth. With the dramatic improvement in our CMB lensing detection, we are able to independently constrain τ, finding comparably tight and consistent results ($\tau = 0.071 \pm 0.016$) without the use of low-ℓ polarization. This provides additional confidence in the results.

While improved constraints on polarization at low multipoles will eventually allow us to study the reionization epoch in more detail, at present the largest impact of the change in τ comes from the implied downward shift in the inferred matter power spectrum normalization, σ_8. As it happens, much of the downward shift in this parameter is largely cancelled by the upward shift in the CMB spectrum arising from the improved calibration in the current data release.

Gravitational waves entering the horizon between recombination and today give a "tensor" contribution to the large-scale temperature and polarization anisotropies. Our strongest *Planck*-only constraint still comes from temperature anisotropies at $\ell < 10^2$ (or $k \lesssim 0.01$ Mpc^{-1}), and is thus limited by cosmic variance and is model-dependent. Tensor modes also generate a B-mode signal, which peaks at $\ell \approx 10^2$, slightly smaller scales than the bulk of the temperature signal. The cosmological landscape became more complicated in early 2014 with the detection of B-mode polarization anisotropy by the BICEP2 team (BICEP2 Collaboration 2014). Analysis of *Planck* polarization data at high Galactic latitudes demonstrated that no region of the sky can be considered dust-free when searching for primordial B-modes (Planck Collaboration Int. XXX 2016), and a joint analysis of BICEP2/Keck Array observations and *Planck* polarization data (BICEP2/Keck Array and Planck Collaborations 2015) shows that polarized dust emission contributes a significant part of the BICEP2 signal. Combining the *Planck* and revised BICEP2/Keck Array likelihoods leads to a 95% upper limit of $r_{0.002} < 0.09$. This eliminates any tension between the BICEP2 and *Planck* results, and in combination with our other constraints disfavours inflationary models with a ϕ^2 potential. This and other implications for inflationary models in the early Universe are discussed more fully in Planck Collaboration XIII (2016) and Planck Collaboration XX (2016).

10.3. Dark energy and modified gravity

Even though much of the weight in the *Planck* data lies at high redshift, *Planck* can still provide tight constraints on dark energy and modified gravity models, especially when used in combination with other probes. This is explored in Planck Collaboration XIV (2016), which focuses on tests of dark energy and modified gravity on the scales where linear theory is most applicable, since these are the most theoretically robust. As for Planck Collaboration XIII (2016), the results are consistent with the simplest scenario, ΛCDM, though all constraints on dark energy models (including minimally-coupled scalar field models or evolving equation of state models) and modified gravity models (including effective field theory, phenomenological, $f(R)$, and coupled dark energy models) are considerably improved with respect to past analyses. In particular, we improve significantly the constraint on the density of dark energy at early times, finding that it has to be below 2% (95% confidence) of the critical density, even if it only plays a role at $z < 50$. Constraints are tighter if early dark energy is present since recombination, with $\Omega_e < 0.0071$ (for the data combination PlanckTT+lensing+BAO+SNe+H_0), and an even tighter bound results if high-ℓ polarization is included. In models where perturbations are modified, even if the background is ΛCDM, a few tensions appear, mainly driven by external data sets.

10.4. Lensing of the CMB

The CMB fluctuations measured by *Planck* provide a slightly perturbed image of the last-scattering surface, due to the effects of gravitational lensing by large-scale structure. Lensing slightly washes out the acoustic peaks of the CMB power spectrum, an effect we see in the *Planck* data at high significance. Lensing also introduces distinctive non-Gaussian features into the CMB maps, which allow us to map and make statistical measurements of the gravitational potentials, and the associated matter. These are studied in detail in Planck Collaboration XV (2016). The lensing signal is consistent with the basic, 6-parameter, ΛCDM model that best fits the temperature data. This gives us a very strong consistency check on the gravitational instability paradigm and the growth of structure over more than two decades in expansion factor.

Since it provides sensitivity to the growth of structure between the surface of last scattering and the present epoch, the lensing signal allows us to measure a number of important parameters by breaking parameter degeneracies. Figure 20 shows the lensing power spectrum, which for the first time is measured with higher accuracy than it is predicted by the base ΛCDM model that fits the temperature data. With the temperature-only nominal mission data from the 2013 *Planck* data release, we were able to make the most powerful measurement of lensing to that date (at a level of 25σ). In the current release, incorporating additional temperature data, as well as entirely new polarization information, we have nearly doubled the power of this measurement to 40σ. This is the most significant detection to date, allowing lensing to be used as part of our precision cosmology suite.

10.5. Inflation

The release of the 2013 *Planck* data and findings had an enormous impact on the inflationary community, and the *Planck* 2015 results continue to demonstrate the importance of this window into the early Universe. Planck Collaboration XX (2016) presents our constraints on inflationary models. The *Planck* data are consistent with a purely adiabatic, power-law spectrum of initial fluctuations, whose spectral index ($n_s = 0.9677 \pm 0.006$) is significantly different from unity. The addition of polarization data has significantly improved the limits on any isocurvature modes, which are now constrained at the percent level. Despite a detailed search, and study of several models, we see no statistically significant evidence for departures from a power law. The combination of *Planck* data with the BICEP2/Keck Array data provide a strong upper limit on the tensor-to-scalar ratio, and disfavour all monomial models ($V(\phi) \propto \phi^{2p}$) with $p \geq 1$. This is an important milestone, since these form the simplest class of inflationary models.

10.6. Primordial non-Gaussianity

Planck Collaboration XVII (2016) for the first time uses polarization information to constrain non-Gaussian signals left by primordial physics. The results significantly reduce the allowed model space spanned by local, equilateral, and orthogonal non-Gaussianity, tightening constraints by up to 45%. In particular, $f_{NL}^{local} = 0.8 \pm 5.0$, $f_{NL}^{equil} = -4 \pm 43$, and $f_{NL}^{ortho} = -26 \pm 21$. In addition, the *Planck* 2015 analysis covers a greatly extended range of primordial 3-point and 4-point signals, constraining inflationary model space as well as some proposed alternatives to inflation. The global picture that emerges is one of consistency

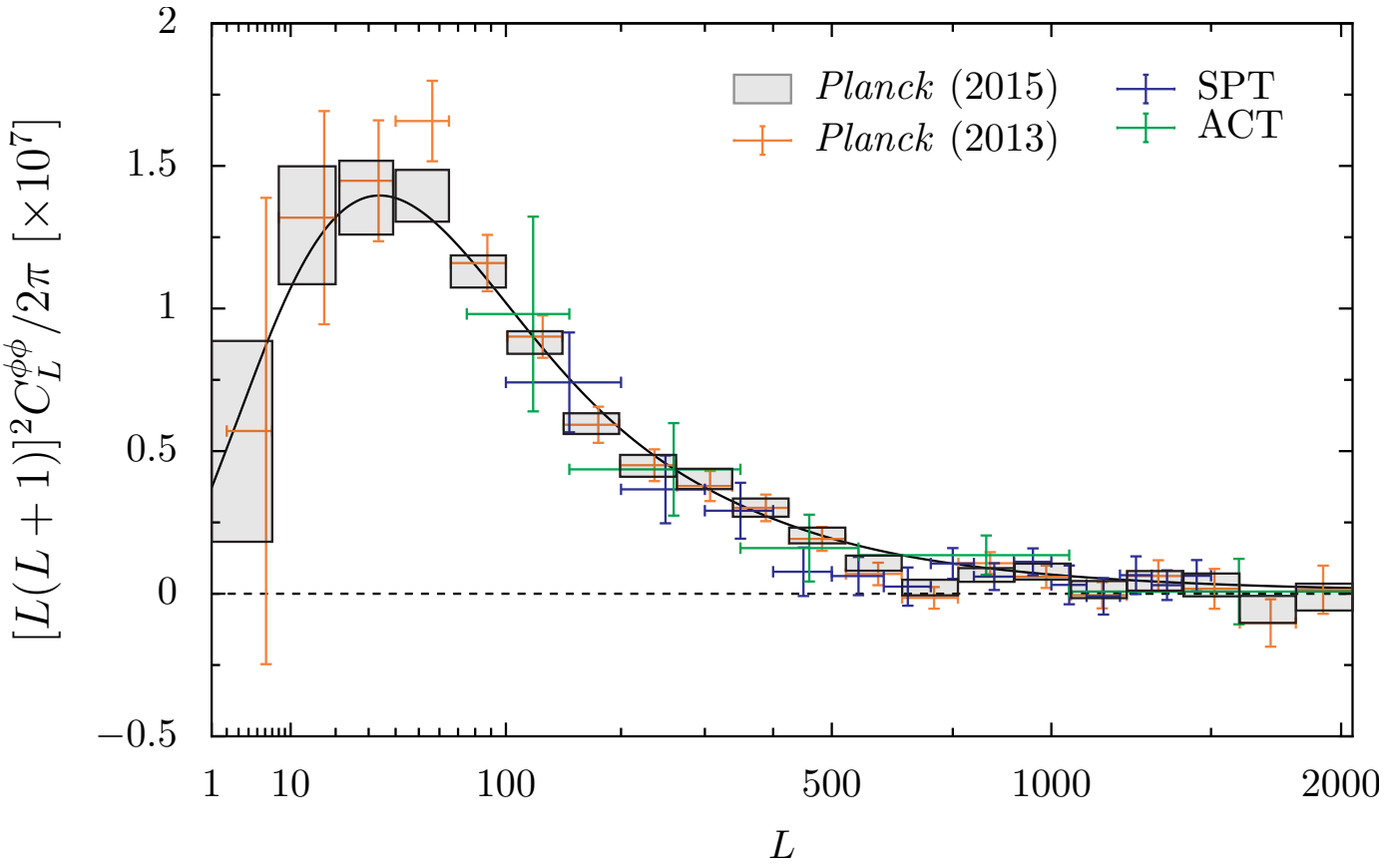

Fig. 20. Lensing potential power spectrum estimate from the 2015 data release (Planck Collaboration XV 2016), based on the SMICA CMB map, as well as previous reconstructions from *Planck* and other experiments for comparison.

with the premises of ΛCDM cosmology, namely that the structure we observe today is the consequence of the passive evolution of adiabatic, Gaussian, nearly scale-invariant, primordial seed perturbations.

10.7. Isotropy and statistics

The *Planck* 2013 results determined the presence of statistically anisotropic signals in the CMB, confirming previous studies made using WMAP data. Such anomalies therefore constitute real features of the microwave sky, and potentially challenge fundamental assumptions of the standard cosmological model. Planck Collaboration XVI (2016) extends these studies based mainly on the full *Planck* mission for temperature, but also including some polarization measurements. A large number of statistical tests indicate consistency with Gaussianity, while a power deficit at large angular scales is manifested in several ways, for example in low map variance. The well-known "Cold Spot" is identified through various methods. Tests of directionality suggest the presence of angular clustering from large to small scales, but at a significance that is dependent on the details of the approach. On large angular scales, a dipolar power asymmetry is investigated through several approaches, and we address the subject of a posteriori correction. Our ability to include results based on polarization data is limited by two factors. First, CMB polarization maps have been high-pass filtered to mitigate residual large-scale systematic errors in the HFI channels, thus eliminating structure in the maps on angular scales larger than about 10°. Second, an observed noise mismatch between the simulations and the data precludes robust conclusions based on the null-hypothesis approach adopted throughout the paper. Nevertheless, we perform the first examination of polarization data via a stacking analysis, in which the stacking of the data themselves necessarily acts to lower the effect of the noise mismatch. We find that the morphology of the stacked peaks is consistent with the expectations of statistically isotropic simulations. Further studies of the large angular scale structure of the CMB polarization anisotropy will be conducted with data of improved quality expected to be released in 2016.

10.8. The ISW effect

The 2013 results on the integrated Sachs-Wolfe (ISW, Planck Collaboration XIX 2014) effect have been refined and extended using the full mission data (Planck Collaboration XXI 2016). We now detect the ISW effect at 4σ by cross-correlating the *Planck* CMB temperature map with tracers of the large-scale structure, in particular: the NRAO VLA Sky Survey (NVSS) radio catalogue; the photometric luminous galaxy catalogue from the Baryonic Oscillation Spectroscopic Survey of the Sloan Digital Sky Survey (SDSS) III; the photometrically-selected galaxies from the SDSS-DR8 catalogue; the Wide-field Infrared Survey Explorer (WISE) galaxy and AGN catalogues; and the *Planck* lensing map. The ISW-lensing bispectrum (Planck Collaboration XIX 2014; Planck Collaboration XXII 2014; Planck Collaboration XXVI 2014) gives a detection at approximately 3σ, 20% higher than the level achieved with the 2013 release. The increase is due to the lower noise in the full mission temperature data, and to the

addition of polarization data, which enter into the ISW detection levels mentioned above through the *Planck* lensing map.

Since a purely gravitational effect does not polarize photons, polarization data in principle provide a powerful discriminant between ISW and primary CMB fluctuations. The current *Planck* polarization maps, however, are not usable at the largest scales (Sect. 2.2), so this tool cannot yet be fully exploited.

Polarization data on smaller scales ($\gtrsim 5^\circ$) can be used to probe the ISW effect through stacking of CMB anisotropies at the positions of known superstructures. We have studied the photometric profiles of *Planck* CMB polarization patches at the locations of the Granett et al. (2008) catalogue of superclusters and super-voids, which have been reported as anomalous ISW sources (e.g., Planck Collaboration XVII 2014). Our analysis, using specially-constructed CMB temperature maps that are correlated and uncorrelated with E-modes, cannot rule out the ISW effect as the cause of these anomalies.

A map of the ISW anisotropies is presented in Fig. 21. It shows the redshifts and blueshifts suffered by CMB photons travelling through the gravitational potential traced by different galaxy catalogues and the *Planck* lensing map. Our reconstruction has a mean error of ≈ 15 μK (per roughly 1° pixel).

10.9. Cosmology from clusters

In 2013 we found an apparent tension between our primary CMB constraints and those from the *Planck* cluster counts, with the clusters preferring a lower normalization of the matter power spectrum, σ_8. The comparison is interesting because the cluster counts directly measure σ_8 at low redshift and hence any tension could signal the need for extensions of the base model, such as non-minimal neutrino mass. However, limited knowledge of the normalization of the scaling relation between SZ signal and mass (usually called "mass bias") continues to hamper the interpretation of this result.

Our 2015 cluster analysis benefits from a larger catalogue (438 objects versus the 189 in 2013), greater control of the selection function, and recent gravitational lensing determinations of the mass bias for *Planck* clusters. With the larger sample, we now fit the counts in the 2-dimensional plane of redshift and S/N, allowing us to simultaneously constrain the slope of the scaling relation and the cosmological parameters. We examine three new empirical determinations of the mass bias from gravitational lensing: weighing the Giants (WtG; von der Linden et al. 2014); the Canadian Cluster Comparison Project (CCCP; Hoekstra et al., priv. comm.); and results from a new method based on CMB lensing (Melin & Bartlett 2015). We use these three results as priors because they measure the mass scale directly on samples of *Planck* clusters.

The cluster constraints on σ_8 and Ω_m are statistically identical to those of 2013 when adopting the same scaling relation and mass bias; in this sense, we confirm the 2013 results with the larger 2015 catalogue. Applying the three new mass bias priors, we find that the WtG calibration reduces the tension with the primary CMB constraints to slightly more than 1σ in the base model, and CCCP results in tension at just over 2σ, similar to the case for the CMB lensing calibration. More detailed discussion of constraints from *Planck* cluster counts can be found in Planck Collaboration XXIV (2016).

11. *Planck* 2015 astrophysics results

11.1. Low frequency foregrounds

Galactic foreground emission between 20 and 100 GHz, based primarily on the `Commander` component separation of Planck Collaboration X (2016), is discussed in Planck Collaboration XXV (2016). The total intensity in this part of the spectrum is dominated by free-free and spinning dust emission, while polarization is dominated by synchrotron emission.

Comparison with radio recombination line templates verifies the recovery of the free-free emission along the Galactic plane. Comparison of high-latitude Hα emission with our free-free map shows residuals that correlate with dust optical depth, consistent with a fraction (around 30%) of Hα having been scattered by high-latitude dust. A number of diffuse morphological features of spinning dust at high latitude can be highlighted. There is substantial spatial variation in the spinning dust spectrum, with the emission peak (in I_ν) ranging from below 20 GHz to more than 50 GHz. There is a strong tendency for the spinning dust component near prominent H II regions to have a higher peak frequency, suggesting that this increase in peak frequency is associated with dust in the photo-dissociation regions around the nebulae. The emissivity of spinning dust in these diffuse regions is of the same order as previous detections in the literature. Over the entire sky, the `Commander` solution finds more anomalous microwave emission (AME) than the WMAP component maps, at the expense of synchrotron and free-free emission. Although the `Commander` model fits the data exceptionally well, as noted in Sect 9.4, the discrepancy is largely driven by differences in the assumed synchrotron spectrum and the more elaborate model of spinning dust designed to allow for the variation in peak frequency noted above. Future surveys, particularly at 5–20 GHz, will greatly improve the separation, since the predicted brightness between the two models disagrees substantially in that range.

In polarization, synchrotron emission completely dominates on angular scales larger than 1° and frequencies up to 44 GHz. We combine *Planck* and WMAP data to make the highest signal-to-noise ratio map yet of the intensity of the all-sky polarized synchrotron emission at frequencies above a few gigahertz, where Faraday rotation and depolarization are negligible (Figs. 22 and 23). Most of the high-latitude polarized emission is associated with distinct large-scale loops and spurs, and we rediscuss their structure following the earlier study of Vidal et al. (2015) based on WMAP observations. We argue that nearly all the emission at $-90^\circ < l < 40^\circ$ is part of the Loop I structure, and show that the emission extends much further into the southern Galactic hemisphere than previously recognized, giving Loop I an ovoid rather than circular outline. However, it does not continue as far as the "*Fermi* bubble/microwave haze", which probably rules out an association between the two structures. The South Polar Spur (SPS, see Fig. 22) is bordered by a polarized dust filament and associated low-velocity H I emission, analogous to the cold features long known to border Loop I around the North Polar Spur. We find two structures that could correspond to distant analogues of the radio loops, as predicted by Mertsch & Sarkar (2013), including one surrounding the Cygnus X star-forming region, both of which are again associated with dust polarization.

We identify a number of other faint features in the polarized sky, including a dearth of polarized synchrotron emission directly correlated with a narrow, 20°-long filament seen in Hα at high Galactic latitude, and also visible in the Faraday rotation map of Oppermann et al. (2012). Finally, we look for evidence of

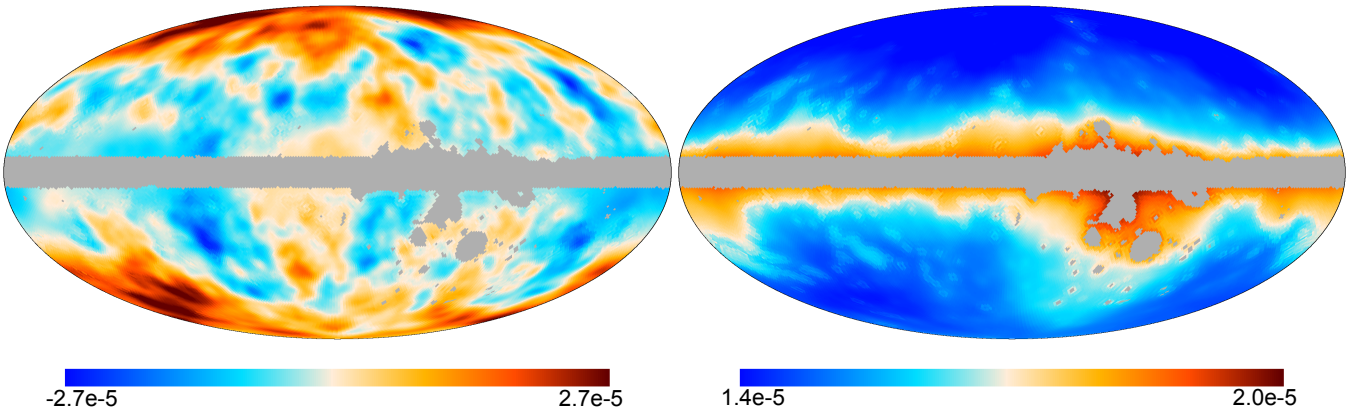

Fig. 21. Maps of ISW anisotropies (*left*) and their (per pixel) uncertainties (*right*), from the combination of the *Planck* SEVEM CMB map and the large-scale structure tracers used in Planck Collaboration XXI (2016): NVSS; WISE galaxies and AGN; and luminous photometrically-selected galaxies from SDSS. The units are kelvins.

polarized AME. Many AME regions, however, are significantly contaminated by polarized synchrotron emission, and we find a 2σ upper limit of 1.6% in the Perseus region.

11.2. Polarized thermal dust emission

Planck has produced the first all-sky map of the polarized emission from dust at submillimetre wavelengths (Figs. 17 and 24). Compared with earlier ground-based and balloon-borne observations (e.g., Benoît et al. 2004; Ward-Thompson et al. 2009; Matthews et al. 2009, 2014; Koch et al. 2010) this survey is an immense step forward in sensitivity, coverage, and statistics. It provides new insight into the structure of the Galactic magnetic field and the properties of dust, as well as the first statistical characterization of one of the main foregrounds to CMB polarization. The wealth of information encoded in the all-sky maps of polarized intensity, P, polarization fraction, p, and polarization angle, ψ, presented in Planck Collaboration X (2016), is illustrated in Fig. 25. Here we summarize the main results from the data analysis by the Planck Consortium. The release of the data to the science community at large will trigger many more studies.

11.2.1. The dust polarization sky

Planck Collaboration Int. XIX (2015) presents an overview of the polarized sky as seen by *Planck* at 353 GHz (the most sensitive *Planck* channel for polarized thermal dust emission), focusing on the statistics of p and ψ. At all $N_{\rm H}$ below 10^{22} cm^{-2}, p displays a large scatter. The maximum p, observed in regions of moderate hydrogen column density ($N_{\rm H} < 2{\times}10^{21}$ cm^{-2}), is high ($p_{\rm max} \approx 20\%$). There is a general decrease in p with increasing column density above $N_{\rm H} \approx 1 \times 10^{21}$ cm^{-2} and in particular a sharp drop above $N_{\rm H} \approx 10^{22}$ cm^{-2}.

The spatial structure of ψ is characterized using the angle dispersion function $\mathcal{S}$, the local dispersion of ψ (introduced by Hildebrand et al. 2009). The polarization fraction is found to be anti-correlated with $\mathcal{S}$. The polarization angle is ordered over extended areas of several square degrees. The ordered areas are separated by long, narrow structures of high $\mathcal{S}$ that highlight interfaces where the sky polarization changes abruptly. These structures have no clear counterpart in the map of the total intensity, I. They bear a morphological resemblance to features detected in gradient maps of radio polarized emission (Iacobelli et al. 2014).

11.2.2. The Galactic magnetic field

The *Planck* maps of p and ψ contain information on the magnetic field structure. The data have been compared to synthetic polarized emission maps computed from simulations of anisotropic magnetohydrodynamical turbulence, assuming simply a uniform intrinsic polarization fraction of dust grains (Planck Collaboration Int. XX 2015). The turbulent structure of the magnetic field is able to reproduce the main statistical properties of p and ψ that are observed directly in a variety of nearby clouds (dense cores excluded). The large-scale field orientation with respect to the line of sight plays a major role in the quantitative analysis of these statistical properties. This study suggests that the large scatter of p at $N_{\rm H}$ smaller than about 10^{22} cm^{-2} is due mainly to fluctuations in the magnetic field orientation along the line of sight, rather than to changes in grain shape and/or the efficiency of grain alignment.

The formation of density structures in the interstellar medium involves turbulence, gas cooling, magnetic fields, and gravity. Polarization of thermal dust emission is well suited to studying the role of the magnetic field, because it images structure through an emission process that traces the mass of interstellar matter (Planck Collaboration XI 2014). The *Planck* I map shows elongated structures (filaments or ridges) that have counterparts in either the Stokes Q or U map, or in both, depending on the mean orientation. The correlation between Stokes maps characterizes the relative orientation between the ridges and the magnetic field. In the diffuse interstellar medium, the ridges are preferentially aligned with the magnetic field measured on the structures. This statistical trend becomes more striking for decreasing column density and, as expected from the potential effects of projection, for increasing polarization fraction (Planck Collaboration Int. XXXII 2016). Towards nearby molecular clouds the relative orientation changes progressively from preferentially parallel in areas with the lowest $N_{\rm H}$ to preferentially perpendicular in the areas with the highest $N_{\rm H}$ (Planck Collaboration Int. XXXV 2016). This change in relative orientation might be a signature of the formation of gravitationally-bound structures in the presence of a dynamically-important magnetic field.

The relation between the structure of matter and the magnetic field is also investigated in Planck Collaboration Int. XXXIII (2016) through modelling of the variations of the Stokes parameters across three filaments for different hypotheses on p. For these representative structures in molecular clouds, the

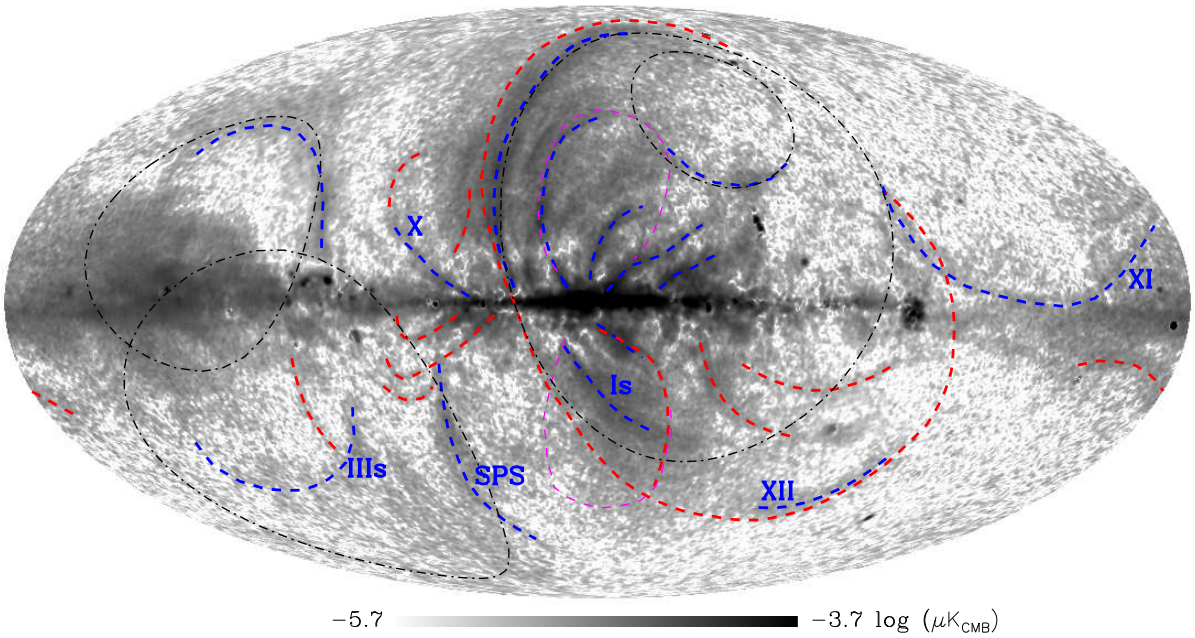

Fig. 22. Synchrotron polarization amplitude map, $P = \sqrt{Q^2 + U^2}$, at 30 GHz, smoothed to an angular resolution of 60′, produced by a weighted sum of *Planck* and WMAP data as described in Planck Collaboration XXV (2016). The traditional locii of radio loops I–IV are marked in black, a selection of the spurs identified by Vidal et al. (2015) in blue, the outline of the *Fermi* bubbles in magenta, and features discussed for the first time in Planck Collaboration XXV (2016) in red. Our measured outline for Loop I departs substantially from the traditional small circle.

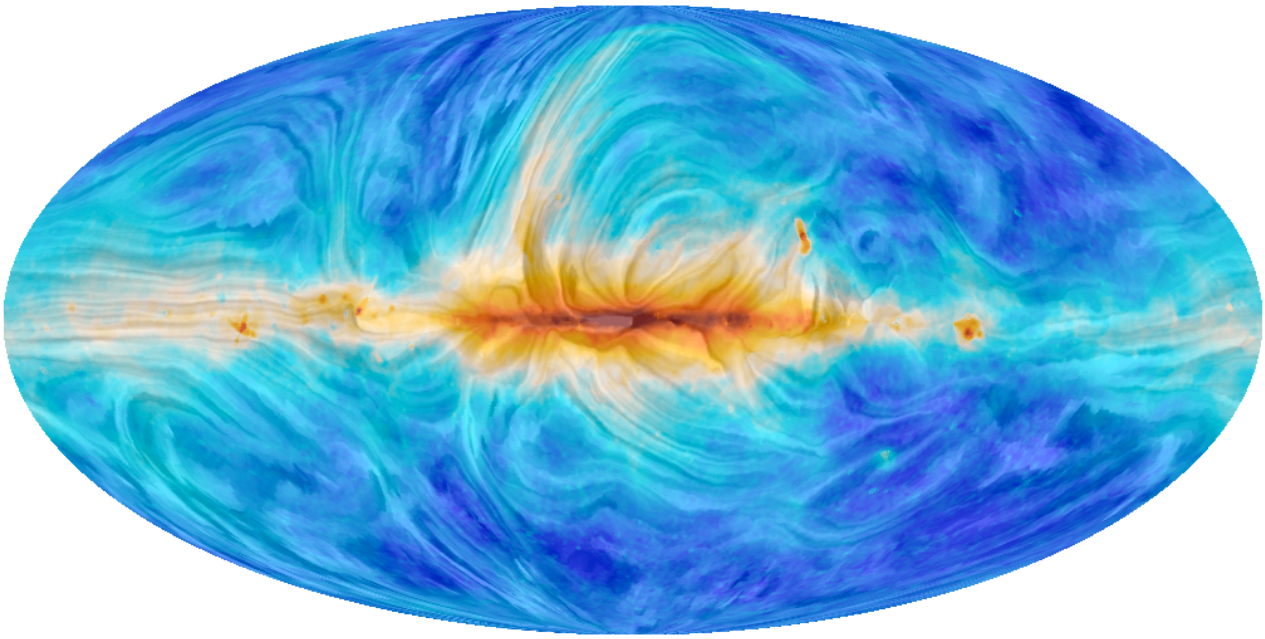

Fig. 23. All-sky view of the angle of polarization at 30 GHz, rotated by 90° to indicate the direction of the Galactic magnetic field projected on the plane of the sky. The colours represent intensity, dominated at this frequency by synchrotron emission. The "drapery" pattern was obtained by applying the line integral convolution (LIC; Cabral & Leedom 1993) procedure using an IDL implementation provided by Diego Falceta-Gonçalves (http://each.uspnet.usp.br/fgoncalves/pros/lic.pro). This gives an effective way of visualizing regions where the field is coherent, but where the field varies significantly along the line of sight, the orientation pattern is irregular and difficult to interpret.

magnetic fields in the filaments and their background have an ordered component with a mean orientation inferred from *Planck* polarization data. However, the mean magnetic field in the filaments does not have the same orientation as in the background, with a different configuration in all three cases examined. The magnetic field in a massive star-forming region, the Rosette Nebula and parent molecular cloud, is analysed in Planck Collaboration Int. XXXIV (2016), combining Faraday rotation measures from the ionized gas with dust polarized emission from the swept-up shell. This same methodology and

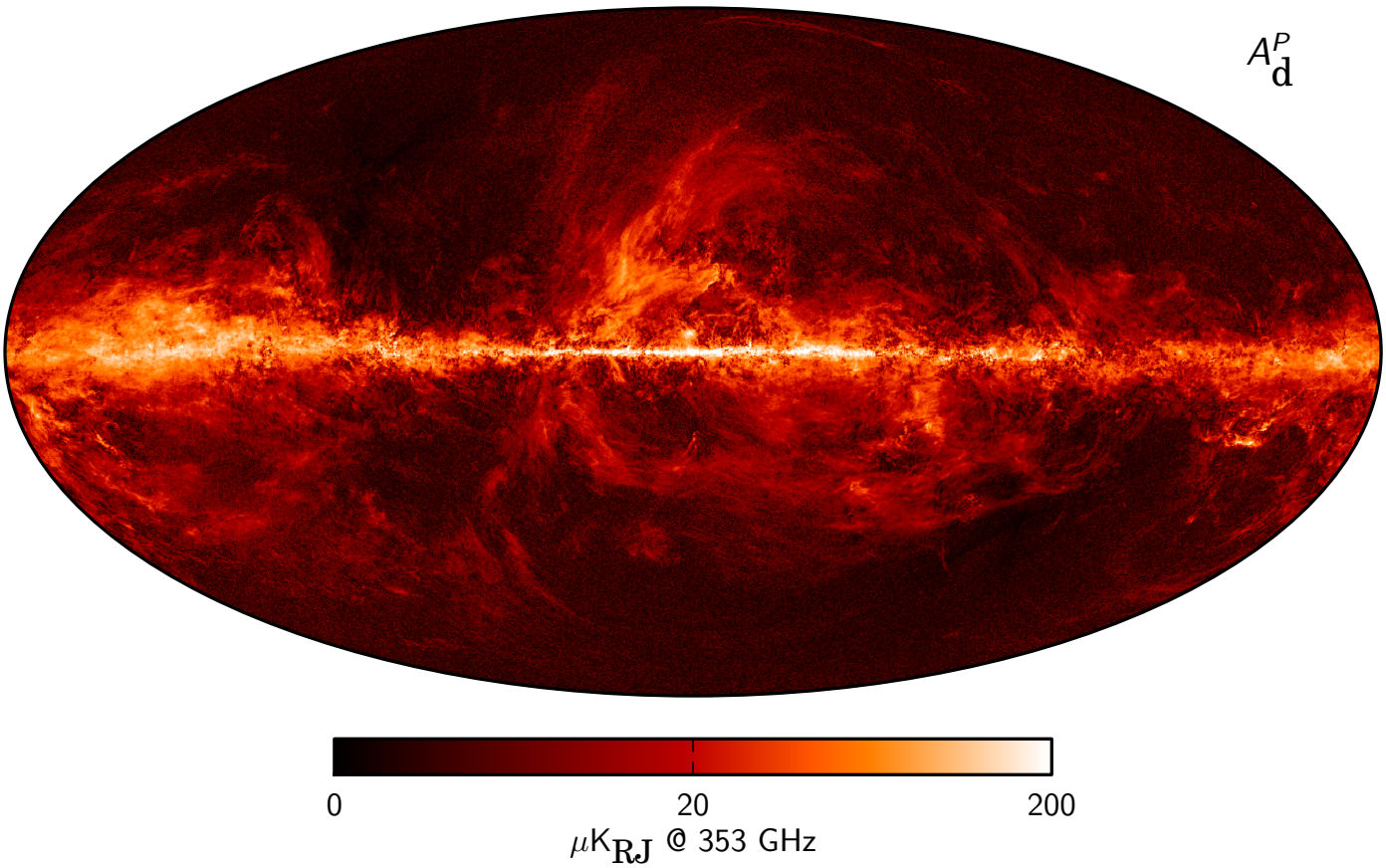

Fig. 24. Dust polarization amplitude map, $P = \sqrt{Q^2 + U^2}$, at 353 GHz, smoothed to an angular resolution of 10′, produced by the diffuse component-separation process described in Planck Collaboration X (2016) using *Planck* and WMAP data.

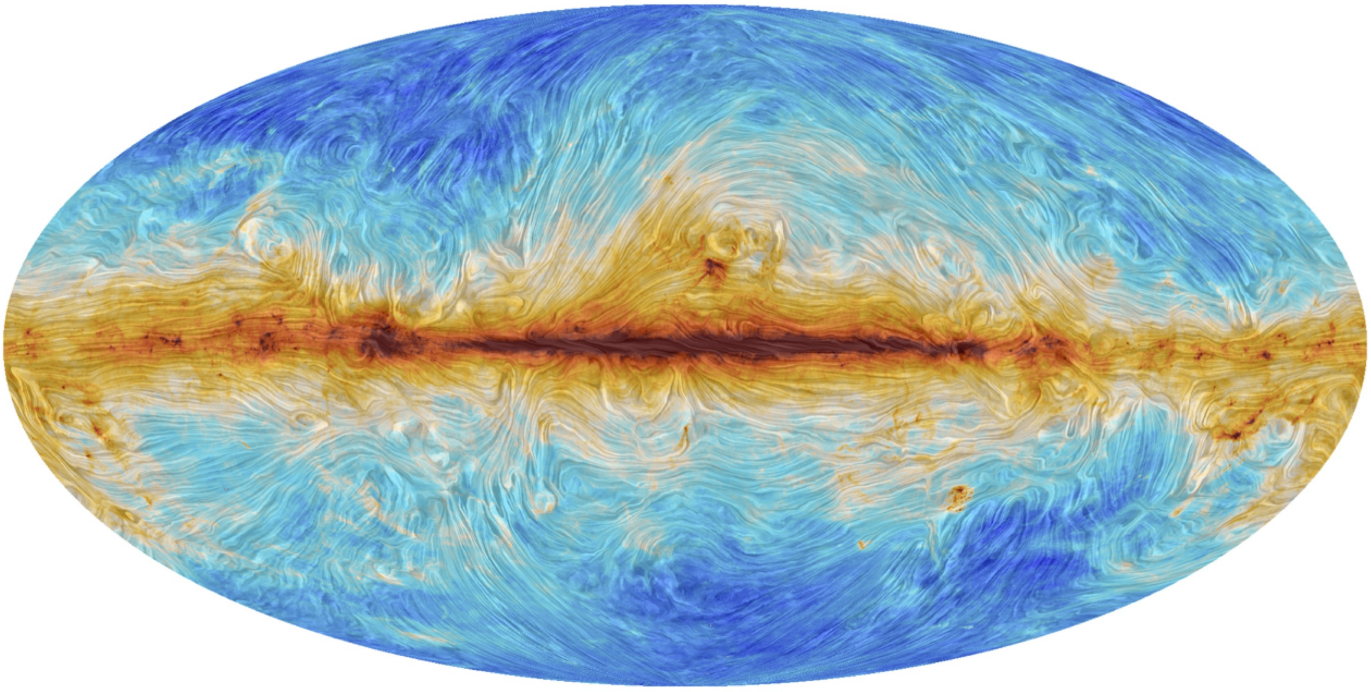

Fig. 25. All-sky view of the angle of polarization at 353 GHz, rotated by 90° to indicate the direction of the Galactic magnetic field projected on the plane of the sky and presented as in Fig. 23.

modelling framework could be used to study the field structure in a sample of massive star-forming regions.

11.2.3. Dust polarization properties

Galactic interstellar dust consists of components with different sizes and compositions, and consequently different polarization properties. The relatively large grains that are in thermal equilibrium and emit the radiation seen by *Planck* in the submillimetre also extinguish and polarize starlight in the visible (e.g., Martin 2007). Comparison of polarized emission and starlight polarization on lines of sight probed by stars provides insight into the properties of polarizing grains. In Planck Collaboration Int. XXI (2015) we specifically use P and I in the *Planck* 353 GHz channel, stellar polarization observations in the V band, the degree of polarization, p_V, and the optical depth to the star, τ_V. Lines of sight through the diffuse interstellar medium are selected with comparable values of the column density as estimated at submillimetre and visible wavelengths, and with polarization directions in emission and extinction that are close to orthogonal. Through correlations involving many lines of sight two ratios are determined, $R_{S/V} = (P/I)/(p_V/\tau_V)$ and $R_{P/p} = P/p_V$, the latter focusing directly on the polarization properties of the grains contributing to polarization. The first ratio, $R_{S/V}$, is compatible with predictions based on a range of dust models that have been developed for the diffuse interstellar medium (e.g., Martin 2007; Draine & Fraisse 2009). This estimate provides new empirical validation of many of the common underlying assumptions of the models, but is not very discriminating among them. The second ratio, $R_{P/p}$, is higher than model predictions by a factor of about 2.5. A comparable difference between data and model is observed for I/τ_V (Planck Collaboration Int. XXIX 2016). To address this, changes will be needed in the modelled optical properties of the large dust grains contributing to the submillimetre emission and polarization.

The spectral dependence at submillimetre wavelengths is also important for constraining dust models. In Planck Collaboration Int. XXII (2015) the *Planck* and WMAP data are combined to characterize the frequency dependence of emission that is spatially correlated with dust emission at 353 GHz, for both intensity and polarization, in a consistent manner. At $\nu \geq 100$ GHz, the mean spectral energy distribution (SED) of the correlated emission is well fit by a modified blackbody spectrum, for which the mean dust temperature of 19.6 K (derived from an SED fit of the dust total intensity up to 3000 GHz $= 100\,\mu$m) is adopted. It is found that the opacity has a spectral index of 1.59 ± 0.02 for polarization and 1.51 ± 0.01 for intensity. The difference between the two spectral indices is small but significant. It might result from differences in polarization efficiency among different components of interstellar dust. Results from Planck Collaboration Int. XXII (2015) also show that the spectral energy distribution increases with decreasing frequency at $\nu < 60$ GHz, for both intensity and polarization. The rise of the polarization SED towards low frequency might be accounted for by a synchrotron component correlated with dust, with no need for any polarization of the anomalous microwave emission.

11.2.4. Polarized dust and the CMB

The polarized thermal emission from diffuse Galactic dust is the main foreground present in measurements of the polarization of the CMB at frequencies above 70 GHz. The *Planck* sky coverage, spectral coverage, and sensitivity are all important for component separation of the polarization data. The polarized dust angular power spectra C_ℓ^{EE} and C_ℓ^{BB} are measured in Planck Collaboration Int. XXX (2016) over the multipole range $40 < \ell < 600$ and well away from the Galactic plane, providing a precise characterization of the dust foreground for CMB polarization.

The polarization power spectra of the dust are well-described by power laws in multipole, $C_\ell \propto \ell^\alpha$, with exponents $\alpha = -2.42 \pm 0.02$ for both the EE and BB spectra. The amplitudes of the polarization power spectra are observed to scale with the average dust brightness as $\langle I \rangle^{1.9}$, similar to the scaling found earlier (Miville-Deschênes et al. 2007). The frequency dependence of the power spectra for polarized thermal dust emission is consistent with that found for the modified blackbody emission in Planck Collaboration Int. XXII (2015). A systematic difference is discovered between the amplitudes of the Galactic B- and E-modes, such that $C_\ell^{BB}/C_\ell^{EE} = 0.5$. There is additional information coming from the dust TE and TB spectra. These general properties apply at intermediate and high Galactic latitudes in regions with low dust column density. The data show that there are no windows in the sky where primordial CMB B-mode polarization can be measured without subtraction of polarized dust emission.

12. Summary and conclusions

This paper is an overview of the *Planck* 2015 release, summarizing the main features of the products being released and the main scientific conclusions that we draw from them. Some highlights of this release are listed below.

- Data from the entire mission are now used, including both temperature and polarization, and significant improvements have been made in the understanding of beams, pointing, calibration, and systematic errors. As a result, the new products are less noisy, but even more importantly they are much better understood and the overall level of confidence is significantly increased.
- The residual systematics in the *Planck* 2015 polarization maps have been dramatically reduced compared to 2013, by as much as two orders of magnitude in some cases. Nevertheless, on angular scales greater than 10°, systematic errors in the polarization maps between 100 and 217 GHz are still non-negligible compared to the expected cosmological signal. It was not possible, for this data release, to fully characterize the large-scale residuals due to these systematic errors from the data or from simulations. Therefore all results published by the Planck Collaboration in 2015 based on CMB polarization maps use maps that have been high-pass filtered to remove structure on large angular scales. Users of the *Planck* CMB maps are warned that they are not generally usable for cosmological analysis at $\ell < 30$. Nevertheless, our polarization data are already making important contributions in a variety of analyses. More specifically, we are able to use the TE and EE angular power spectra at small scales (and to a more limited extent, at large angular scales) over the full sky, reaching the expected sensitivity. This allows us to estimate cosmological parameters independently of TT, and in combination with TT.
- A large set of simulations accompanies the release, including up to 10 000 realizations of signal and noise; this has been used to test and verify methods of analysis and to estimate uncertainties.

- We measure the amplitude and direction of the Solar dipole to the best precision so far.
- One of the most notable improvements in this release is that LFI, HFI, and WMAP now agree on the amplitude of fluctuations in the CMB to within a few tenths of a percent on angular scales from the dipole through the first acoustic peak.
- At large angular scales, we are now able to use *Planck*-only products to carry out cosmological analysis. Specifically, we can estimate the optical depth of reionization, τ, independently of other experiments. The value of τ is smaller than found in previous determination, implying later reionization.
- Foregrounds can be separated effectively over larger areas of the sky than in the 2013 release, allowing more sky to be used for cosmology, and producing high-quality maps of synchrotron, free-free, spinning dust, thermal dust, and CO emission.
- Our 2015 results for cosmology are consistent with our 2013 results, but with smaller uncertainties, and covering a greater range of science implications.
- Our best-fit 2015 cosmological parameters confirm the basic 6-parameter ΛCDM scenario that we determined in 2013. There is no compelling evidence for any extensions to the 6-parameter model, or any need for new physics. Depending somewhat on the precise data combinations used, five of the six parameters are now measured to better than 1% precision. Areas that were in "tension" in 2013 (σ_8 and weak galaxy lensing) remain in tension today, although the disagreement is lessened when only particular subsets of the external data are considered.
- Using only *Planck* data, we find that the Universe is flat to 0.7% (1σ). Including BAO data, the constraint tightens to a remarkable 0.25%.
- Using the *Planck* temperature data over the whole sky, together with our recent work combining *Planck* and BICEP2/Keck data, we have obtained the best current upper limits on the tensor-to-scalar ratio obtained to date.
- Improved limits on primordial non-Gaussianity ($f_{\rm NL}$) are about 30% tighter than before, reaching the expected sensitivity of *Planck* when including polarization.
- Models of inflation are more tightly constrained than ever before, with the simplest ϕ^n models being ruled out for $n \geq 2$.
- We have obtained the most restrictive limits yet on the amplitude of primordial magnetic fields.
- *Planck*'s measurement of lensing of the CMB has the highest signal-to-noise ratio yet achieved, 40σ.
- The second *Planck* catalogues of compact sources, SZ clusters, and Galactic cold clumps, are larger than the previous ones and better-characterized in terms of completeness and reliability.

Planck continues to provide a rich harvest of data for cosmology and astrophysics.

Acknowledgements. Planck is a project of the European Space Agency in cooperation with the scientific community, which started in 1993. ESA led the project, developed the satellite, integrated the payload into it, and launched and operated the satellite. Two Consortia, comprising around 100 scientific institutes within Europe, the USA, and Canada, and funded by agencies from the participating countries, developed and operated the scientific instruments LFI and HFI. The Consortia are also responsible for scientific processing of the acquired data. The Consortia are led by the Principal Investigators: J.-L. Puget in France for HFI (funded principally by CNES and CNRS/INSU-IN2P3) and N. Mandolesi in Italy for LFI (funded principally via ASI). NASA's US Planck Project, based at JPL and involving scientists at many US institutions, contributes significantly to the efforts of these two Consortia. A third Consortium, led by H.U. Norgaard-Nielsen and supported by the Danish Natural Research Council, contributed to the reflector programme. These three Consortia, together with ESA's Planck Science Office, form the Planck Collaboration. A description of the Planck Collaboration and a list of its members, indicating which technical or scientific activities they have been involved in, can be found at http://www.cosmos.esa.int/web/planck/planck-collaboration. The Planck Collaboration acknowledges the support of: ESA; CNES and CNRS/INSU-IN2P3-INP (France); ASI, CNR, and INAF (Italy); NASA and DoE (USA); STFC and UKSA (UK); CSIC, MINECO, JA, and RES (Spain); Tekes, AoF, and CSC (Finland); DLR and MPG (Germany); CSA (Canada); DTU Space (Denmark); SER/SSO (Switzerland); RCN (Norway); SFI (Ireland); FCT/MCTES (Portugal); ERC and PRACE (EU). We thank Diego Falceta-Gonçalves for providing the technique for making the line-integral-convolution maps presented in Figs. 23 and 25.

References

Bennett, C. L., Larson, D., Weiland, J. L., et al. 2013, ApJ, 208, 20
Benoît, A., Ade, P., Amblard, A., et al. 2004, A&A, 424, 571
Bersanelli, M., Mandolesi, N., Butler, R. C., et al. 2010, A&A, 520, A4
Béthermin, M., Daddi, E., Magdis, G., et al. 2012, ApJ, 757, L23
BICEP2 Collaboration 2014, Phys. Rev. Lett., 112, 241101
BICEP2/Keck Array and Planck Collaborations 2015, Phys. Rev. Lett., 114, 101301
Bond, J. R., Contaldi, C., & Pogosyan, D. 2003, Roy. Soc. London Philos. Trans. Ser. A, 361, 2435
Cabral, B., & Leedom, L. C. 1993, in Special Interest Group on GRAPHics and Interactive Techniques Proceedings, 263
Cardoso, J., Martin, M., Delabrouille, J., Betoule, M., & Patanchon, G. 2008, special issue on Signal Processing for Astronomical and Space Research Applications, IEEE J. Selected Topics in Signal Processing, 2, 735
Corasaniti, P. S., & Melchiorri, A. 2008, Phys. Rev. D, 77, 103507
de Bernardis, P., Ade, P. A. R., Bock, J. J., et al. 2002, ApJ, 564, 559
Delabrouille, J., Cardoso, J.-F., & Patanchon, G. 2003, MNRAS, 346, 1089
Delabrouille, J., Cardoso, J., Le Jeune, M., et al. 2009, A&A, 493, 835
Delabrouille, J., Betoule, M., Melin, J.-B., et al. 2013, A&A, 553, A96
Draine, B. T., & Fraisse, A. A. 2009, ApJ, 696, 1
Durrer, R., Novosyadlyj, B., & Apunevych, S. 2003, ApJ, 583, 33
Eriksen, H. K., Hansen, F. K., Banday, A. J., Górski, K. M., & Lilje, P. B. 2004, ApJ, 605, 14
Eriksen, H. K., Dickinson, C., Lawrence, C. R., et al. 2006, ApJ, 641, 665
Eriksen, H. K., Jewell, J. B., Dickinson, C., et al. 2008, ApJ, 676, 10
Fernández-Cobos, R., Vielva, P., Barreiro, R. B., & Martínez-González, E. 2012, MNRAS, 420, 2162
Górski, K. M., Hivon, E., Banday, A. J., et al. 2005, ApJ, 622, 759
Granett, B. R., Neyrinck, M. C., & Szapudi, I. 2008, ApJ, 683, L99
Hamaker, J. P., & Bregman, J. D. 1996, A&AS, 117, 161
Hancock, S., & Rocha, G. 1997, in Microwave Background Anisotropies, eds. F. R. Bouchet, R. Gispert, B. Guiderdoni, & J. Trân Thanh Vân, 179
Haslam, C. G. T., Salter, C. J., Stoffel, H., & Wilson, W. E. 1982, A&AS, 47, 1
Heeschen, D. S., & Howard, W. E. 1974, in Trans. IAU, Vol. XVB, Proc. 1973, General Assembly, eds. G. Contopoulos, & A. Jappel (Dordrecht: Reidel), 165
Hildebrand, R. H., Kirby, L., Dotson, J. L., Houde, M., & Vaillancourt, J. E. 2009, ApJ, 696, 567
Hinshaw, G., Nolta, M. R., Bennett, C. L., et al. 2007, ApJS, 170, 288
Hinshaw, G., Weiland, J. L., Hill, R. S., et al. 2009, ApJS, 180, 225
Hu, W., Hedman, M. M., & Zaldarriaga, M. 2003, Phys. Rev. D, 67, 043004
Hurier, G., Macías-Pérez, J. F., & Hildebrandt, S. R. 2013, A&A, 558, A118
Iacobelli, M., Burkhart, B., Haverkorn, M., et al. 2014, A&A, 566, A5
Jarosik, N., Bennett, C. L., Dunkley, J., et al. 2011, ApJS, 192, 14
Jones, W. C., Ade, P. A. R., Bock, J. J., et al. 2006, ApJ, 647, 823
Keihänen, E., Keskitalo, R., Kurki-Suonio, H., Poutanen, T., & Sirviö, A. 2010, A&A, 510, A57
Knox, L., & Page, L. 2000, Phys. Rev. Lett., 85, 1366
Koch, P. M., Tang, Y.-W., & Ho, P. T. P. 2010, ApJ, 721, 815
Lamarre, J., Puget, J., Ade, P. A. R., et al. 2010, A&A, 520, A9
Leahy, J. P., Bersanelli, M., D'Arcangelo, O., et al. 2010, A&A, 520, A8
Martin, P. G. 2007, in EAS Pub. Ser. 23, eds. M.-A. Miville-Deschênes, & F. Boulanger, 165
Matthews, B. C., McPhee, C. A., Fissel, L. M., & Curran, R. L. 2009, ApJS, 182, 143
Matthews, T. G., Ade, P. A. R., Angilè, F. E., et al. 2014, ApJ, 784, 116
Melin, J.-B., & Bartlett, J. G. 2015, A&A, 578, A21
Mennella, A., Butler, R. C., Curto, A., et al. 2011, A&A, 536, A3
Mertsch, P., & Sarkar, S. 2013, JCAP, 6, 41
Mitra, S., Rocha, G., Górski, K. M., et al. 2011, ApJS, 193, 5
Miville-Deschênes, M., & Lagache, G. 2005, ApJS, 157, 302

Miville-Deschênes, M.-A., Lagache, G., Boulanger, F., & Puget, J.-L. 2007, A&A, 469, 595
Montier, L. A., Pelkonen, V., Juvela, M., Ristorcelli, I., & Marshall, D. J. 2010, A&A, 522, A83
Oppermann, N., Junklewitz, H., Robbers, G., et al. 2012, A&A, 542, A93
Page, L., Nolta, M. R., Barnes, C., et al. 2003, ApJS, 148, 233
Planck Collaboration 2005, ESA publication ESA-SCI(2005)/01 [arXiv:astro-ph/0604069]
Planck Collaboration 2015, The Explanatory Supplement to the *Planck* 2015 results, http://wiki.cosmos.esa.int/planckpla/index.php/Main_Page (ESA)
Planck Collaboration I. 2011, A&A, 536, A1
Planck Collaboration VII. 2011, A&A, 536, A7
Planck Collaboration XIII. 2011, A&A, 536, A13
Planck Collaboration XIV. 2011, A&A, 536, A14
Planck Collaboration XXII. 2011, A&A, 536, A22
Planck Collaboration XXIII. 2011, A&A, 536, A23
Planck Collaboration I. 2014, A&A, 571, A1
Planck Collaboration II. 2014, A&A, 571, A2
Planck Collaboration IV. 2014, A&A, 571, A4
Planck Collaboration V. 2014, A&A, 571, A5
Planck Collaboration VI. 2014, A&A, 571, A6
Planck Collaboration VII. 2014, A&A, 571, A7
Planck Collaboration XI. 2014, A&A, 571, A11
Planck Collaboration XIII. 2014, A&A, 571, A13
Planck Collaboration XIV. 2014, A&A, 571, A14
Planck Collaboration XV. 2014, A&A, 571, A15
Planck Collaboration XVI. 2014, A&A, 571, A16
Planck Collaboration XVII. 2014, A&A, 571, A17
Planck Collaboration XIX. 2014, A&A, 571, A19
Planck Collaboration XXI. 2014, A&A, 571, A21
Planck Collaboration XXII. 2014, A&A, 571, A22
Planck Collaboration XXVI. 2014, A&A, 571, A26
Planck Collaboration XXVII. 2014, A&A, 571, A27
Planck Collaboration XXVIII. 2014, A&A, 571, A28
Planck Collaboration XXIX. 2014, A&A, 571, A29
Planck Collaboration XXXI. 2014, A&A, 571, A31
Planck Collaboration I. 2016, A&A, 594, A1
Planck Collaboration II. 2016, A&A, 594, A2
Planck Collaboration III. 2016, A&A, 594, A3
Planck Collaboration IV. 2016, A&A, 594, A4
Planck Collaboration V. 2016, A&A, 594, A5
Planck Collaboration VI. 2016, A&A, 594, A6
Planck Collaboration VII. 2016, A&A, 594, A7
Planck Collaboration VIII. 2016, A&A, 594, A8
Planck Collaboration IX. 2016, A&A, 594, A9
Planck Collaboration X. 2016, A&A, 594, A10
Planck Collaboration XI. 2016, A&A, 594, A11
Planck Collaboration XII. 2016, A&A, 594, A12
Planck Collaboration XIII. 2016, A&A, 594, A13
Planck Collaboration XIV. 2016, A&A, 594, A14
Planck Collaboration XV. 2016, A&A, 594, A15
Planck Collaboration XVI. 2016, A&A, 594, A16
Planck Collaboration XVII. 2016, A&A, 594, A17
Planck Collaboration XVIII. 2016, A&A, 594, A18
Planck Collaboration XIX. 2016, A&A, 594, A19
Planck Collaboration XX. 2016, A&A, 594, A20
Planck Collaboration XXI. 2016, A&A, 594, A21
Planck Collaboration XXII. 2016, A&A, 594, A22
Planck Collaboration XXIII. 2016, A&A, 594, A23
Planck Collaboration XXIV. 2016, A&A, 594, A24
Planck Collaboration XXV. 2016, A&A, 594, A25
Planck Collaboration XXVI. 2016, A&A, 594, A26
Planck Collaboration XXVII. 2016, A&A, 594, A27
Planck Collaboration XXVIII. 2016, A&A, 594, A28
Planck Collaboration Int. XIX. 2015, A&A, 576, A104
Planck Collaboration Int. XX. 2015, A&A, 576, A105
Planck Collaboration Int. XXI. 2015, A&A, 576, A106
Planck Collaboration Int. XXII. 2015, A&A, 576, A107
Planck Collaboration Int. XXIX. 2016, A&A, 586, A132
Planck Collaboration Int. XXX. 2016, A&A, 586, A133
Planck Collaboration Int. XXXII. 2016, A&A, 586, A135
Planck Collaboration Int. XXXIII. 2016, A&A, 586, A136
Planck Collaboration Int. XXXIV. 2016, A&A, 586, A137
Planck Collaboration Int. XXXV. 2016, A&A, 586, A138
Planck HFI Core Team 2011, A&A, 536, A4
Pryke, C., Ade, P., Bock, J., et al. 2009, ApJ, 692, 1247
Readhead, A. C. S., Myers, S. T., Pearson, T. J., et al. 2004, Science, 306, 836
Remazeilles, M., Delabrouille, J., & Cardoso, J.-F. 2011, MNRAS, 410, 2481
Scott, D., & White, M. 1994, in CMB Anisotropies Two Years after COBE: Observations, Theory and the Future, ed. L. M. Krauss, 214
Tauber, J. A., Mandolesi, N., Puget, J., et al. 2010, A&A, 520, A1
Tristram, M., Filliard, C., Perdereau, O., et al. 2011, A&A, 534, A88
Vidal, M., Dickinson, C., Davies, R. D., & Leahy, J. P. 2015, MNRAS, 432, 656
von der Linden, A., Mantz, A., Allen, S. W., et al. 2014, MNRAS, 443, 1973
Ward-Thompson, D., Sen, A. K., Kirk, J. M., & Nutter, D. 2009, MNRAS, 398, 394

[1] APC, AstroParticule et Cosmologie, Université Paris Diderot, CNRS/IN2P3, CEA/lrfu, Observatoire de Paris, Sorbonne Paris Cité, 10 rue Alice Domon et Léonie Duquet, 75205 Paris Cedex 13, France
[2] Aalto University Metsähovi Radio Observatory and Dept of Radio Science and Engineering, PO Box 13000, 00076 Aalto, Finland
[3] Aalto University Metsähovi Radio Observatory, PO Box 13000, 00076 Aalto, Finland
[4] Academy of Sciences of Tatarstan, Bauman Str., 20, Kazan, 420111, Republic of Tatarstan, Russia
[5] African Institute for Mathematical Sciences, 6-8 Melrose Road, Muizenberg, Cape Town, South Africa
[6] Agenzia Spaziale Italiana Science Data Center, Via del Politecnico snc, 00133, Roma, Italy
[7] Aix-Marseille Université, CNRS, LAM (Laboratoire d'Astrophysique de Marseille) UMR 7326, 13388, Marseille, France
[8] Aix Marseille Université, Centre de Physique Théorique, 163 avenue de Luminy, 13288, Marseille, France
[9] Astrophysics Group, Cavendish Laboratory, University of Cambridge, J J Thomson Avenue, Cambridge CB3 0HE, UK
[10] Astrophysics & Cosmology Research Unit, School of Mathematics, Statistics & Computer Science, University of KwaZulu-Natal, Westville Campus, Private Bag X54001, Durban 4000, South Africa
[11] Atacama Large Millimeter/submillimeter Array, ALMA Santiago Central Offices, Alonso de Cordova 3107, Vitacura, Casilla 763 0355, Santiago, Chile
[12] CGEE, SCS Qd 9, Lote C, Torre C, 4° andar, Ed. Parque Cidade Corporate, CEP 70308-200, Brasília, DF, Brazil
[13] CITA, University of Toronto, 60 St. George St., Toronto, ON M5S 3H8, Canada
[14] CNRS, IRAP, 9 Av. colonel Roche, BP 44346, 31028 Toulouse Cedex 4, France
[15] CRANN, Trinity College, Dublin, Ireland
[16] California Institute of Technology, Pasadena, California, USA
[17] Centre for Theoretical Cosmology, DAMTP, University of Cambridge, Wilberforce Road, Cambridge CB3 0WA, UK
[18] Centro de Estudios de Física del Cosmos de Aragón (CEFCA), Plaza San Juan, 1, Planta 2, 44001, Teruel, Spain
[19] Computational Cosmology Center, Lawrence Berkeley National Laboratory, Berkeley, California, USA
[20] Consejo Superior de Investigaciones Científicas (CSIC), Madrid, Spain
[21] DSM/Irfu/SPP, CEA-Saclay, 91191 Gif-sur-Yvette Cedex, France
[22] DTU Space, National Space Institute, Technical University of Denmark, Elektrovej 327, 2800 Kgs. Lyngby, Denmark
[23] Département de Physique Théorique, Université de Genève, 24 quai E. Ansermet, 1211 Genève 4, Switzerland
[24] Dark Cosmology Centre, Niels Bohr Institute, University of Copenhagen, Juliane Maries Vej 30, 2100 Copenhagen, Denmark
[25] Departamento de Astrofísica, Universidad de La Laguna (ULL), 38206 La Laguna, Tenerife, Spain
[26] Departamento de Física, Universidad de Oviedo, Avda. Calvo Sotelo s/n, Oviedo, Spain
[27] Departamento de Matemáticas, Estadística y Computación, Universidad de Cantabria, Avda. de los Castros s/n, Santander, Spain
[28] Departamento de Matemáticas, Universidad de Oviedo, Avda. Calvo Sotelo s/n, Oviedo, Spain
[29] Department of Astronomy and Astrophysics, University of Toronto, 50 Saint George Street, Toronto, Ontario, Canada

[30] Department of Astronomy and Geodesy, Kazan Federal University, Kremlevskaya Str., 18, Kazan, 420008, Russia
[31] Department of Astrophysics/IMAPP, Radboud University Nijmegen, PO Box 9010, 6500 GL Nijmegen, The Netherlands
[32] Department of Physics & Astronomy, University of British Columbia, 6224 Agricultural Road, Vancouver, British Columbia, Canada
[33] Department of Physics and Astronomy, Dana and David Dornsife College of Letter, Arts and Sciences, University of Southern California, Los Angeles, CA 90089, USA
[34] Department of Physics and Astronomy, Johns Hopkins University, Bloomberg Center 435, 3400 N. Charles St., Baltimore, MD 21218, USA
[35] Department of Physics and Astronomy, University College London, London WC1E 6BT, UK
[36] Department of Physics and Astronomy, University of Sussex, Brighton BN1 9QH, UK
[37] Department of Physics, Florida State University, Keen Physics Building, 77 Chieftan Way, Tallahassee, Florida, USA
[38] Department of Physics, Gustaf Hällströmin katu 2a, University of Helsinki, Helsinki, Finland
[39] Department of Physics, Princeton University, Princeton, New Jersey, USA
[40] Department of Physics, University of Alberta, 11322-89 Avenue, Edmonton, Alberta, T6G 2G7, Canada
[41] Department of Physics, University of California, Berkeley, California, USA
[42] Department of Physics, University of California, One Shields Avenue, Davis, California, USA
[43] Department of Physics, University of California, Santa Barbara, California, USA
[44] Department of Physics, University of Illinois at Urbana-Champaign, 1110 West Green Street, Urbana, Illinois, USA
[45] Dipartimento di Fisica e Astronomia G. Galilei, Università degli Studi di Padova, via Marzolo 8, 35131 Padova, Italy
[46] Dipartimento di Fisica e Astronomia, Alma Mater Studiorum, Università degli Studi di Bologna, Viale Berti Pichat 6/2, 40127 Bologna, Italy
[47] Dipartimento di Fisica e Scienze della Terra, Università di Ferrara, Via Saragat 1, 44122 Ferrara, Italy
[48] Dipartimento di Fisica, Università La Sapienza, P.le A. Moro 2, Roma, Italy
[49] Dipartimento di Fisica, Università degli Studi di Milano, Via Celoria, 16, Milano, Italy
[50] Dipartimento di Fisica, Università degli Studi di Trieste, via A. Valerio 2, Trieste, Italy
[51] Dipartimento di Fisica, Università di Roma Tor Vergata, Via della Ricerca Scientifica 1, Roma, Italy
[52] Dipartimento di Matematica, Università di Roma Tor Vergata, Via della Ricerca Scientifica 1, Roma, Italy
[53] Discovery Center, Niels Bohr Institute, Blegdamsvej 17, Copenhagen, Denmark
[54] Discovery Center, Niels Bohr Institute, Copenhagen University, Blegdamsvej 17, Copenhagen, Denmark
[55] European Southern Observatory, ESO Vitacura, Alonso de Cordova 3107, Vitacura, Casilla 19001, Santiago, Chile
[56] European Space Agency, ESAC, Camino bajo del Castillo s/n, Urbanización Villafranca del Castillo, Villanueva de la Cañada, Madrid, Spain
[57] European Space Agency, ESAC, Planck Science Office, Camino bajo del Castillo s/n, Urbanización Villafranca del Castillo, Villanueva de la Cañada, Madrid, Spain
[58] European Space Agency, ESTEC, Keplerlaan 1, 2201 AZ Noordwijk, The Netherlands
[59] Finnish Centre for Astronomy with ESO (FINCA), University of Turku, Väisäläntie 20, 21500 Piikkiö, Finland
[60] GEPI, Observatoire de Paris, Section de Meudon, 5 place J. Janssen, 92195 Meudon Cedex, France
[61] Gran Sasso Science Institute, INFN, viale F. Crispi 7, 67100 L'Aquila, Italy
[62] HGSFP and University of Heidelberg, Theoretical Physics Department, Philosophenweg 16, 69120, Heidelberg, Germany
[63] Haverford College Astronomy Department, 370 Lancaster Avenue, Haverford, Pennsylvania, USA
[64] Helsinki Institute of Physics, Gustaf Hällströmin katu 2, University of Helsinki, Helsinki, Finland
[65] ICTP South American Institute for Fundamental Research, Instituto de Física Teórica, Universidade Estadual Paulista, São Paulo, Brazil
[66] INAF – Osservatorio Astrofisico di Catania, Via S. Sofia 78, Catania, Italy
[67] INAF – Osservatorio Astronomico di Padova, Vicolo dell'Osservatorio 5, Padova, Italy
[68] INAF – Osservatorio Astronomico di Roma, via di Frascati 33, Monte Porzio Catone, Italy
[69] INAF – Osservatorio Astronomico di Trieste, Via G.B. Tiepolo 11, Trieste, Italy
[70] INAF/IASF Bologna, Via Gobetti 101, Bologna, Italy
[71] INAF/IASF Milano, Via E. Bassini 15, Milano, Italy
[72] INFN, Sezione di Bologna, viale Berti Pichat 6/2, 40127 Bologna, Italy
[73] INFN, Sezione di Ferrara, Via Saragat 1, 44122 Ferrara, Italy
[74] INFN, Sezione di Roma 1, Università di Roma Sapienza, Piazzale Aldo Moro 2, 00185 Roma, Italy
[75] INFN, Sezione di Roma 2, Università di Roma Tor Vergata, Via della Ricerca Scientifica 1, Roma, Italy
[76] INFN/National Institute for Nuclear Physics, Via Valerio 2, 34127 Trieste, Italy
[77] IPAG: Institut de Planétologie et d'Astrophysique de Grenoble, Université Grenoble Alpes, IPAG; CNRS, IPAG, 38000 Grenoble, France
[78] ISDC, Department of Astronomy, University of Geneva, Ch. d'Ecogia 16, 1290 Versoix, Switzerland
[79] IUCAA, Post Bag 4, Ganeshkhind, Pune University Campus, Pune 411 007, India
[80] Imperial College London, Astrophysics group, Blackett Laboratory, Prince Consort Road, London, SW7 2AZ, UK
[81] Infrared Processing and Analysis Center, California Institute of Technology, Pasadena, CA 91125, USA
[82] Institut Néel, CNRS, Université Joseph Fourier Grenoble I, 25 rue des Martyrs, Grenoble, France
[83] Institut Universitaire de France, 103 bd Saint-Michel, 75005 Paris, France
[84] Institut d'Astrophysique Spatiale, CNRS, Univ. Paris-Sud, Université Paris-Saclay, Bât. 121, 91405 Orsay Cedex, France
[85] Institut d'Astrophysique de Paris, CNRS (UMR 7095), 98bis boulevard Arago, 75014 Paris, France
[86] Institut für Theoretische Teilchenphysik und Kosmologie, RWTH Aachen University, 52056 Aachen, Germany
[87] Institute for Space Sciences, Bucharest-Magurale, Romania
[88] Institute of Astronomy, University of Cambridge, Madingley Road, Cambridge CB3 0HA, UK
[89] Institute of Theoretical Astrophysics, University of Oslo, Blindern, Oslo, Norway
[90] Instituto Nacional de Astrofísica, Óptica y Electrónica (INAOE), Apartado Postal 51 y 216, 72000 Puebla, México
[91] Instituto de Astrofísica de Canarias, C/Vía Láctea s/n, La Laguna, Tenerife, Spain
[92] Instituto de Física de Cantabria (CSIC-Universidad de Cantabria), Avda. de los Castros s/n, Santander, Spain
[93] Istituto Nazionale di Astrofisica – Osservatorio Astronomico di Roma, Via Frascati 33, 00040 Monte Porzio Catone (RM), Italy
[94] Istituto Nazionale di Fisica Nucleare, Sezione di Padova, via Marzolo 8, 35131 Padova, Italy
[95] Jet Propulsion Laboratory, California Institute of Technology, 4800 Oak Grove Drive, Pasadena, California, USA
[96] Jodrell Bank Centre for Astrophysics, Alan Turing Building, School of Physics and Astronomy, The University of Manchester, Oxford Road, Manchester, M13 9PL, UK

[97] Kavli Institute for Cosmological Physics, University of Chicago, Chicago, IL 60637, USA
[98] Kavli Institute for Cosmology Cambridge, Madingley Road, Cambridge, CB3 0HA, UK
[99] Kazan Federal University, 18 Kremlyovskaya St., Kazan 420008, Russia
[100] LAL, Université Paris-Sud, CNRS/IN2P3, Orsay, France
[101] LERMA, CNRS, Observatoire de Paris, 61 Avenue de l'Observatoire, Paris, France
[102] LESIA, Observatoire de Paris, CNRS, UPMC, Université Paris-Diderot, 5 Place J. Janssen, 92195 Meudon, France
[103] Laboratoire AIM, IRFU/Service d'Astrophysique - CEA/DSM - CNRS - Université Paris Diderot, Bât. 709, CEA-Saclay, 91191 Gif-sur-Yvette Cedex, France
[104] Laboratoire Traitement et Communication de l'Information, CNRS (UMR 5141) and Télécom ParisTech, 46 rue Barrault, 75634 Paris Cedex 13, France
[105] Laboratoire de Physique Subatomique et Cosmologie, Université Grenoble-Alpes, CNRS/IN2P3, 53 rue des Martyrs, 38026 Grenoble Cedex, France
[106] Laboratoire de Physique Théorique, Université Paris-Sud 11 & CNRS, Bâtiment 210, 91405 Orsay, France
[107] Lawrence Berkeley National Laboratory, Berkeley, California, USA
[108] Lebedev Physical Institute of the Russian Academy of Sciences, Astro Space Centre, 84/32 Profsoyuznaya st., Moscow, GSP-7, 117997, Russia
[109] Leung Center for Cosmology and Particle Astrophysics, National Taiwan University, Taipei 10617, Taiwan
[110] Max-Planck-Institut für Astrophysik, Karl-Schwarzschild-Str. 1, 85741 Garching, Germany
[111] Max-Planck-Institut für Extraterrestrische Physik, Giessenbachstraße, 85748 Garching, Germany
[112] McGill Physics, Ernest Rutherford Physics Building, McGill University, 3600 rue University, Montréal, QC, H3A 2T8, Canada
[113] Moscow Institute of Physics and Technology, Institutsky per., 9, Dolgoprudny, 141700, Russia
[114] Mullard Space Science Laboratory, University College London, Surrey RH5 6NT, UK
[115] National University of Ireland, Department of Experimental Physics, Maynooth, Co. Kildare, Ireland
[116] Nicolaus Copernicus Astronomical Center, Bartycka 18, 00-716 Warsaw, Poland
[117] Niels Bohr Institute, Blegdamsvej 17, Copenhagen, Denmark
[118] Niels Bohr Institute, Copenhagen University, Blegdamsvej 17, Copenhagen, Denmark
[119] Nordita (Nordic Institute for Theoretical Physics), Roslagstullsbacken 23, 106 91 Stockholm, Sweden
[120] Optical Science Laboratory, University College London, Gower Street, London, UK
[121] Perimeter Institute for Theoretical Physics, Waterloo ON N2L 2Y5, Canada
[122] Physics Department, Shahid Beheshti University, Tehran, Iran
[123] SISSA, Astrophysics Sector, via Bonomea 265, 34136, Trieste, Italy
[124] SMARTEST Research Centre, Università degli Studi e-Campus, Via Isimbardi 10, Novedrate (CO), 22060, Italy
[125] School of Chemistry and Physics, University of KwaZulu-Natal, Westville Campus, Private Bag X54001, 4000 Durban, South Africa
[126] School of Physics and Astronomy, Cardiff University, Queens Buildings, The Parade, Cardiff, CF24 3AA, UK
[127] School of Physics and Astronomy, University of Nottingham, Nottingham NG7 2RD, UK
[128] Simon Fraser University, Department of Physics, 8888 University Drive, Burnaby BC, Canada
[129] Sorbonne Université-UPMC, UMR7095, Institut d'Astrophysique de Paris, 98bis Boulevard Arago, 75014 Paris, France
[130] Space Research Institute (IKI), Russian Academy of Sciences, Profsoyuznaya Str, 84/32, 117997 Moscow, Russia
[131] Space Sciences Laboratory, University of California, Berkeley, California, USA
[132] Special Astrophysical Observatory, Russian Academy of Sciences, Nizhnij Arkhyz, Zelenchukskiy region, 369167 Karachai-Cherkessian Republic, Russia
[133] Stanford University, Dept of Physics, Varian Physics Bldg, 382 Via Pueblo Mall, Stanford, California, USA
[134] Sterrewacht Leiden, PO Box 9513, 2300 RA Leiden, The Netherlands
[135] Sub-Department of Astrophysics, University of Oxford, Keble Road, Oxford OX1 3RH, UK
[136] Sydney Institute for Astronomy, School of Physics A28, University of Sydney, NSW 2006, Australia
[137] TÜBİTAK National Observatory, Akdeniz University Campus, 07058 Antalya, Turkey
[138] The Oskar Klein Centre for Cosmoparticle Physics, Department of Physics, Stockholm University, AlbaNova, 106 91 Stockholm, Sweden
[139] Theory Division, PH-TH, CERN, 1211 Geneva 23, Switzerland
[140] UPMC Univ Paris 06, UMR7095, 98bis Boulevard Arago, 75014 Paris, France
[141] Universität Heidelberg, Institut für Theoretische Astrophysik, Philosophenweg 12, 69120 Heidelberg, Germany
[142] Université Denis Diderot (Paris 7), 75205 Paris Cedex 13, France
[143] Université de Toulouse, UPS-OMP, IRAP, 31028 Toulouse Cedex 4, France
[144] Universities Space Research Association, Stratospheric Observatory for Infrared Astronomy, MS 232-11, Moffett Field, CA 94035, USA
[145] University Observatory, Ludwig Maximilian University of Munich, Scheinerstrasse 1, 81679 Munich, Germany
[146] University of Granada, Departamento de Física Teórica y del Cosmos, Facultad de Ciencias, Granada, Spain
[147] University of Granada, Instituto Carlos I de Física Teórica y Computacional, Granada, Spain
[148] University of Heidelberg, Institute for Theoretical Physics, Philosophenweg 16, 69120 Heidelberg, Germany
[149] W. W. Hansen Experimental Physics Laboratory, Kavli Institute for Particle Astrophysics and Cosmology, Department of Physics and SLAC National Accelerator Laboratory, Stanford University, Stanford, CA 94305, USA
[150] Warsaw University Observatory, Aleje Ujazdowskie 4, 00-478 Warszawa, Poland